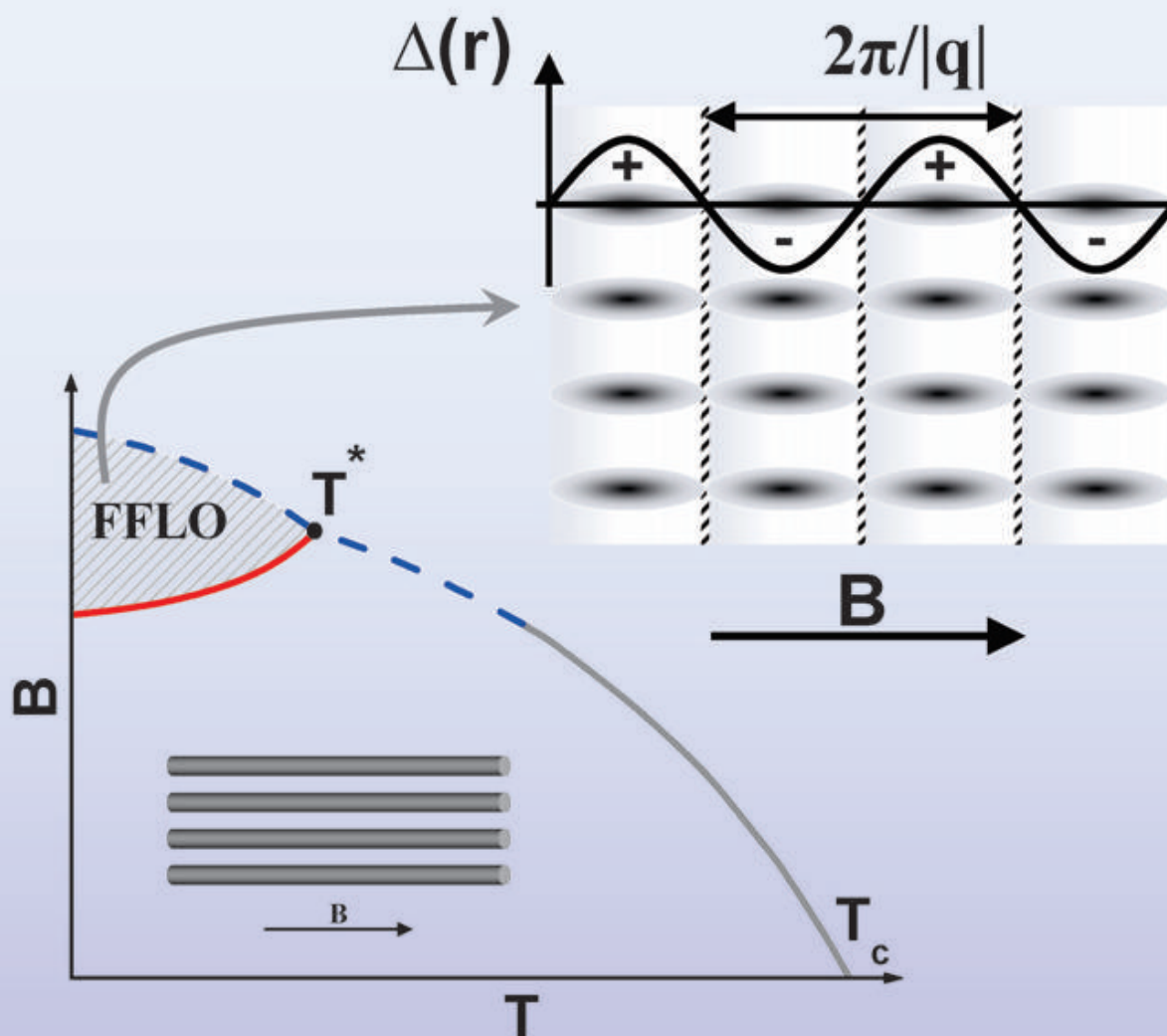Corneliu Florin Miclea

Investigation of superconducting order parameters in heavy-fermion and low-dimensional metallic systems under pressure

Investigation of superconducting order parameters in heavy-fermion and low-dimensional metallic systems under pressure

Dissertation

zur Erlangung des akademischen Grades

Doctor rerum naturalium
(Dr. rer. nat.)

vorgelegt

der Fakultät Mathematik und Naturwissenschaften
der Technischen Universität Dresden

von

Corneliu Florin Miclea

geboren am 04. April 1974 in Petrosani, Rumänien

Contents

Introduction

The understanding of new emerging unconventional ground states is a great challenge for experimental and theoretical solid-state physicists. New ground states are developing, where different energy scales compete, leading to a high sensitivity of the system to external tuning parameters like doping, pressure or magnetic field.

The exploration of superconductivity proved to be a fascinating and challenging scientific undertaking. Discovered by H. Kammerlingh Onnes in 1911, prior to the development of the quantum theory of matter, superconductivity was defying a microscopic theory for more than four decades until the BCS theory was formulated in 1957 by J. Bardeen, L. N. Cooper and J. R. Schrieffer. Superconductivity of most of the simple metals or metallic alloys is well described within the frame of the BCS scenario, however, in the last thirty years numerous new superconducting materials were found to exhibit exotic properties not accounted for by the BCS theory. Among them are included the high-T_c compounds, the heavy-fermion superconductors and as well the organic superconductors. It was the purpose of this work to probe different facets of superconductivity in heavy-fermion and in low-dimensional metallic compounds.

In the class of the heavy-fermion systems the Kondo-effect, leading to a non-magnetic ground state, competes with the Ruderman-Kittel-Kasuya-Yosida (RKKY) interactions which favors magnetic order. It is this competition which leads to unusual physical properties in proximity to a quantum critical point, where the magnetic ordering temperature is suppressed to zero. The heavy-fermion compound $CeCoIn_5$ is superconducting at atmospheric pressure having the highest superconducting transi-

tion temperature, among all Ce-based heavy-fermion systems [1]. $CeCoIn_5$ is assumed to be situated close to an antiferromagnetic quantum critical point giving rise to non-Fermi liquid behavior in the normal state [2]. Recently, the possible appearance of an inhomogeneous superconducting state in $CeCoIn_5$, called Fulde-Ferrell-Larkin-Ovchinnikov (FFLO) state, attracted much attention not only among solid state physicists [3, 4]. The FFLO state, predicted independently by Fulde and Ferrell [5] and by Larkin and Ovchinnikov [6] 40 years ago, is a spatially inhomogeneous superconducting phase, where the order parameter is periodically modulated in real space. It is predicted to appear in type-II superconductors close to the upper critical field if the orbital pair-breaking is negligible relative to the Pauli-limiting effect, in sufficiently clean systems. The theoretical concept of the FFLO state is not only of importance in solid state physics, but also in elementary-particle physics [7]. The FFLO state eluded the experimental confirmation until very recently. $CeCoIn_5$ is the first material where different physical experiments show strong evidence pointing to the realization of the FFLO state at low temperatures close to the upper critical field for superconductivity. However, the presence of strong antiferromagnetic fluctuations in this compound might be responsible for the anomaly taken as signature of the FFLO state.

The central part of the present work is the exploration of the nature of this low temperature phase observed inside the superconducting state in $CeCoIn_5$ at high magnetic fields. Using external pressure to suppress the magnetic fluctuations we were able for the first time to provide evidence that the FFLO state in $CeCoIn_5$ exists away from the influence of the strong magnetic fluctuations present at atmospheric pressure. For this purpose we developed a new type of miniature pressure cell allowing us to conduct heat capacity studies under quasi-hydrostatic pressure conditions at high magnetic fields up to $B = 14$ T and at low temperatures down to $T = 100$ mK, on precisely oriented $CeCoIn_5$ single crystals. We studied the evolution of the magnetic field – temperature phase diagram with pressure. Not only the first-order character of the transition from the normal to the superconducting state at high magnetic fields persists with increasing pressure, but we could also follow the

transition from the vortex to the FFLO state for all pressures. Moreover, the FFLO region in the phase diagram is extended at high pressures. This strongly supports the genuine FFLO origin of the anomaly in the superconducting state and makes a magnetic origin very unlikely.

Despite of more than two decades of intensive experimental studies to characterize the heavy-fermion superconductor UBe_{13}, many details behind its physical properties remain undisclosed. Several experiments probing the superconducting state of this material, revealed anomalous features which are regarded as evidence for unconventional superconductivity. The most compelling evidence obtained so far for unconventional superconductivity regards the giant ultrasonic absorption anomaly observed directly below T_c [8, 9] which was ascribed to collective modes or domain-wall damping due to a multi-component order parameter [10]. Theoretical calculations by Sigrist *et al.* [11, 12] predict the behavior of a multi-component order parameter for an anisotropic superconductor under uniaxial stress. Uniaxial stress is lowering the crystal symmetry and the degeneracy in the order parameter representation might be lifted leading to a split of the superconducting transition. We performed high resolution AC specific heat experiments under uniaxial pressure up to $p = 0.55$ GPa. A small feature resembling a superconducting temperature splitting is induced by pressure. However, this feature has to be regarded carefully as, though improbable, pressure anisotropy cannot be completely ruled out as origin.

The interplay between superconductivity and a charge-density wave (CDW) instability remains an interesting experimental and theoretical challenge. The opening of a dielectric gap in the electronic spectrum due to electron-hole pairing, reduces the density of states at the Fermi-level. However, not uncommon are the examples of compounds displaying a CDW instability which at lower temperatures enter a superconducting ground state. In such cases the superconductivity sets in from a normal but gapped state. We thoroughly investigated the quasi-one-dimensional, metallic compound $Tl_xV_6S_8$ employing resistivity, specific heat and susceptibility measure-

ments at ambient pressure for different Tl fillings. Moreover, in resistivity studies, we followed the evolution with pressure of both superconducting and CDW phases in the above mentioned compounds.

This dissertation is divided into six chapters. After this introduction, in Chapter 1 we will outline the basic theoretical concepts later needed for the analysis of the experimental results. In Chapter 2 we briefly introduce the experimental techniques with a special focus on the new pressure cells developed during this thesis and used for the measurements presented in Chapters 3 to 5. In Chapter 3 the possible realization of the inhomogeneous superconducting FFLO state in $CeCoIn_5$ is studied by specific heat measurements under hydrostatic pressure, while in Chapter 4 the results of AC specific heat experiments on UBe_{13} under uniaxial pressure are presented. The ambient pressure properties as well as results obtained by resistivity measurements under hydrostatic pressure on the one-dimensional metallic compounds $Tl_xV_6S_8$ are discussed in Chapter 5. At the end, Chapter 6 summarizes and concludes this thesis.

Chapter 1

Theoretical concepts

This chapter serves to outline some of the basic theoretical concepts which are related to the experimental results to be presented in the following chapters.

1.1 Fulde-Ferrell-Larkin-Ovchinnikov state

1.1.1 Introduction

For a type-II singlet superconductor (SC), in the clean-limit and for which the main pair-breaking mechanism is due to the spin susceptibility (Pauli paramagnetism), an inhomogeneous superconducting phase is predicted to appear at low temperatures and close to the upper critical field (B_{c2}), between the normal and the vortex state [5, 6]. At the core of this phase, called Fulde-Ferrell-Larkin-Ovchinnikov (FFLO), lie competing interactions of basic nature. One is the energy necessary to bind the electrons into Cooper pairs (the condensation energy) and the other is the interaction between the spin of the electrons and the magnetic field. In the normal state, the electrons are free to lower their total energy by preferentially aligning their spins along to the external magnetic field, leading to a temperature-independent Pauli susceptibility. On the other hand, in the superconducting state, the numbers of spin-down and spin-up electrons are equal and since they cannot all be aligned along the magnetic field, the ground state energy is higher than in normal state. In this way, Pauli paramagnetism will always favor the normal state against the spin-singlet superconducting phase. This effect, called Pauli-limiting, is reducing the upper critical field B_{c2} to the char-

acteristic Pauli field B_P, defined in the absence of all other pair-breaking mechanisms. The magnetic field can also suppress superconductivity when the kinetic energy of the supercurrent around the superconducting vortices becomes greater than the superconducting condensation energy; this is the orbital limiting effect and reduces the B_{c2} to the orbital-limiting field B_{c2}^{orb} defined in the absence of Pauli-limiting.

1.1.2   Pauli paramagnetism and superconductivity

The Pauli field for a classical BCS-superconductor was determined by A. M. Clogston [13] and B. S. Chandrasekhar [14]. The stability of the superconducting state compared to the normal state is given by the free-energy balance

$$F_s - F_n = -\frac{B_c^2}{8\pi},\tag{1.1}$$

where F_n and F_s are the free energies per volume unit in the normal and superconducting state, respectively, and B_c is the thermodynamic critical field. A metal, in the normal state, has a finite paramagnetic susceptibility χ_n caused by the electronic density of states at the Fermi-level. Upon applying magnetic field B the free energy will be lowered, due to the spin polarization, by an amount of $\frac{1}{2}\chi_n B^2$. The same metal, in the superconducting state, will have a susceptibility χ_s which is smaller than in the normal state due to the formation of Cooper pairs. According to the BCS theory, χ_s vanishes as the temperature is lowered to $T = 0$ K. Therefore, the free energy balance between the normal and the superconducting state, at absolute zero temperature, can be written as:

$$F_n - \frac{1}{2}\chi_n B_c^2 = F_s.\tag{1.2}$$

Considering the electronic gyromagnetic factor g and the electronic density of states at $T = 0$ K, $N(0)$, the spin susceptibility becomes:

$$\chi_n = \frac{1}{2}(g\mu_B)^2 N(0),\tag{1.3}$$

where μ_B is the Bohr-Procopiu magneton. The jump in the free energy at the superconducting phase transition can be related to the superconducting energy gap at
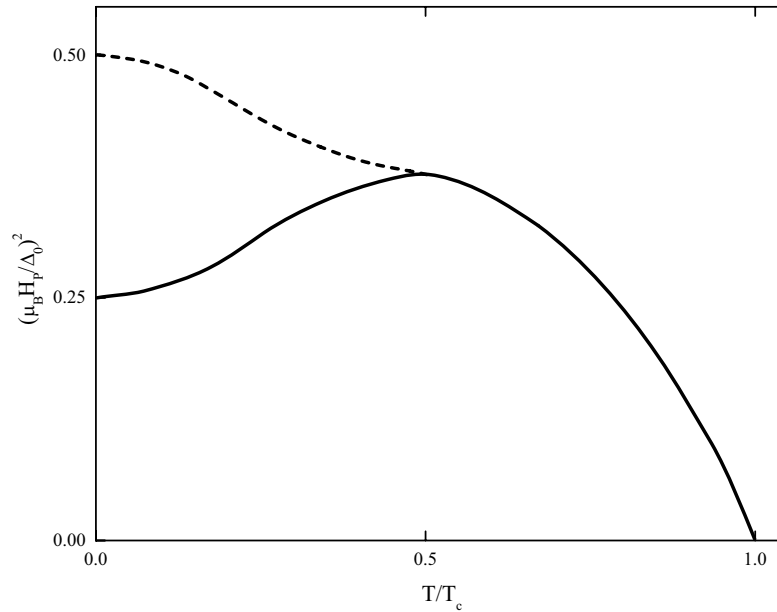
Figure 1.1: Above the critical point $t_0 = T_0/T_c = 0.556$ the solid line is the critical field for the second-order phase transition. Below t_0 the dotted line corresponds to the first-order phase transition and the solid line to the supercooling critical field.

$T = 0$ K, $\Delta(0)$ by:

$$F_n - F_s = \frac{1}{2} N(0) \Delta(0)^2. \tag{1.4}$$

Therefore, the upper limit for the critical field in the absence of any orbital effect (i.e., the Pauli field B_P), for a BCS superconductor, can be written as [13]:

$$B_P = B_{c2}(0) = \frac{\sqrt{2} \Delta(0)}{g \mu_B}. \tag{1.5}$$

The effect of Pauli paramagnetism on the order of the superconducting phase transition was discussed by G. Sarma [15] and K. Maki and T. Tsuneto [16]. They found that for a clean superconductor in which the Pauli paramagnetism is the dominant limiting factor for the upper critical field, the phase transition changes from second- to first-order as the temperature is lowered (Fig. 1.1). Below the critical point $t_0 = T_0/T_c = 0.556$ the phase transition between the normal and the superconducting phase, changes from second- to first-order; in this region, the gap equation has two solutions, one corresponding to the actual gap (dotted line) and the other corresponding to a supercooling critical field. It is important to remark that the lower line, below t_0 is not associated with a phase transition between a classical BCS phase

and an inhomogeneous superconducting state.

In the dirty-limit (one would intuitively expect a short mean-free path for super-conductors for which the orbital effect can be neglected) the phase transition should remain second-order for the whole temperature range [16].

1.1.3 FFLO state

Fulde and Ferrell [5] and at the same time Larkin and Ovchinnikov [6] have studied the effect of a large exchange field B acting only on the electronic spins, assuming that some of the Cooper pairs are broken in certain regions around the Fermi-surface. Those regions of unpaired electrons are stabilized by field and the corresponding opposite areas of the Fermi-surface are completely depleted of electrons with opposite spin orientation (Fig. 1.2). These regions are blocked for the pair formation process
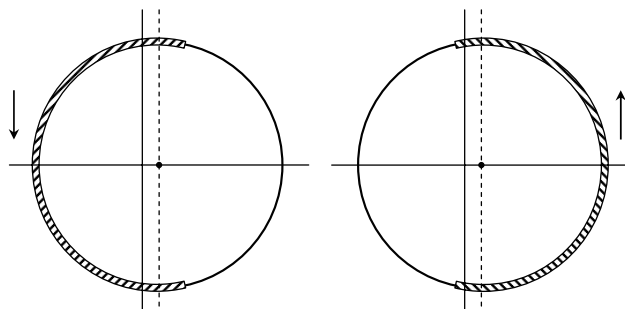
Figure 1.2: Depairing in momentum space produced by field. The Fermi-surface is shifted to the right. The left hashed area is fully occupied by down spin electrons polarized along the field. The right hatched area is completely depleted of spin-up electrons

since the BCS-theory requires that the states with opposite momenta are either both occupied or both empty.

If the BCS energy gap in the absence of any magnetic field is Δ_0 and $2H\Delta_0$ is the splitting of the electron energy due to the exchange field, the Hamiltonian of the system can be written as:

$$\mathcal{H} = \mathcal{H}_0 + H\Delta_0 \sum_i \sigma_i \, , \tag{1.6}$$

where $\mathcal{H}_0$ is the usual BCS Hamiltonian for a superconductor in the absence of an ex-

change field and σ_i is the operator ± 1 reflecting the spin alignment ("up" or "down") of the i-th electron with respect to the magnetic field. The second term of the Hamiltonian is proportional to the total electronic spin component parallel to the field, which operator commutes with $\mathcal{H}_0$ and therefore has the same set of eigenfunctions and associated eigenvalues with $\mathcal{H}_0$. Thus an approximate eigenfunction of $\mathcal{H}$ is the BCS ground state wave function.

For a field which produces a split of the conduction electrons energy of $\sqrt{2}\Delta_0$, the normal state undergoes already enough spin orientation to acquire a lower free energy than the BCS ground state [17]. Electronic configurations which lower further the energy of the system have even lower symmetry than in Fig 1.2 [5]. Therefore, the unpaired electrons are distributed asymmetrically around the Fermi-surface and this leads to a net current flow. But in the absence of magnetic field acting on the electron orbits, the ground state should not carry any current (Bloch's theorem).

Consequently, it is necessary for the remaining paired electrons to establish a counterflow current exactly canceling out that of the unpaired electrons. This leads to a remarkable result: the Cooper pairs are formed from states $(\mathbf{k}, -\sigma)$ and $(\mathbf{k}' = -\mathbf{k} + \mathbf{q}, \sigma)$ and have a finite momentum $\mathbf{q}$, where $\mathbf{k}$ and σ are the momentum and the spin of the one electron wave function (Fig. 1.3). The choice of $\mathbf{q}$ determines the size of regions with unpaired electrons and the value of the superconducting gap. The pairing wave vector $\mathbf{q}$ is determined as a function of the magnetic field imposing that the depaired current and the supercurrent (which both depend on $\mathbf{q}$) sum up to zero.

This new inhomogeneous superconducting phase yields a highly degenerate ground state characterized by the direction of the pairing momentum. For this phase to qualify as a ground state, the single-particle excitations must all have positive energies. Goldstone's theorem [18, 19], implies that there must exist low-lying collective modes. The mixed state was found to be stable over a finite range of the magnetic field. This range, for weakly coupled electrons is:

$$0.71 \, \frac{\Delta_0}{\mu_B} < B < 0.76 \, \frac{\Delta_0}{\mu_B} \quad [5]. \tag{1.7}$$
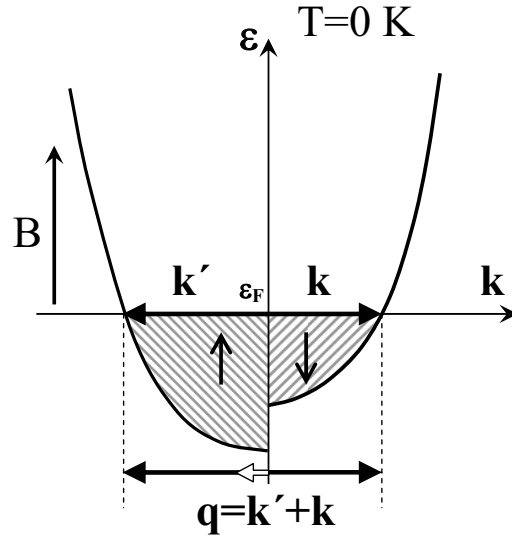
Figure 1.3: The Cooper pairs are formed from $(\mathbf{k}, -\sigma)$ and $(\mathbf{k}', \sigma)$ states, with a finite momentum $\mathbf{q}$. The energy is lowered for the electrons with the spins parallel to the magnetic field B.

An increased coupling strength will decrease the stability of the depaired phase relative to the BCS state, but will decrease the energy of the normal state even more, due to enhanced magnetization. Therefore, the stability range for the strong coupling case is significantly extended to:

$$0.83 \, \frac{\Delta_0}{\mu_B} < B < 1.13 \, \frac{\Delta_0}{\mu_B} \quad [5]. \tag{1.8}$$

The BCS superconducting gap has to be integrated taking into account the regions of the Fermi-surface allowed to pairing:

$$\Delta = N(0)V \left(\int_0^{\hbar\omega_0} \frac{\Delta}{E_{\mathbf{k}}} d\varepsilon_{\mathbf{k}} - \int_{blocked} \frac{\Delta}{E_{\mathbf{k}}} d\varepsilon_{\mathbf{k}} \right), \tag{1.9}$$

where the second integral is over all depaired regions, $E_k = \sqrt{\varepsilon_{\mathbf{k}}^2 + \Delta^2}$, $\varepsilon_{\mathbf{k}}$ is the electron energy relative to the Fermi-level ε_F and $\varepsilon_F - \hbar\omega_0 < \varepsilon_{\mathbf{k}} < \varepsilon_F + \hbar\omega_0$, $N(0)$ is the density of states at the Fermi-level and V is the volume. For this phase to be a ground state, all single-particle excitations must have positive energies. The quasiparticle energy associated with the addition of a particle with the wave vector $\mathbf{k}$ and energy $\varepsilon_{\mathbf{k}}$ is given by:

$$\mathcal{E}_{\mathbf{q},B} = E_{\mathbf{k}} + \frac{1}{2}g\mu_B B\sigma + \frac{\hbar}{m}\mathbf{q}\mathbf{k} \geq 0 \,, \tag{1.10}$$

where $\frac{1}{2}g\mu_B B\sigma$ is the energy change due to the Zeeman effect ($\sigma = \pm 1$), $\frac{\hbar}{m}\mathbf{q}\mathbf{k} = |\mathbf{q}|v_F$ is caused by the finite momentum $|\mathbf{q}|$ pairing (i.e., shift of the Fermi-surface) and v_F is the Fermi velocity. At the boundary of the blocking region we have:

$$\mathcal{E}_{\mathbf{q},B} = 0 \,. \tag{1.11}$$

The width of the blocking regions in momentum space is determined by solving the equation 1.11. Using this in the integral 1.9 one can obtain the gap equation which in real space can be written as:

$$\Delta(\mathbf{r}) = |\Delta_{\mathbf{q}}| \, \exp(i\mathbf{q}\mathbf{r}) \quad [5] \tag{1.12}$$

or

$$\Delta(\mathbf{r}) = |\Delta_{\mathbf{q}}| \, \cos(\mathbf{q}\mathbf{r}) \quad [6] \,. \tag{1.13}$$

Therefore this inhomogeneous superconducting phase, called Fulde-Ferrell-Larkin-Ovchinnikov state, shows an unusual and remarkable spatial modulation of the order parameter in real space, meaning that the normal and the superconducting regions of the material are placed alternately perpendicular to the magnetic field and the vortices (Fig. 1.4). The order parameter has nodes ($\Delta(\mathbf{r}) = 0$) in the normal planes with a periodicity of $2\pi/|\mathbf{q}|$. The size of the superconducting regions depends on pairing momentum $\mathbf{q}$.

In contrast to the classical BCS state, the FFLO phase exhibits spin magnetization, almost normal state tunneling and specific heat. This is expected as a result of an almost constant density of states (though with some structure) qualitatively similar with the normal state [5]. The spin polarization appears around the nodes of the order parameter and the wavelength of the spin-density wave is $\pi/|\mathbf{q}|$ with the spin-density of the quasiparticles given by:

$$<\sigma> \approx \sigma_n \left[1 - \left(\frac{\Delta(\mathbf{r})}{\Delta_0} \right)^2 \right], \tag{1.14}$$

where $\sigma_n = 2\mu_B B N(0)$ is the spin polarization in the normal state [20].

According to the Ginzburg-Landau theory, the supercurrent is proportional to the square of the order parameter, therefore it cannot pass through the nodal planes.
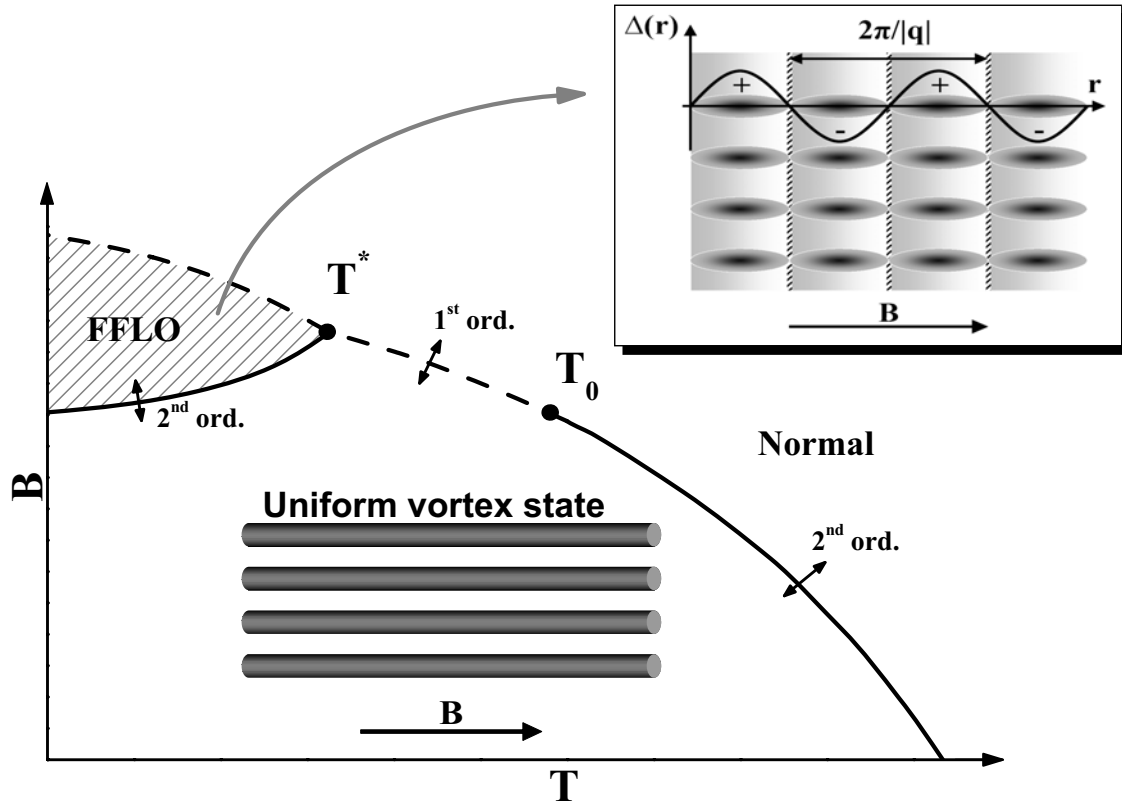
Figure 1.4: Generic $B(T)$ phase diagram. At low temperatures and high magnetic fields, an FFLO phase emerges between the BCS-superconducting and the normal state. In this phase, the order parameter is spatially modulated along the magnetic field. The hatched regions ($\Delta(\mathbf{r}) = 0$) in the upper inset are in the normal state and the gray ones are superconducting regions.

Nevertheless, this theory is only valid close to T_c and it has been shown that the supercurrent is passing, with a phase shift, in the direction of the exchange field, through the regions where the order parameter is vanishing [20]. It is also important to note that the FFLO state is readily destroyed by impurities [21].

The findings of Fulde-Ferrell and Larkin-Ovchinnikov apply also if the exchange field is replaced by an uniform external magnetic field providing that the orbital effects are sufficiently small.

1.1.4   Order of the FFLO phase transition and dimensionality

According to the original paper of Fulde and Ferrell [5], upon increasing the magnetic field, the system undergoes a first-order phase transition from the conventional vortex

state to the FFLO phase and then, at the upper critical field, a second-order phase transition into the normal state. The pairing momentum at the latter transition is given by:

$$|\mathbf{q}_c| = \frac{g\mu_B B_c}{0.833 \ v_F}. \tag{1.15}$$

But depending on how strong is the Pauli-limiting effect and on the details of the free energy expansion in powers of the order parameter, the order of the transitions can be reversed. Larkin and Ovchinnikov [6] left open the possibility for a first-order transition from FFLO to normal state. More recent and extensive calculations were addressing the problem of the order of the transition in both, two (2D) and three dimensions (3D) for conventional *s*-type superconductors and in the absence of orbital effects.

In 2D it is generally believed that the phase transition from the normal to the FFLO state is of second-order in the whole temperature range. In particular Burkhardt and Rainer [22] have found, at finite temperature, an order parameter $\Delta_0(\mathbf{r})\cos(\mathbf{q}\mathbf{r})$. This is the order parameter found by Larkin and Ovchinnikov in 3D at $T = 0$ K, for a second-order phase transition. However, in 2D and at low temperature, the order parameter becomes more complicated and can be a superposition of more than two plane waves [23]. The low temperature case in 2D was addressed in detail by Combescot and Mora [24]. They found that for an isotropic Fermi surface (i.e., a circle in 2D) the order parameter changes from a simple $\cos(\mathbf{q}\mathbf{r})$ close to the tricritical point to an increasingly more complex one as the temperature is lowered. The order parameter, at the transition in the normal state, changes to a superposition of planar waves with equal weights and equal wave vector moduli. The directions of these wave vectors are equally spaced angularly and with an angle which goes to zero as the temperature is decreased to zero. This gives rise to an infinite number of planar waves, singularity related to the fact that in 2D the Fermi-surface is a line. The transitions between the various FFLO phases and the normal state remain second-order.

In 3D, in the vicinity of the tricritical point, the order parameter is a simple $\cos(\mathbf{q}\mathbf{r})$ at the transition [25–27], and the phase transition from FFLO to normal state

is always first-order [28–30]. Upon decreasing the temperature, the order parameter changes to a sum of two cosines with equal weights and wave vectors with same moduli but orthogonal directions. Finally, by further lowering the temperature, one finds another transition toward an order parameter which is a sum of three cosines, again with same weights and wave vectors with equal moduli and orthogonal directions [29]:

$$\Delta(\mathbf{r}) = \Delta_0[\cos(\mathbf{q}_1\mathbf{r}) + \cos(\mathbf{q}_2\mathbf{r}) + \cos(\mathbf{q}_3\mathbf{r})] \qquad (1.16)$$

where $\mathbf{q}_1$, $\mathbf{q}_2$, $\mathbf{q}_3$ are orthogonal and $|\mathbf{q}_1| = |\mathbf{q}_2| = |\mathbf{q}_3|$.

It must be underlined that the orbital effect [31], the pairing symmetry and also small amounts of impurities [32] may influence the order of the phase transition and the structure of the order parameter.

1.1.5 Orbital effects

The orbital-limiting effect is the one which, in general, has the main influence in determining the upper critical field of a superconductor. So taking it into account, in the context of the FFLO state in type-II superconductors, is of great importance.

The influence on the upper critical field of both, Pauli and orbital-limiting, was discussed for the dirty-limit case by Werthamer *et al.* [33] and independently by Maki [16, 34]. They conclude that the orbital interactions reduce the effect of spin paramagnetism in limiting B_{c2} and also diminish the possibility to have a first-order phase transition into the normal state at low temperatures and in high magnetic fields.

The formation of a FFLO state is favorable only in the clean-limit [21, 35, 36]. The realization of this state depends on the relative strength of the Pauli paramagnetism and of the orbital effects. This is quantified by the Maki parameter α [37]:

$$\alpha = \frac{\sqrt{2}B_{c2}^{orb}}{B_P}, \qquad (1.17)$$

where B_{c2}^{orb} and B_P are the orbital and Pauli field, respectively, defined at the beginning of this chapter.
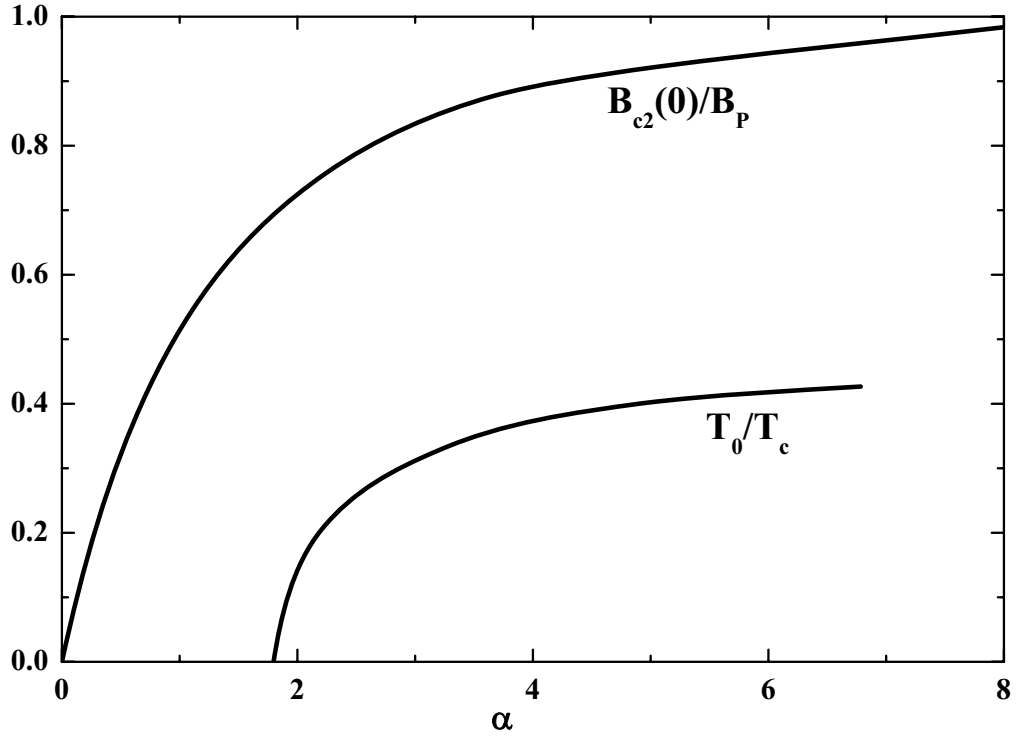
Figure 1.5: $\frac{B_{c2}(0)}{B_P}$ and $\frac{T_0}{T_c}$ as function of the Maki parameter α according to L. W. Gruenberg and L. Gunther [36].

L. W. Gruenberg and L. Gunther showed for the first time that the FFLO state formation is possible in the presence of orbital effects [36]. Their results for an *s*-wave type-II superconductor are depicted in Fig. 1.5, where $B_{c2}(0)$ is the upper critical field at $T = 0$ K, T_c is the temperature of the normal to superconducting phase transition and T_0 is the temperature of the tricritical point. They found out that the formation of the FFLO phase is possible only in systems for which

$$\alpha > \alpha_c = 1.8 \tag{1.18}$$

is fulfilled and below a characteristic temperature $T_0(\alpha)$. For $\alpha \to \infty$ the orbital limiting effect can be neglected and the upper limit for T_0 is:

$$T_0 = T_c(B_0) = 0.55\, T_c(B = 0) \quad [36]. \tag{1.19}$$

Also, for $\alpha \to \infty$, the phase transition to the normal state is of first-order [15, 16]. $B_{c2}(0)$ increases monotonously with α and reaches asymptotically, in the pure
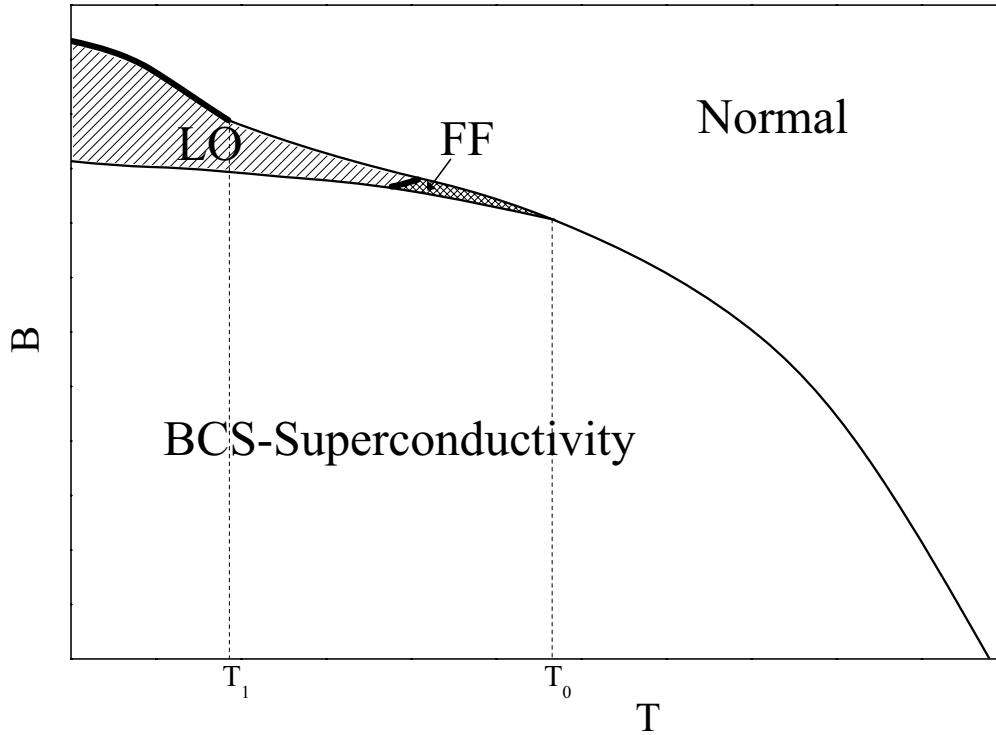
Figure 1.6: Generic $B(T)$ phase diagram proposed by M. Houzet *et al.* [31] for an *s*-type superconductor and accounting for both, orbital and Pauli-limiting effects. The thick lines represent first-order phase transitions.

paramagnetic limit:

$$B_{c2}(0)_{\alpha \to \infty} = B_P. \tag{1.20}$$

Equation 1.20 gives the lower limit for B_P. The Gruenberg-Gunther ansatz is of great importance since it is valid for *d*-wave and other nodal superconductors as well. The orbital field is proportional to the initial slope of B_{c2} [38]:

$$B_{c2}^{orb} = 0.7 \, T_c \, \left. \frac{\partial B_{c2}}{\partial T} \right|_{T_c}. \tag{1.21}$$

It was suggested by M. Houzet *et al.* [31] that in the clean-limit, for an *s*-type superconductor, the presence of orbital effects reduces the temperature of the tricritical point relative to the pure paramagnetic case by:

$$\Delta T_0 \approx 1.2 \frac{T_c}{\alpha}. \tag{1.22}$$

The generic phase diagram obtained by M. Houzet *et al.* [31] is presented in Fig. 1.6. The inhomogeneous superconducting state has an $\exp(i\mathbf{qr})$ (Fulde-Ferrell

state) modulation of the order parameter immediately below T_0 in a narrow temperature range $\Delta T \approx 0.08 T_c / \alpha$. The system changes through a first-order phase transition into another unpaired state with a $\cos(\mathbf{qr})$ modulation (Larkin-Ovchinnikov state). Below a certain temperature T_1, with $T_0 - T_1 \approx 4 T_c / \alpha$, the transition from normal to FFLO state changes from second- to first-order.

1.1.6 FFLO state in *d*-wave superconductors
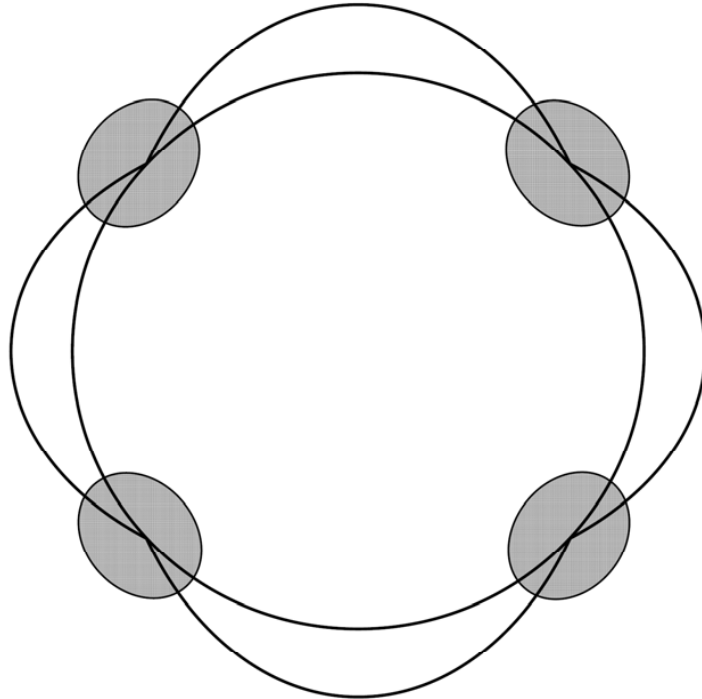
Figure 1.7: Fermi-surface for a *d*-wave superconductor. The shadowed ellipses are pockets of unpaired electrons with spins polarized along the magnetic field

It is important to discuss the FFLO state in the context of *d*-wave superconductors since for this type of superconductors it is more probable to achieve the conditions requested for the formation of the inhomogeneous superconducting phase. The main difference to the *s*-wave case is that even at zero field the superconducting gap has nodes. Upon increasing the field, pockets of normal, polarized electrons form around the initial nodes (Fig. 1.7). The inner and outer parts of the pockets are pieces of

the field-split Fermi surface which come together when the Zeeman energy exceeds the angle dependent gap function. K. Yang *et al.* [39] have found that for a 2D *d*-wave superconductor, ignoring the orbital effect, the $B - T$ phase diagram remains qualitatively similar to the *s*-wave case. Moreover, they showed that the stability range of the unpaired phase is considerably extended to $0.56\,\Delta_0 < \mu_B B < 1.06\,\Delta_0$ compared with $0.71\,\Delta_0 < \mu_B B < \Delta_0$ [40] for the 2D *s*-wave case. The transition from the normal to the FFLO state is second-order and is followed by a first-order phase transition, at lower fields, into the zero momentum pairing state.

It is also important to remark that for the *d*-wave case the FFLO state seems to be more robust against impurities [32].

1.1.7   Conclusions

The realization of the inhomogeneous superconducting FFLO state is possible in type-II singlet superconductors in the clean-limit and with a high Maki parameter $\alpha > 1.8$, at high fields and low temperatures ($T \leq 0.56\,T_c$ [39]). Such conditions are extremely difficult to achieve in conventional superconductors [41]. Therefore, an important strategy to observe this phase is to eliminate, as much as possible, the orbital currents which are responsible for the low critical fields in ordinary superconductors. A path to achieve this is to lower the electronic dimensionality of the system in a geometry where the orbital currents would have to flow in an actually prohibited direction. Other systems for which the field coupling to the orbital degrees of freedom is comparable with the coupling to the electronic spins are, for example, the heavy-fermion systems due to the largely enhanced electronic masses. But in this last case the sensitivity to the impurities should be regarded with great attention. It is therefore not surprising that earlier observations of possible FFLO phases in heavy fermion compounds [42] have been disputed.

For a very strong Pauli-limiting effect ($\alpha \gg 1.8$) the phase transition from the FFLO to the normal state is expected to be of first-order regardless of the system dimensionality. Nevertheless, in a 2D system, theoretical studies suggest that the order of the phase transition could change, from first-order in the vicinity of the

tricritical point, to second-order, as the temperature is lowered to $T = 0$ K.

The appearance of unconventional superconductors such as the heavy-fermions, organic and high-T_c compounds, opens up a new window for exploration of the FFLO state. Many of these materials have a layered structure with larger Fermi velocities within the conducting plane. Technical advances in single crystal growth allow now to obtain samples with an electronic mean-free path of the order of microns which favors the FFLO state. Finally, for d-wave superconductivity the FFLO state has a more extended stability region and is more robust against impurities [32] than for the s-wave superconductors.

In addition to its intrinsic fundamental interest, the FFLO phase has also a potential practical relevance since it appears in superconductors with very high critical fields. It was also suggested that this phase is of high importance for the physics of ultracold gases in their superfluid BCS-like state [43, 44] and also in the physics of quark matter [7] as it might be found in the center of the neutron stars.

Theoretical models, assuming a weak coupling BCS model with $d_{x^2-y^2}$ pairing symmetry, a quasi-2D electronic structure and the Gruenberg-Gunther ansatz have been developed [45, 46]. A different approach based on antiferromagnetic (AFM) spin fluctuations in the frame of a mean-field theory offers as well a way to qualitatively explore the FFLO state [47].

However, to properly understand the physics of this state, particularly for unconventional superconductors, remains an important challenge.

1.2   Charge-density wave phenomena

1.2.1   Introduction

While charge-density wave (CDW) formation occurs in materials with two- or three-dimensional band structure, they are predominantly a one-dimensional phenomenon. The basic concepts regarding the physical properties of such CDW states were first addressed by Peierls [48] more than 50 years ago. He pointed out that a one-dimensional metal coupled to the underlying lattice is not stable at low temperatures as the system favors a new ground state displaying a static periodic lattice distortion and a modulation of the conduction electron density.

Moreover, the ground state of the coupled electron-phonon system is characterized by a gap in the single-particle excitation spectrum and by a collective mode formed by electron-hole pairing involving the wave vector $|\mathbf{q}| = 2k_F$ (k_F is the Fermi wave vector) as the paired electron and hole are situated on opposite points of the Fermi-surface. The charge-density associated with the collective mode is given by

$$\rho(\mathbf{r}) = \rho_0 + \rho_1 \cos(2\mathbf{k}_F \cdot \mathbf{r} + \varphi) \quad [49], \tag{1.23}$$

where ρ_0 is the unperturbed electron density and the condensate is called the charge-density wave. The phase φ is of fundamental importance as its time and spatial derivative are related to the electrical current and to the condensate density.

1.2.2   Instability in a one-dimensional electron gas

A one-dimensional electron-gas interacting with a periodic potential $\phi(\mathbf{r}) = \int_{\mathbf{q}} \phi(\mathbf{q}) e^{i\mathbf{q}\mathbf{r}}$ will have a response function (Lindhard susceptibility):

$$\chi^d(\mathbf{q}) = \int \frac{1}{(2\pi)^d} \frac{f_{\mathbf{k}} - f_{\mathbf{k}+\mathbf{q}}}{\epsilon_{\mathbf{k}} - \epsilon_{\mathbf{k}+\mathbf{q}}} d\mathbf{k} \quad [50], \tag{1.24}$$

where $\mathbf{q}$ is the wave vector, $\epsilon_{\mathbf{k}}$ is the electron energy, $f_{\mathbf{k}} = f(\epsilon_{\mathbf{k}})$ is the Fermi distribution function, and d is the dimensionality of the system.

In the one-dimensional case, the particular topology of the Fermi-surface leads to an electronic dispersion $\epsilon_k = E_F \pm \hbar v_F (k - k_F)$ (E_F is the Fermi-level) [50]. In

this case the equation 1.24 can be rewritten as:

$$\chi^{1D}(q) = -e^2 N(E_F) \ln \left| \frac{q + 2k_F}{q - 2k_F} \right|, \tag{1.25}$$

with $N(E_F)$ the density of states at the Fermi-level. $\chi^{1D}(q)$ diverges for electron-phonon pairing $q = 2k_F$. This topology is called perfect nesting and for an arbitrary cutoff energy ϵ_0, at finite T, the response function becomes [50]:

$$\chi^{1D}(2k_F, T) = -e^2 N(E_F) \ln \frac{1.14\,\epsilon_0}{k_B T} \ . \tag{1.26}$$

The system becomes unstable for $T \to 0$.

1.2.3 Mean-field approach to charge-density wave phenomena

For a one-dimensional metal at $T = 0$ K, in the absence of electron-electron or electron-phonon interactions the ground state corresponds to the situation depicted in Fig. 1.8, left panel; the electron states are occupied up to the Fermi-level, E_F, and the undistorted crystal has a lattice constant a. The charge-density is independent of the spatial coordinates. The presence of the electron-phonon interaction renders more energetically favorable a periodic lattice distortion. This distortion opens up a gap at the Fermi-level as depicted in the right panel of Fig. 1.8, where the situation appropriate for a half-filled band is presented. The electrons only occupy states $\mathbf{k}$ with $-|\mathbf{k}_F| < |\mathbf{k}| < |\mathbf{k}_F|$ and the gap leads to a reduction of the electronic energy.

In the one-dimensional case the magnitude of the single-particle gap Δ depends proportionally on the lattice distortion u and the reduction of the electronic energy for a small displacement is proportional to $u^2 \ln(u)$. Moreover, the deformation leads also to an increase of the elastic energy proportional to u^2 [51]. Therefore, a small distortion might lower the energy of the system compared to the undistorted state. The magnitude of the distortion is given by the maximum gain in energy. The modification of the dispersion relation leads also to a spatially dependent electron density.
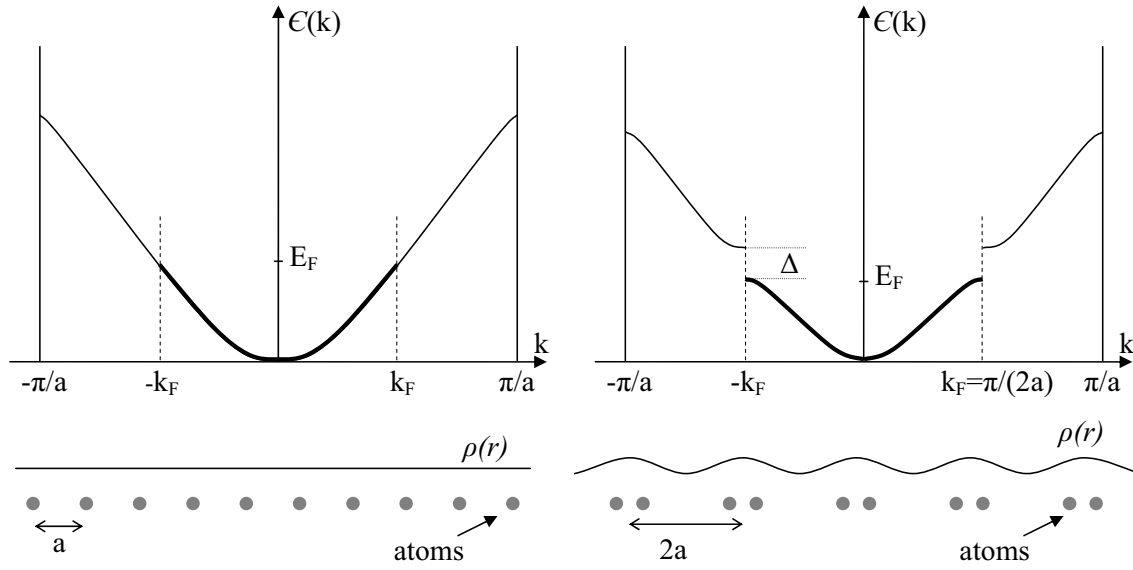
Figure 1.8: Sketch of a Peierls distortion in a one-dimensional metal with a half-filled band and the corresponding $\epsilon(k)$ diagram. Left panel: undistorted lattice. Right panel: the distorted lattice coupled with a spatially periodic modulation of the charge-density leading to the opening of a gap in the single particle spectrum.

For an arbitrary band filling, the wavelength of the charge-density (λ_{CD}) and the accompanying periodic lattice distortion are incommensurate with the underlaying lattice, i.e., λ_{CD}/a is irrational.

Since the CDW instability develops as collective mode involving electron-hole pairs coupled with the lattice distortion, both the electronic and phononic dispersion relations are modified in the new ground state. Peierls [48] and Fröhlich [52] addressed the one-dimensional coupled electron-lattice system in the frame of a mean-field theory in the weak coupling electron-phonon limit. In this approximation the system is described by the following Hamiltonian:

$$\mathcal{H} = \sum_{k,\sigma} \epsilon_k \, c_{k\sigma}^\dagger c_{k\sigma} + \sum_{k,\sigma} \hbar \, \omega_q \, b_q^\dagger b_q + \sum_{k,q,\sigma} g_k \, c_{k+q,\sigma}^\dagger c_{k,\sigma} (b_q + b_{-q}^\dagger), \qquad (1.27)$$

where $c_k^\dagger$ and c_k ($b_q^\dagger$ and b_q) are the electron (phonon) creation and annihilation operators with momenta k and q and spin σ. The electron and phonon dispersions are denoted by ϵ_k and ω_q, respectively, and g_k is the electron-phonon coupling constant. The first term of the Hamiltonian describes the one-dimensional free electron gas and

the second the one-dimensional chains of ions. The last term denotes the coupling between the two systems.

By solving the equation of motion for this Hamiltonian and making use of equation 1.26 one can derive the phonon dispersion relation and from this the CDW transition temperature:

$$T_{CDW}^{MF} = \frac{1.14\,\epsilon_0}{k_B}\,e^{-\frac{1}{\lambda}}, \tag{1.28}$$

where the dimensionless electron-phonon coupling constant λ is given by:

$$\lambda = g^2 \frac{2k_F}{\omega_{2k_F} E_F}. \tag{1.29}$$

The BCS-like expression of the CDW transition temperature (equation 1.28), indicates that the T_{CDW}^{MF} is enhanced as the electron-phonon coupling is increased. The complex CDW state order parameter can be defined, similar to the BCS theory, as:

$$\Delta = |\Delta|e^{i\phi}, \tag{1.30}$$

where $|\Delta|$ is related to the single-particle gap.

Without going into the details of the calculations which are carried out under the basic assumptions of the weak-coupling limit (i.e., $E_F \gg |\Delta|$), we summarize the main results of the mean-field theory approach in the following:

○ The periodic lattice distortion:

$$\langle u(x) \rangle = \Delta u \cos(2k_F x + \phi), \tag{1.31}$$

with the single-particle gap being proportional to the atomic displacement $\Delta u \sim |\Delta|/g$.

○ The modulation of the charge-density:

$$\rho(x) = \rho_0 \left[1 + \frac{\Delta}{\hbar v_F k_F \lambda} \cos(2k_F x + \phi)\right], \tag{1.32}$$

where ρ_0 is the spatially constant electronic density for $T > T_{CDW}^{MF}$.

○ The specific heat jump at the CDW phase transition

$$\frac{\Delta C}{\gamma_e T_{CDW}^{MF}} = 1.438 \, k_B^2 \, N(E_F), \qquad (1.33)$$

where γ_e is the linear specific heat coefficient of the electron gas.

○ The zero-temperature gap is related to T_{CDW}^{MF} by a BCS-like relation:

$$\Delta(0) = 1.76 \, k_B T_{CDW}^{MF}. \qquad (1.34)$$

1.2.4   Fluctuations and strong electron-phonon coupling effects

The mean-field description neglects the effect of fluctuations which, in the one-dimensional case, are particularly important. Fluctuations increase the dimensionality of the system and strongly suppress the transition temperature [53]; for a single metallic chain the phase transition does not occur at finite temperature anymore. For a system of coupled 1D chains the phase transition is restored again at non-zero temperatures with most of the 1D correlations preserved in the CDW state [51, 54].

The coupling between 1D-chains is realized mainly via two mechanisms: the Coulomb interaction between electrons situated in neighboring chains and via single-particle tunneling between the chains [50]. In such a picture a new transition temperature T_{3D} has to be defined as the temperature below which the correlations on the neighboring chains couple together, leading to a 3D long range order [53]. The general picture that emerges is that chain systems, which are metals at high temperatures, show strong 1D correlations along the chains above T_{3D} leading to a wide fluctuating region for the transition: $T_{3D} < T_{CDW} < T_{CDW}^{MF}$.

The effect of inter-chain coupling on the Peierls transitions in 1D chain systems has been addressed within the mean-field theory, including the effect of fluctuations by Horovitz *et al.* [55]. They found, for a given electron-phonon coupling, that the CDW transition is robust against the inter-chain coupling η up to a critical value η_c above which the transition temperature is drastically suppressed (Fig. 1.9). The
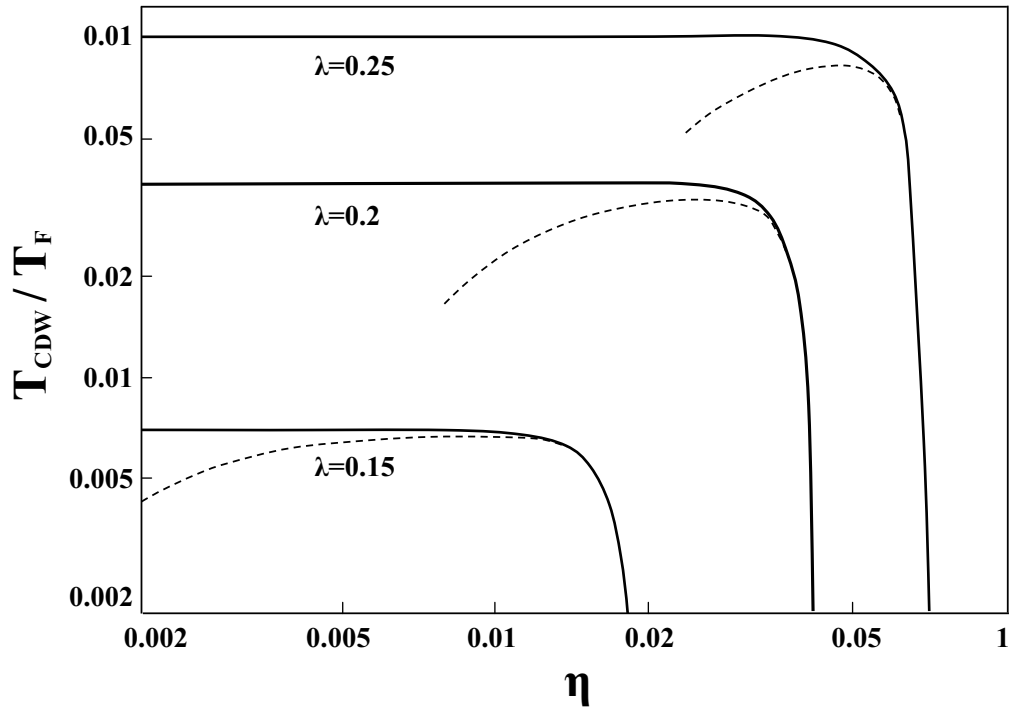
Figure 1.9: T_{CDW} normalized to the Fermi temperature T_F as a function of the inter-chain coupling η for different electron-phonon couplings λ. The solid line is the mean-field temperature. The dashed lines are obtained when fluctuation effects are also included into the calculation. From Ref. [55].

additional fluctuations narrow even further the stability range of the CDW state. Strong coupling theories for CDW instabilities have been developed also by McMillan [56] and later by Varma [57].

1.2.5   Conclusions

The CDW state occurs preponderantly in low-dimensional systems where parts of the Fermi-surface are nested. Nevertheless another route towards CDW instabilities, besides nesting, in low-dimensional systems is the existence of van Hove saddle points [58]. The appearance of a gap in the single-particle excitation spectrum, together with the collective mode described by a complex order parameter are features reminiscent of superconductivity. However, the collective mode here is formed by electron-hole pairs involving the wave vector $2k_F$ as the electrons and the holes on opposite sides of the Fermi-surface are combined to lead to the CDW instability and to the accom-

panying lattice distortion. The cutoff energy which enters the CDW gap equation is large compared to the characteristic phonon frequencies involved in the superconducting gap. Consequently the CDW transition temperature is considerably larger than the superconducting transition temperatures. Furthermore, the CDW temperature is strongly influenced by both, the electron-phonon and inter-chain coupling.

Interestingly, in real 3D compounds although anisotropic, superconductivity and CDW coexist as proven by numerous experimental results. In the struggle for the FS the superconductivity is often found to be the weaker competitor.

Chapter 2

Experimental methods: Pressure cells

This chapter serves to outline some of the basic experimental setups used to obtain to the experimental results to be presented in the following chapters emphasizing mainly the devices developed during this work.

Pressure is an ideal control parameter to tune a compound through various parts of its phase diagram. Other control parameters such as doping or magnetic field have the disadvantage of introducing additional complexities due to the effect of disorder in the case of doping or due to breaking of the time-reversal symmetry in the case of magnetic field.

2.1 Miniaturized specific heat pressure cell

Specific heat measurements under pressure, at low temperature and in high magnetic field, require specially developed pressure cells with the lowest possible contribution (addenda) to the total heat capacity.

This was the motivation for us to develop a new miniaturized piston-cylinder type pressure cell built entirely from very clean CuBe. The cell was designed to fit on the commercially available Quantum Design specific heat platforms and as well to be easily accommodated on any typical size specific heat platforms used in dilution cryostats.

Great attention has to be paid to the heat treatment of the CuBe as this is
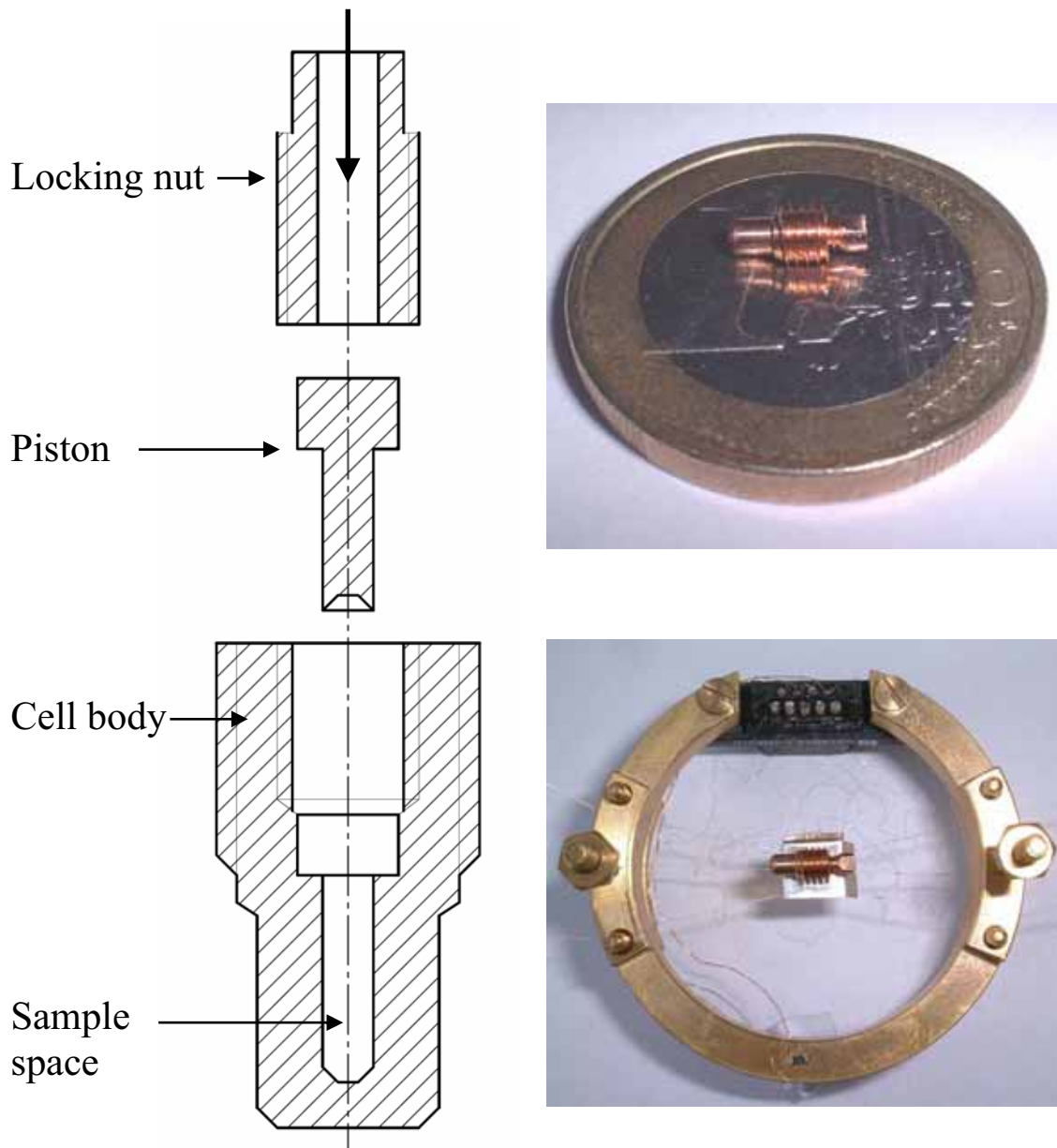
Figure 2.1: Left panel: the component parts of the miniaturized specific heat pressure cell. Right, upper panel: size reference for the cell. Right, lower panel: the pressure cell mounted on a self-built specific heat platform designed for a dilution refrigerator.

the determining factor in setting the upper pressure limit achieved in the cell; in our case the material was annealed at 325°C for 2.5 hours. In Fig. 2.1, a sketch of the component parts of the cell is displayed. The force is applied via a piston (not shown in the figure) along the direction depicted by the vertical arrow. Once the desired

force is achieved the locking nut is closed and keeps the whole force. The right panel shows a size reference for the cell (upper picture) and the cell mounted on a self-built specific heat platform designed for a dilution refrigerator.

Cell characteristics:

○ The pressure cell mass is of only 160 mg and its filling factor (sample/addenda heat capacity ratio) is well above other specific heat pressure cells.

○ Inner bore diameter: below 1 mm;

○ Pressure transmitting medium: Pb;

○ Pressure determination: The pressure is determined by the inductively measured shift of the SC transition temperature of Pb used also as pressure medium, relative to a Pb sample placed outside, directly on the cell. Good hydrostatic conditions, comparable to the liquid filled cells, are achieved;

○ Maximum pressure: we achieved pressures around $p \approx 1.4$ GPa, in the first and up to date the only study employing this cell, without reaching the upper limit of the cell. The maximum threshold expected for this CuBe cell is of about $p = 1.6$ GPa.

2.2   Pressure cell for resistivity studies

We developed a double-wall piston-cylinder pressure cell designed for resistivity measurements and downsized to fit in a commercially available Quantum Design Physical-Property-Measurement-System (PPMS) and as well in any of the dilution refrigerator cryostats available to us.

The schematic drawing of the double-wall piston-cylinder pressure cell used in the resistivity study is depicted in Fig. 2.2. The cell has an outer wall of annealed CuBe inside which an inner body made out of a special alloy (hardened MP35N) is fitted. The inner body has to withstand most of the pressure. The force is applied

CuBe locking nut

MP35N pressure
pad

MP35N feedthrough

CuBe sealing ring

CuBe jacket
(outer wall)

MP35N
inner wall

Teflon cap (sample
space)

Cu sealing ring

WC piston

MP35N pressure
pad

CuBe Locking nut
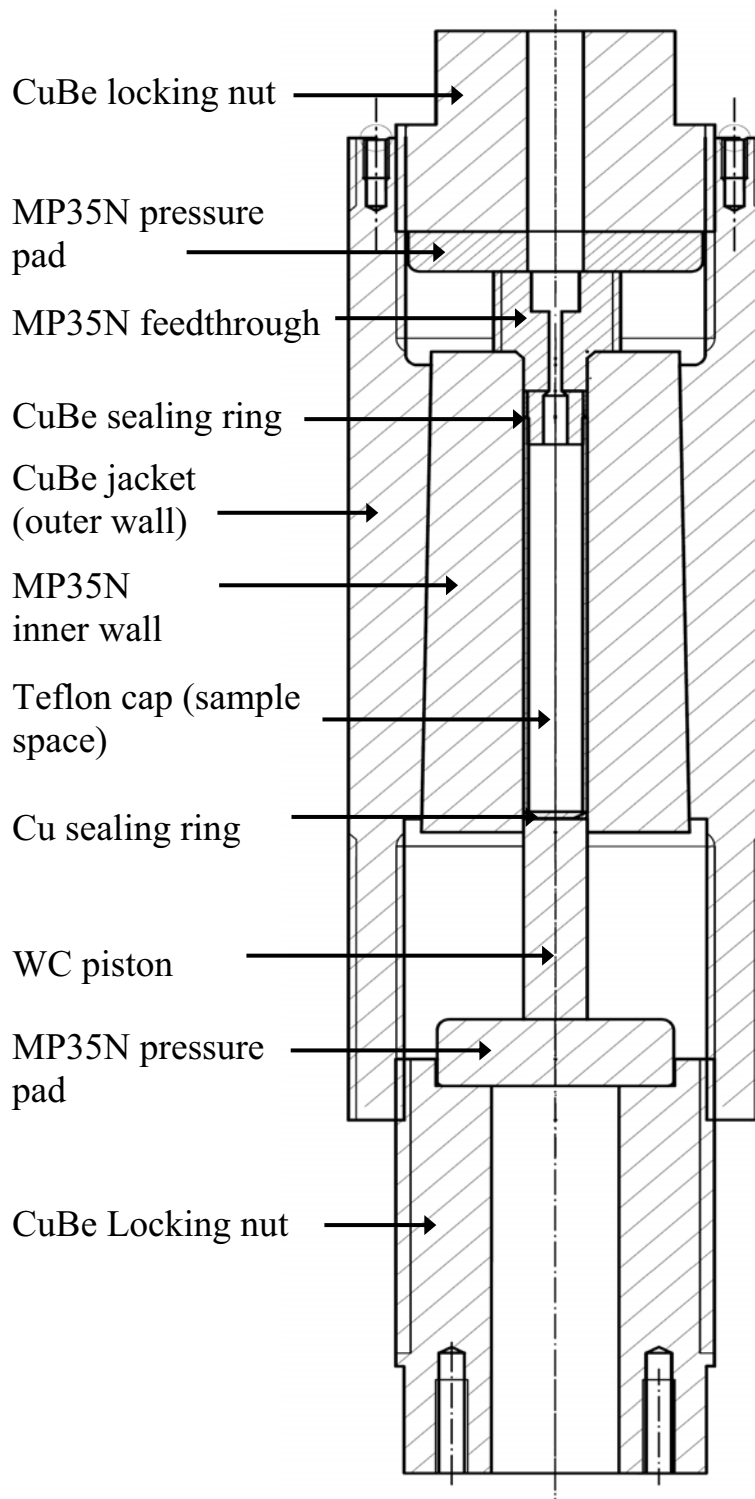
Figure 2.2: Schematic drawing of the double-wall piston-cylinder pressure cell used
in the resistivity studies.
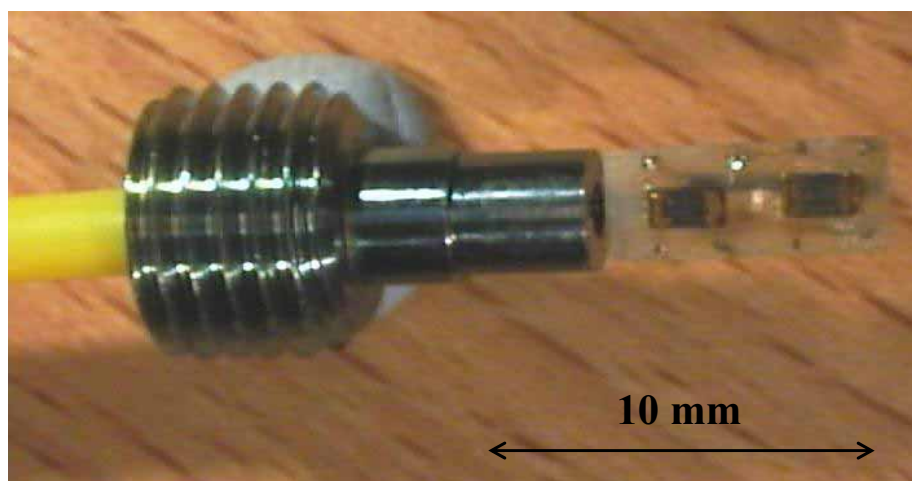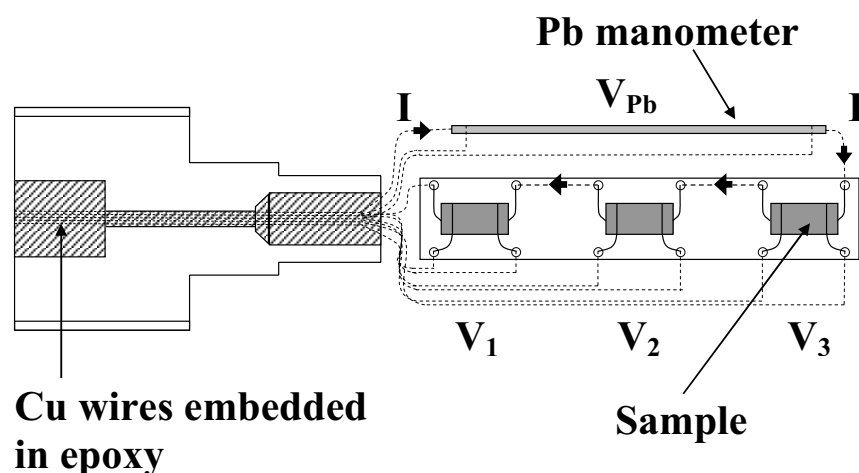
Figure 2.3: Upper panel: schematic of the feedthrough and the sample board. Lower panel: picture with the actual feedthrough with two $Tl_xV_6S_8$ samples and Pb (back side) on the board.

with a hydraulic press (from the lower part in Fig. 2.2) and kept by closing the locking nut. The force is transmitted to the sample space via a tungsten carbide (WC) piston. The samples are placed on a very thin fiber glass board inside a teflon cup filled with the pressure transmitting medium. The Cu wires used for the resistivity measurements are passing from the ambient pressure inside the sample space via the so called "feedthrough" shown in Fig. 2.3. This is the most delicate and vulnerable part of the pressure cell and special attention has to be given while building it. The wires are sealed inside the bore with a commercially available epoxy (Stycast 2850 FT

hardened with Catalyst 9 from Emerson & Cuming) using the vacuum-impregnation technique described in Ref. [59]. Great care has to be taken in cleaning the wires and degassing the epoxy.

Different fluids were tested as pressure transmitting media: fluorinert, Daphne oil, and a 1:1 mixture of iso-pentane and n-pentane. The latter is the only one which does not solidify under pressure at room temperature up to $p = 3.5$ GPa and assures the best hydrostatic conditions. The pressure inside the cell is determined by a resistive measurement of the superconducting transition temperature, T_c, of a lead sample (used as manometer) placed inside the cell, along the whole sample space. The $T_c(p)$ dependency is well established in the literature (Ref. [60]). Only for the alcohol mixture, the superconducting transition width of Pb has been found to be sharp (approx. 5 mK) and pressure independent. However, the disadvantage of this liquid is its very high volatility which makes it difficult to work with. Feedthroughs which are sealing fluorinert or Daphne oil are often found to be leaking when the alcohol mixture is used. This adds extra demands on the quality of the feedthrough construction but remains the best available option for this particular type of cell. Nevertheless, the fluorinert and the Daphne oil can also be used successfully for different constructions of the cells, with lower lenght/diameter ratios for the sample space.

Pressure cell characteristics:

○ inner bore: 4 mm;

○ sample space length: 25 mm;

○ maximum number of samples: 3 samples plus manometer;

○ maximum pressure: 3GPa.

2.2.1   MP35N

A limiting and difficult to control factor in determining the upper pressure limit is the material used to build the inner body of the double-wall pressure cell. We used

MP35N, but a thorough study revealed that its mechanical properties are strongly dependent on two factors: the amount of cold-work (primary hardening) and the heat treatment (secondary hardening). MP35N is a metallic alloy containing: 35% Co, 35% Ni, 20% Cr and 10% Mo. An extensive study of its mechanical properties can be found in [61–64].

MP35N, when fully annealed at $T > 850$ °C is a single phase solid solution with *fcc* structure. It is a low stacking fault energy (SFE) alloy with a high strength and high ductility and remarkably stable against corrosion.
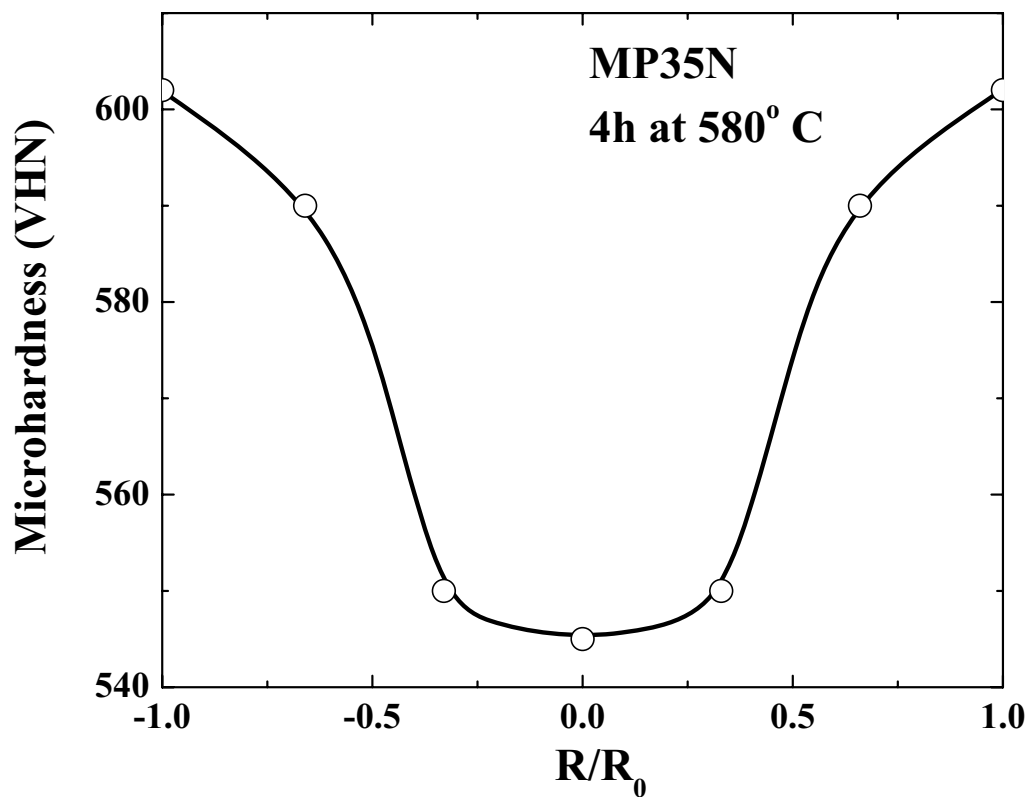
Figure 2.4: Microhardness of a cylindrical sample of MP35N as a function of relative distance R/R_0 to the center.

MP35N is commercially available cold-drawn with a volume reduction of 53%. However the cold-drawing in cylindrical shape compresses mostly the outer parts of the material leaving the inner part soft. We measured the microhardness of disk shaped samples (with the diameter of $2R_0 \approx 1.2$ cm) of MP35N prior and after the heat treatment. We always found a significant hardening reduction (approx. 10%)

in the middle of the sample as depicted in Fig. 2.4. This feature is of increasing importance for smaller pressure cells.

In summary, the following remarks are important to be considered when designing a pressure cell of this type:

○ final hardening depends primarily on the amount of cold work;

○ for high performance pressure cells, MP35N with a volume reduction of about 65% is required;

○ optimum heat treatment: 4 hours at 590 ºC. Extended aging gives no extra hardening.

○ for small inner bore pressure cells, cold-rolled MP35N is preferable to the cold-drawn one due to an accentuate hardness reduction in the latter case in the middle of the rod.

2.3 Uniaxial stress pressure cell

The AC specific heat measurements under uniaxial stress on the cubic heavy-fermion UBe_{13} presented in this work were performed in a pressure cell developed by B. Wand [65] (Fig. 2.5).

This pressure cell, accommodated in a ^{3}He refrigerator, allows to modify in situ the uniaxial stress applied to a sample situated between two stainless steel anvils. A mixture of ^{3}He and ^{4}He from a pressure reservoir is applied via a very thin capillary to the bellows situated at low temperature. A proportional-integral pressure regulator at room temperature was added to the system allowing to keep the pressure constant within 10^{-4} GPa during a measurement. The force was calibrated in situ using a piezoceramic sensor so that also friction effects were accounted for. The spring system in Fig. 2.5 keeps the upper and lower anvils always perfectly parallel one to each other. The uniaxial pressure depends on the sample cross section and its upper limit is, in general, given by the mechanical strength of the sample. In order to prevent the
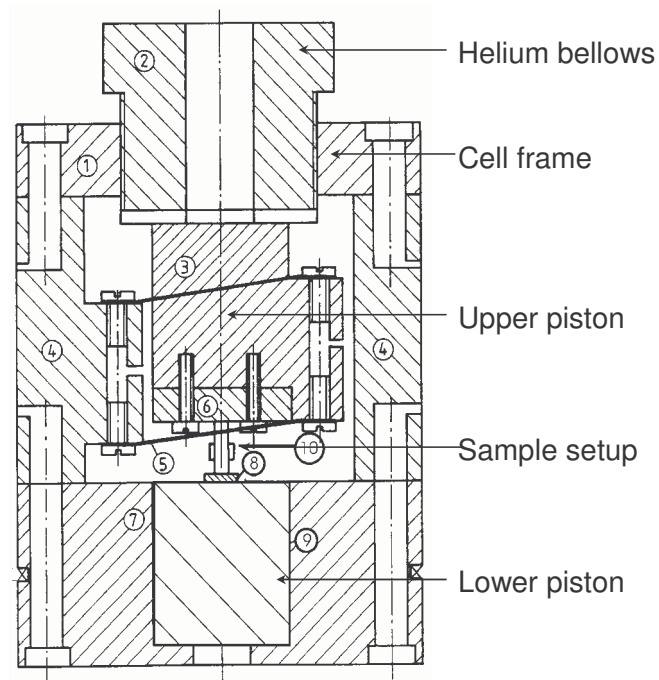
Figure 2.5: Sketch of the uniaxial pressure cell. Ref. [65].
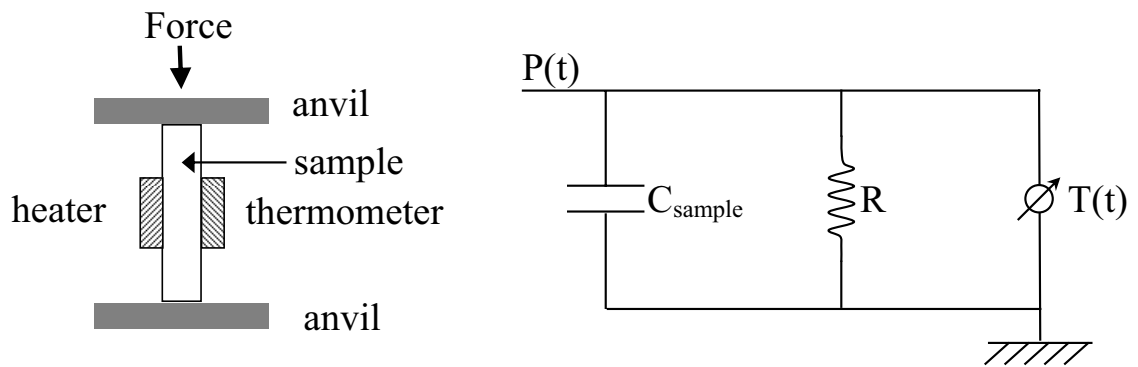
Figure 2.6: Left panel: Sketch of the sample setup. Right panel: equivalent electrical circuit.

crystal from breaking and also to allow some sideways movement, we used copper foil and capton tape between the sample and the anvils. For the AC specific heat measurements under uniaxial stress, a heater ($10\,\mathrm{k\Omega}$ SMD resistor) and a thermometer ($2.2\,\mathrm{k\Omega}$ RuO$_2$ thick-film SMD resistor) were glued with silver paste on the opposite

sides of the sample, as schematically depicted in Fig. 2.6 left panel. Assuming that the thermal resistances between thermometer-sample and heater-sample are negligible compared to the sample-bath contact and neglecting the thermometer and heater heat capacity, the equivalent electrical circuit is shown in the right panel of Fig. 2.6, where R depends on the internal (τ_i) and external (τ_e) relaxation times. τ_i describes the internal equilibrium of the sample, including the heater and the thermometer and depends on the sample thermal conductivity and geometry. τ_e describes the equilibrium between the sample and the surrounding and is mainly given by the thermal link to the bath (cryostat). τ_e can be adjusted by properly choosing the type of materials placed in between sample and anvils.

An oscillating heating power $P(t) = P_0 + P_1 \cos(\omega t)$ is applied through the heater, generating oscillation of the sample temperature with an amplitude ΔT_{ac}. The sample heat capacity is then given by:

$$C_{sample} = \frac{P_1}{\omega \Delta T_{ac}} F(\omega, \tau_i, \tau_e) \quad \text{[66]}. \tag{2.1}$$

As can be seen, F depends on the thermal contact to the bath (through τ_e) which is constantly improved upon increasing pressure. Therefore great attention had to be paid to the frequency response of the AC signal. A detailed description of the AC specific heat method is given in [66].

Chapter 3

Possible Fulde-Ferrell-Larkin-Ovchinnikov state in the heavy-fermion compound CeCoIn$_5$

3.1 CeCoIn$_5$ a good candidate for the FFLO state formation

The Fulde-Ferrell-Larkin-Ovchinnikov(FFLO) phase is expected to be realized at low temperatures ($T \leq 0.56\ T_c$ [39]) and high magnetic fields in a type-II singlet superconductor in the clean-limit and for which the Pauli paramagnetism dominates the orbital currents in limiting the upper critical field (Maki parameter $\alpha > 1.8$). In this inhomogeneous superconducting phase, situated between the normal and the vortex state, part of the Cooper pairs are broken on certain regions asymmetrically distributed around the Fermi-surface. Consequently it is necessary for the remaining paired electrons to establish a counterflow current exactly canceling out that of the unpaired electrons. Therefore, the Cooper pairs form with a finite momentum $\mathbf{q}$, in a ($\mathbf{k} \uparrow, (-\mathbf{k} + \mathbf{q}) \downarrow$) state instead of the conventional ($\mathbf{k} \uparrow, -\mathbf{k} \downarrow$) pairing, where $\mathbf{k}$ is the momentum of the one electron wave function. This leads to an unusual spatially modulated order parameter with a wavelength, in the vicinity of the upper critical field, equal to $2\pi/|\mathbf{q}|$, meaning that the normal and the SC regions of the material are

placed alternately perpendicular to the magnetic field and the vortices. The size of the SC regions depends on the pairing momentum $\mathbf{q}$. However, the realization of such a state in conventional s-wave superconductors is almost impossible [41]. Gruenberg and Gunther [36] showed that the FFLO state can be realized even in the presence of the orbital term and their ansatz plays a crucial role, since it is valid for d-wave or other nodal superconductors as well. For a more thorough introduction to the FFLO state see Chapter 1.1.

Though predicted by theory more than four decades ago [5, 6], the FFLO phase proved to be elusive to the experiments and therefore has been constituting an increasing challenge for the physicists, especially in the last few years. Although several compounds have been proposed as likely candidates for the formation of such a state, subsequent analysis has called the interpretation of the data into question.

The prerequisites for the realization of the FFLO phase are extremely difficult to achieve in any known superconductor but recently a new promising system has been found in $CeCoIn_5$ [1] which seems to meet in an ideal way all the requirements.

3.1.1   Crystal structure and basic properties

$CeCoIn_5$ belongs to the heavy-fermion family of $CeTIn_5$ (T = Co, Rh, or Ir) compounds crystallizing in the tetragonal $HoCoGa_5$ crystal structure, with the lattice constants $a = b = 4.614$ Å and $c = 7.552$ Å [67, 68]. The structure, analogous to its isostructural relatives $CeRhIn_5$ and $CeIrIn_5$, is built up by single layers of $CeIn_3$ and $CoIn_2$ stacked alternatively along the c-axis. It has two crystallographically inequivalent In sites. The first one (In(1)), surrounded by Ce atoms, is located in the Ce-In plane and has a symmetry which is invariant under four-fold rotations relative to the c-axis. The second (In(2)) site, surrounded by both, Ce and Co ions, has a lower crystal symmetry. Due to the anisotropic environment, a large electric field gradient is expected for both In positions (Fig. 3.1).

A rather remarkable characteristic of this family of materials is their instability to superconductivity. $CeCoIn_5$ and $CeIrIn_5$ are superconductors at ambient pressure below $T_c = 2.3$ K [1] and $T_c = 0.4$ K [69], respectively, while for $CeRhIn_5$ the super-

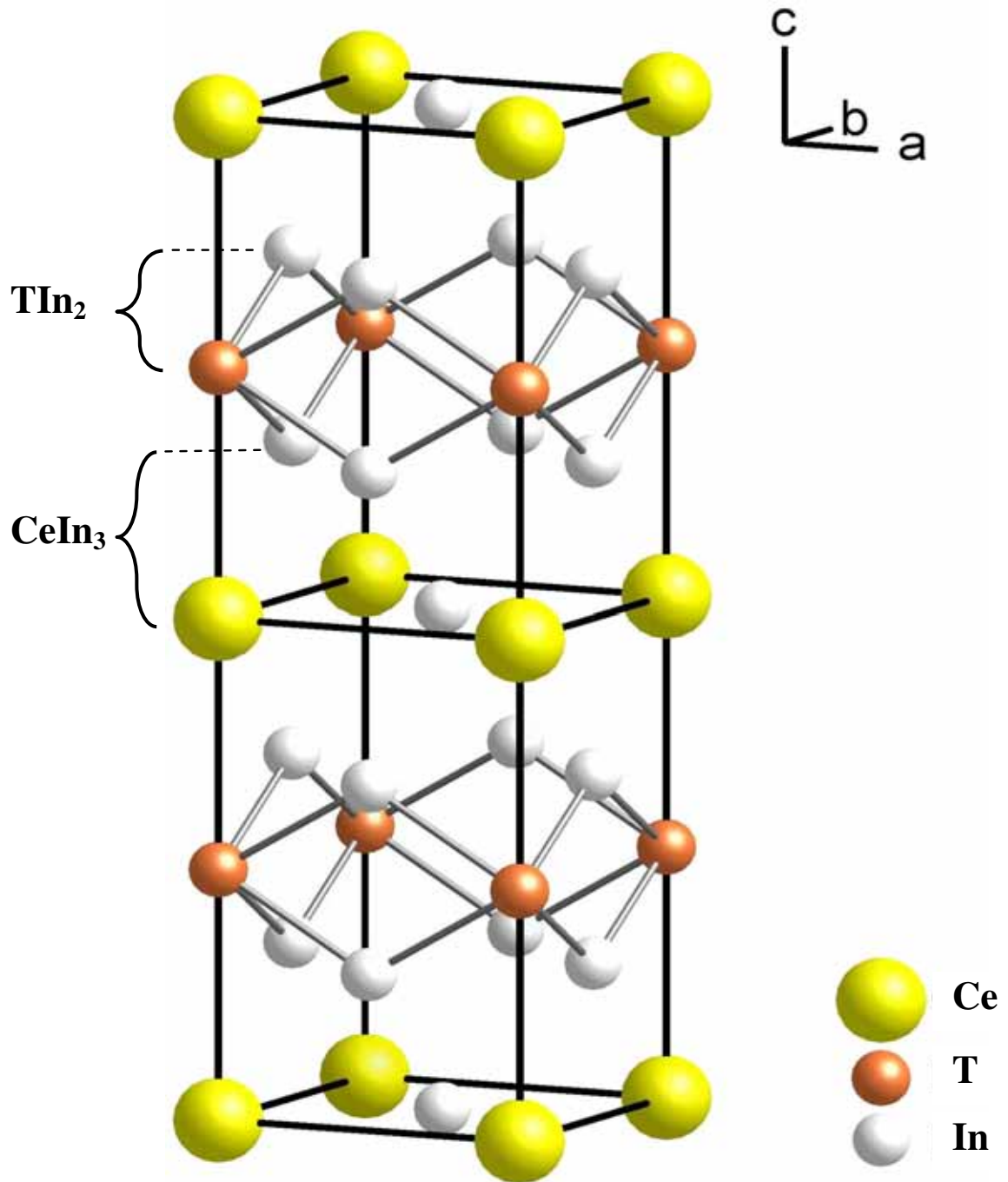Figure 3.1: The crystal structure of the CeTIn$_5$ family. The structure is built up of alternating layers of CeIn$_3$ and TIn$_2$.

conductivity is induced only upon applying pressure: $T_c = 2.12$ K at $p = 2.1$ GPa [70]. In each case, superconductivity develops out of a highly correlated state with a large specific heat coefficient γ and in proximity to antiferromagnetism. Rh substitution

into $CeCo_{1-x}Rh_xIn_5$ [71] and in $CeIr_{1-x}Rh_xIn_5$ [72] induces antiferromagnetic order in both compounds. However $CeRhIn_5$ is the only one in the family showing static long range antiferromagnetic order with a Néel temperature $T_N = 3.8$ K.

3.1.2   Quasi-2D electronic structure

The unique tetragonal layered crystal structure is responsible for producing the pronounced electronic anisotropy in $CeCoIn_5$. This compound has a quasi-2D electronic structure with a highly anisotropic Fermi-surface composed by small ellipsoidal regions dominated by slightly warped cylindrical sheets (Fig. 3.2 [68, 73–75]). $CeCoIn_5$ is a compensated metal, with equal volumes of electron and hole Fermi-surfaces. The main features of the Fermi-surface topology, determined from de Haas-van Alphen (dHvA) measurements, on the basis of the itinerant $4f$ band model, are the branches:

- α_i ($i = 1, 2, 3$): approximately cylindrical band 15-electron,

- β_i (i = 1,2) and η: a highly corrugated but cylindrical band 14-hole.

This important electronic structure anisotropy affects as well the physical properties: resistivity, susceptibility, thermal conductivity, NQR, penetration depth, etc.. The upper critical field at $T = 0$ K is a factor of two bigger for $B \parallel (a,b)$-plane ($B_{c2}(0) = 11.6$ T [3]) relative to the $B_{c2}(0) = 4.9$ T value obtained for the $B \parallel c$ case. [3]. The important anisotropy of B_{c2} is well explained by an effective mass strongly direction dependent. The large cyclotronic effective masses of $m^* \approx 100 \, m_0$ [68], where m_0 is the free electron mass, confirmed by the dHvA measurements are consistent with the large electronic specific heat.

Most likely the superconductivity originates on the cylindrical sheets of the Fermi-surface, with negligible transfer of the order parameter onto the three-dimensional pockets [76] as suggested by the negligible damping in the superconducting state for the ϵ-orbit over the band 13, in contrast to the strong damping observed for the α- and β-orbits over band 14 and 15 sheets [68]. Moreover, the reduced dimensionality is believed to favor the magnetically mediated superconductivity. When the magnetic interactions are quasi-2D, there is a line of soft magnetic fluctuations in the Brillouin
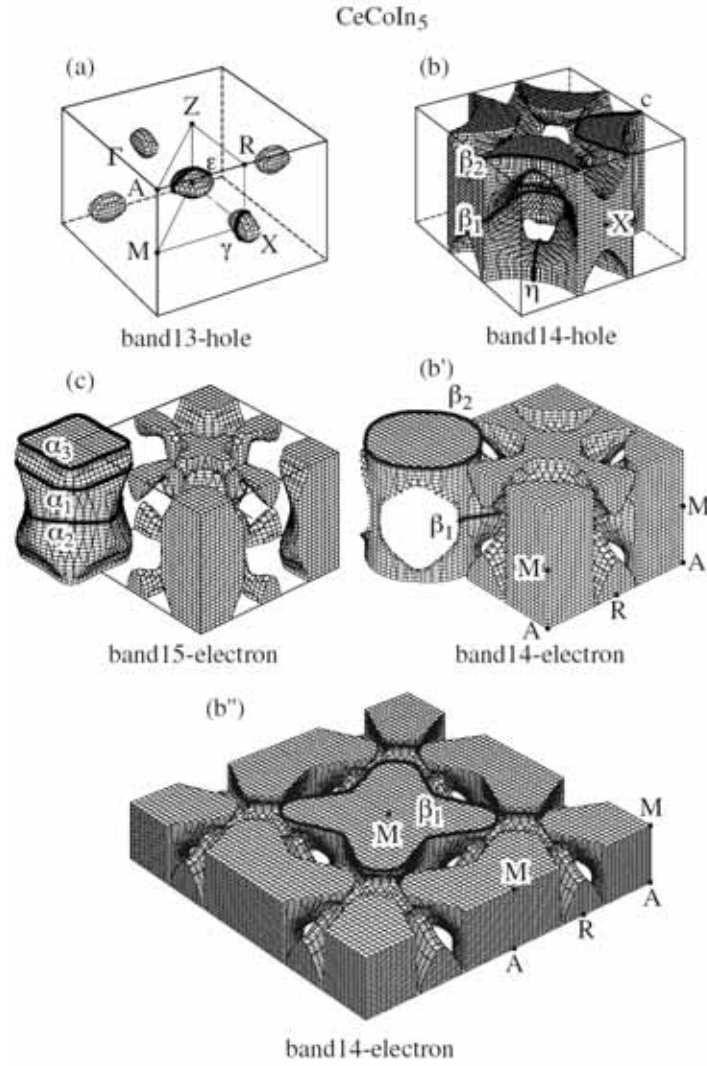
Figure 3.2: Fermi-surface dominated by nearly cylindrical sheets. From Ref. [73].

zone, whereas there is only a point when the magnetism is fully 3D. This leads to an enhanced coupling to magnetic fluctuations in quasi-2D systems relative to their 3D counterparts. This not only favors higher transition temperatures in quasi-2D materials but also greater robustness of pairing to material imperfections and other competing interaction channels such as electron-phonon scattering.

3.1.3 Unconventional superconductivity

Even from its discovery, CeCoIn$_5$ proved to be a remarkable heavy-fermion compound. It is superconducting at ambient pressure with a transition temperature $T_c = 2.3$ K,
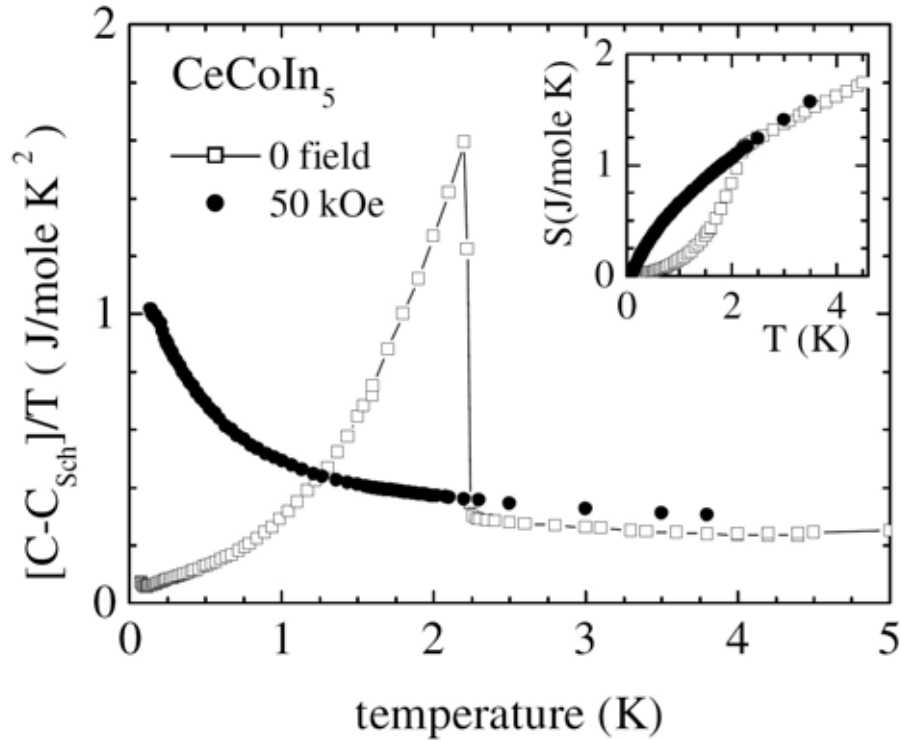
Figure 3.3: The electronic specific heat divided by temperature for CeCoIn$_5$, at ambient pressure and in zero magnetic field (open squares) and for $B = 5$ T ($B \parallel c$) above the upper critical field (solid circles). The inset shows the entropy recovered as a function of temperature in the superconducting (open squares) and field-induced normal (solid circles) state. From Ref. [1].

the highest among the Ce based heavy-fermion systems. The specific heat divided by temperature C/T at normal pressure and in zero field is shown in Fig. 3.3. The large $\gamma = C/T = 0.290$ J/(molK^2) $\propto m^*$ in the normal state, just above the superconducting transition ($T = 2.5$ K), indicates a substantial mass renormalization. The jump in the specific heat at T_c is remarkably high, the inferred value of $\Delta C/\gamma T_c = 4.5$ suggesting very strong coupling. In contrast, the expected value for a weak coupling superconductor is only $\Delta C/\gamma T_c = 1.43$ (from BCS-theory). However, this large jump has to be considered carefully since the superconductivity sets in while the heavy-fermion state is not yet completely formed with the effective mass m^* still increasing upon lowering the temperature. This was described based on a phenomenological two-fluid description of the Kondo lattice [77]: the high temperature gas of nonin-

teracting Kondo centers starts to condense into a coherent heavy-fermion fluid below a characteristic temperature corresponding to the intersite coupling scale. However, this condensation is partial, and a residual single ion component of the incoherent Kondo impurity fluid survives down to very low temperatures, well below the single-ion Kondo temperature T_K, where it seems plausible to eventually condensate into the heavy-fermion ground state albeit inducing unusual behavior in the system [77].

There is even more growing evidence that superconductivity in CeCoIn$_5$ is unconventional. The low temperature electronic specific heat, $(C-C_{Schottky})/T$, displays an anomalous behavior. The In quadrupolar nuclear Schottky contribution was subtracted based on the energy levels determined by nuclear quadrupole resonance (NQR) [78]. The electronic specific heat as function of temperature is non-exponential in the superconducting state and in the low temperature range 0.095 K $\leq T \leq 0.400$ K is given by:

$$(C - C_{Schottky})(\text{J}/(\text{molK})) = 0.04T + 0.25T^2 \ [79].$$ (3.1)

The low-T upturn in the data might be related to the entropy revealed at reduced temperatures when the superconducting state is suppressed in a field $B = 5$ T applied along the c-axis. The T^2 term in the electronic specific heat below T_c, observed as well in a number of unconventional superconductors including both, heavy-fermion systems (UPt$_3$ [80], CeIrIn$_5$ [79], CeRhIn$_5$ [70]) and high-T_c cuprates (YBa$_2$CuO$_7$ [81], La$_2$CuO$_4$ [82]), is a signature of lines of nodes presence in the energy gap.

The thermal conductivity (κ) in CeCoIn$_5$ (Fig. 3.4) shows a maximum around $T = 0.7$ K where its value is a factor of 15 above the upper limit of the phonon thermal conductivity (dotted line). In the normal state, κ is dominated by electrons which, at T_c, contribute over 90 % of the total κ value. Therefore, the maximum in κ is mostly electronic in origin, probably similar to the thermal conductivity peak observed in the high-T_c compounds. At very low temperature (0.033 K$< T <$ 0.100 K), the thermal conductivity follows a $\kappa = \text{const} \cdot T^{3.37}$ behavior (inset Fig. 3.4) close to the T^3 dependency predicted for unconventional superconductors, in the clean-limit and with nodal structure in the superconducting gap [79, 83].
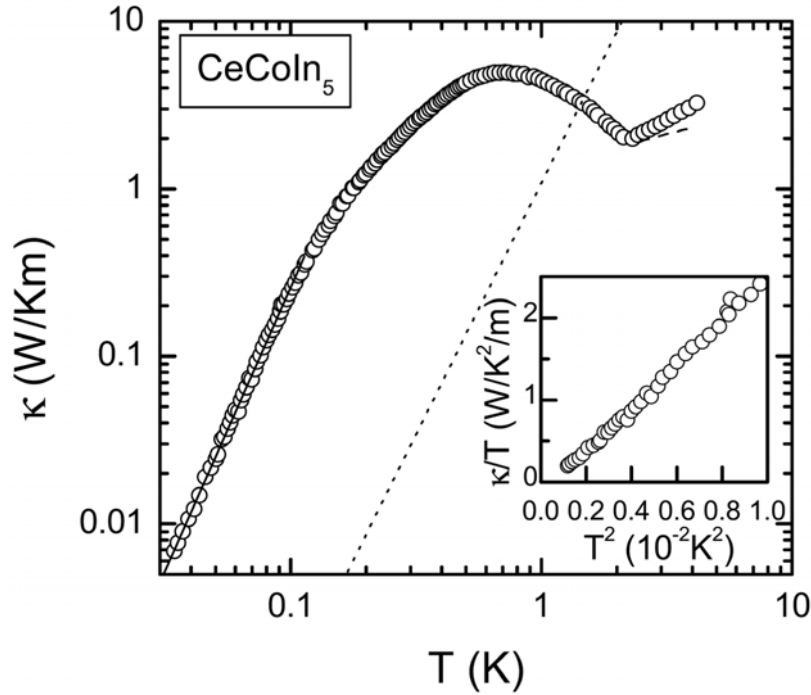
Figure 3.4: Thermal conductivity of CeCoIn$_5$. The dotted line is an upper limit estimate of the phonon contribution. Inset: $\kappa/T(T^2)$ for $T < 0.1$ K. From Ref. [79].

Knight shift (K) studies reveal a strong anisotropy, between the $B \parallel (a, b)$ and the $B \parallel c$ case, higher than the one observed for the magnetic susceptibility χ [78, 84]. Interestingly K is significantly dropping immediately after the superconducting state sets in $(T < T_c)$ for the ^{115}In site (both $B \parallel (a, b)$ and $B \parallel c$ case) and for ^{59}Co $(B \parallel c)$ while K for ^{59}Co $(B \parallel (a, b))$ is positive and temperature independent, indicative that the shift for the Co ions is almost entirely determined by the orbital contribution (Fig. 3.5-a). An analysis of K in the case of even parity superconductivity

$$K \propto \chi \propto \int N(E) \frac{\partial f(E)}{\partial E} dE, \tag{3.2}$$

- where $N(E)$ is the density of states (DOS) and $f(E)$ is the Fermi distribution function - reproduces well the T dependency of the measured Knight shift (the solid lines in Fig. 3.5-a. It is important to remark that at very low temperature, $K(T)$ has a close to linear behavior arisen from low-energy excitations of the quasiparticles in the superconducting state, in support for the d-wave pairing.

Moreover, the spin-lattice relaxation rate $1/T_1$ obtained by NQR measurements

a)   **b)**
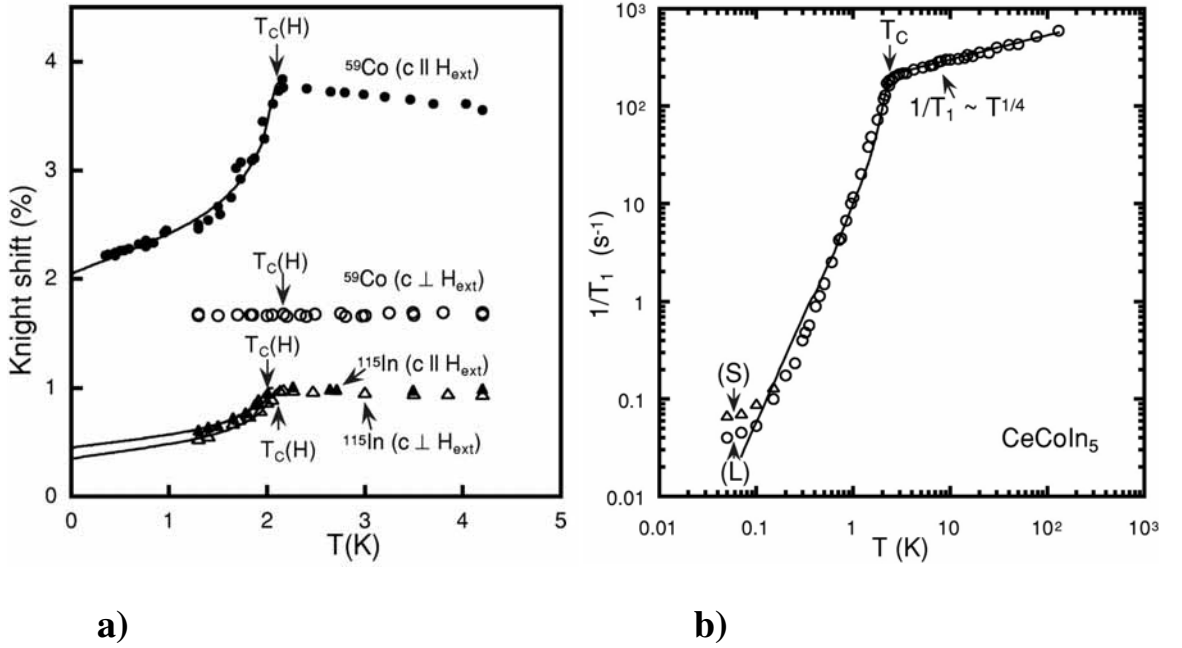
Figure 3.5: a) T dependence of the Knight shift for CeCoIn$_5$ in the superconducting state. The solid line represents an estimation of $K(T)$ for spin-singlet pairing. b) The NQR spin-lattice relaxation rate $1/T_1(T)$. The solid line is a $1/T_1 \propto T^3$ fit. For $T < 0.2$ K the relaxation rate tends to saturate. In the normal state $1/T_1 \propto T^{1/4}$. From Ref. [84].

[84] is approximately described by a $1/T_1 \propto T^3$ law (the solid line in Fig. 3.5-b, reminiscent of the relaxation behavior in many heavy-fermion superconductors: CeCu$_2$Si$_2$ [85], UBe$_{13}$ [86], UPt$_3$ [87], UPd$_2$Al$_3$ [88] and URu$_2$Si$_2$ [89]. For $T < 0.2$ K the relaxation rate tends to saturate. In CeCoIn$_5$ as well as in its relative compound CeIrIn$_5$, no Hebel-Slichter coherence peak is observed as would have been expected for conventional superconductors.

The superconducting penetration depth (λ) displays also unconventional behavior and reveals an significant anisotropy. While the in-plane $\lambda_\parallel$ ($B \parallel (a,b)$) tends to follow a power-law $\lambda_\parallel \propto T^{3/2}$ below $T = 0.8$ K, it was argued that a better description of the data would be a crossover from quadratic ($T < T^*$) to linear ($T > T^*$) behavior, with the crossover temperature $T^* = 0.32$ K in the strong coupling limit [91]. There are two routes to provide such a crossover: non-local effects or impurity scattering. With the latter scenario ruled out by a $\lambda_\perp$ ($B \perp (a,b)$) linear in T and a T^* five-times higher than the T^* value yielded by a dirty-limit d-wave model, the pen-

etration depth measurements constitute strong evidence for non-locality and d-wave superconductivity with lines of nodes along the c-axis in CeCoIn$_5$.

In conclusion, the power-law behaviors found deep in the superconducting state, summarized in Table 3.1, are those expected of an order parameter with line nodes and suggest unconventional spin singlet superconductivity. Indeed, thermal conductivity κ measurements find a prominent four-fold modulation in κ as a magnetic field is rotated in the basal plane [90]. The amplitude of the four-fold term increases by an order of magnitude at $T < 0.25$ K compared to the normal state. It was suggested by Izawa et $al.$ [90] that the four-fold symmetry is arising from the Andreev scattering off
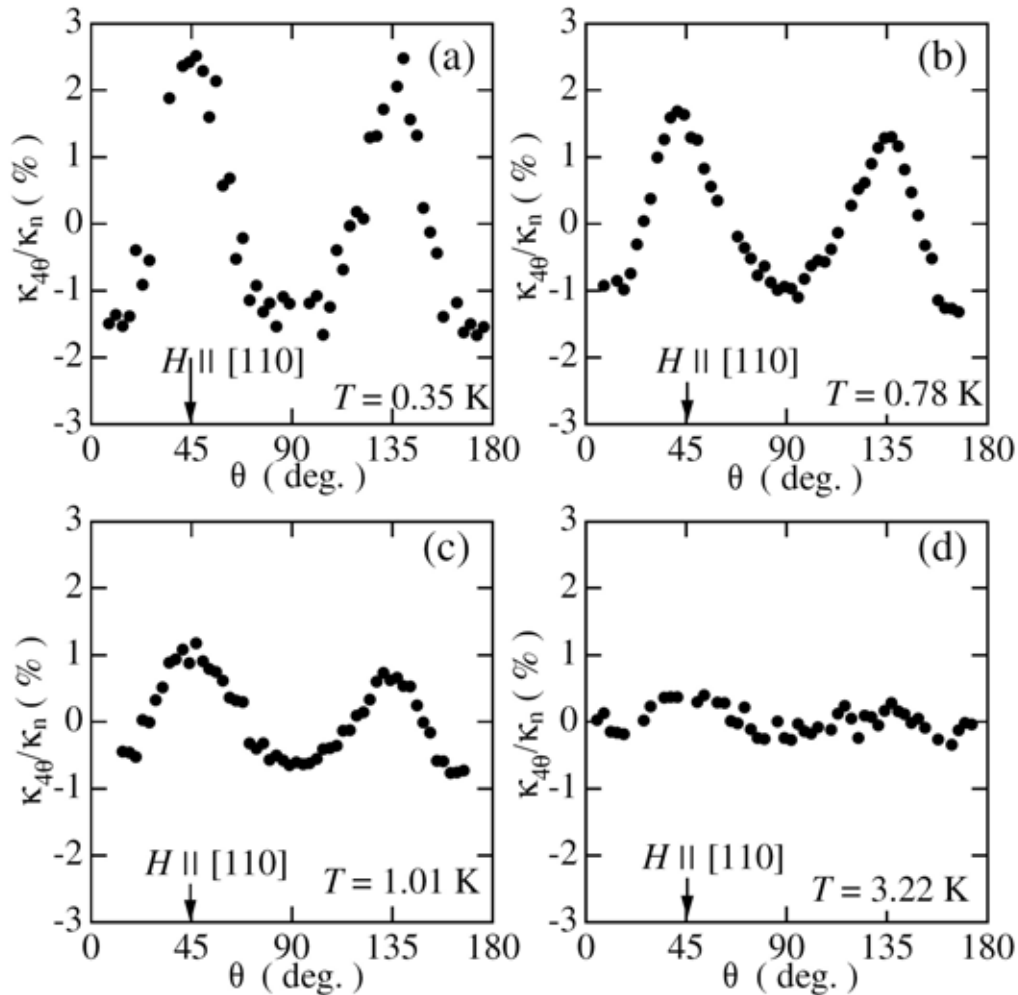

Figure 3.6: Four-fold symmetry revealed by thermal conductivity at several temperatures. From Ref. [90].

Table 3.1: Power-law behavior in the superconducting state in CeCoIn$_5$ and related compounds.

Compound	C/T	κ	$1/T_1$	λ	K
CeCoIn$_5$	T [79]	$T^{3.37}$ [79]	T^3 [84]	$\lambda_\parallel \propto T^{3/2}$, $\lambda_\perp \propto T$ [91] $T^{1.5}$ [92] T [93] $T^{1.65\pm0.2}$ [94]	T [84]
CeIrIn$_5$	T [79]	T^3 [79]	T^3 [84]	$T^{1.5\pm0.2}$ [94]	-
CeRhIn$_5$ at 2.1 GPa	T [70]	-	T^3 [95]	-	-

the vortex lattice which has a symmetry related to the gap function [96, 97]. κ attains a maximum value when B is parallel to the nodal directions and has a minimum when B is directed along the antinodal lines. Therefore, the gap has nodes at every 90º in k-space as seen in Figure 3.6. The magnitude and location of maxima in $k(\theta)$ (where $\theta = \widehat{(q, B)}$) are consistent with an order parameter having $d_{x^2-y^2}$ symmetry with zeros along the $(\pm\pi, \pm\pi)$ positions, similar to the high-T_c cuprates. However, the field-angle dependence of the zero-energy density of states determined by specific heat measurements point to a d_{xy} symmetry [98].

The flux-line lattice (FLL) found to be hexagonal at very low fields, undergoes around $B = 0.6$ T ($B \parallel c$), a transition, most likely of first-order, to a square symmetry with the nearest neighbors oriented along the gap node directions, consistent with a d-wave order parameter [99].

Unconventional superconductivity is displayed, as well, by the other members of the CeTIn$_5$ family as seen in Table 3.1.

3.1.4 Clean-limit superconductor

CeCoIn$_5$ is a clean superconductor with a low value of resistivity just above the superconducting phase transition $\rho_0 = 3$ $\mu\Omega$cm [1] and a very high ratio between the mean-free path (ℓ_{tr}) and the coherence length (ξ_0) of $\ell_{tr}/\xi_0 = 14$ [79]. Moreover, the

impurity band width, estimated from thermal conductivity, is less than 30 mK [79]. An upper limit estimate of the impurity concentration [100] that would give rise to such a narrow impurity band is $n_{imp} = 20$ ppm in the unitary scattering limit. In the Born limit this value would be increased to $n_{imp} = 20$ ppt but it was argued [1] that CeCoIn$_5$ is closer to the unitary scattering limit.

3.1.5 Pauli-limited SC and signatures of the FFLO state

In the case of a superconductor for which the orbital effect as pair breaking mechanism can be neglected relative to the Pauli paramagnetism, it was predicted by theory that the superconducting transition changes, upon increasing magnetic field, from second- to first-order, for $T < 0.55 \, T_c$ [15, 16]. This scenario which eluded the experimental probing for almost forty years was recently confirmed in CeCoIn$_5$ [3, 101].
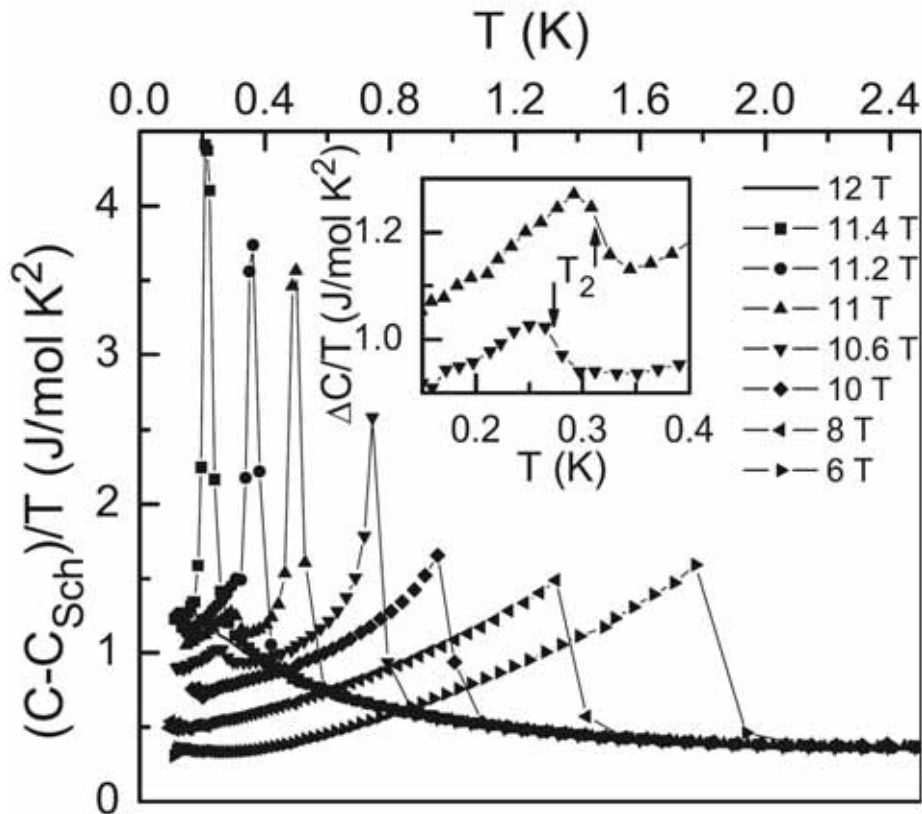

Figure 3.7: Specific heat as function of T at different fields with $B \parallel$ [110]. Upon increasing the field the superconducting transition changes from second- to first-order and a second anomaly at low-T (emphasized in the inset) is induced. From Ref. [3].

With the magnetic field perpendicular to the (a,b)-plane, the superconducting transition changes from second- to first-order at $B_0 \approx 4.7$ T which corresponds to $T_0 \approx 0.75$ K [101]. A similar situation, depicted in Fig. 3.7, has been found for the field in the (a,b)-plane at $B_0 \approx 10$ T and $T_0 \approx 1$ K [3].

The first-order character of the phase transition suggested by the sharpening of the specific heat anomaly and the increase of the peak value of $(C - C_{Sch})/T$ at $T = T_0$, is confirmed by the hysteretic behavior in specific heat and magnetization [102], and as well by magnetocaloric [101] and thermal expansion measurements [103, 104]. Moreover, as expected, a step-like feature in the entropy develops once the transition becomes first-order (inset Fig. 3.8-a [101]).

The Maki parameter assumes large values, considerably above the minimum required value of $\alpha = 1.8$ for the FFLO state formation, and reflects as well the pronounced anisotropy between the (a,b)-plane and the c-direction:

$\alpha \approx 3.6$ for $B \parallel c$,

$\alpha \approx 4.6$ for $B \parallel (a,b)$.

Indeed an anomaly at low temperature (T_{FFLO}) is observed in the specific heat measurements for both, $B \parallel (a,b)$ and $B \parallel c$ directions close to the upper critical field. This feature can be observed only inside the superconducting state and was ascribed to a transition into a FFLO phase [3]. For $B \parallel (a,b)$ this low-T phase could be resolved for 10.2 T $< B <$ 11.4 T while for the perpendicular field orientation it spans between 4.8 T $< B <$ 5 T. However, for $B \parallel c$ the T_{FFLO} feature is not resolved indisputably. The T_{FFLO} anomaly has a very weak field dependence as can be seen in the $B \parallel (a,b)$ phase diagram. A very small in-plane anisotropy for T_{FFLO} between the [110] and [100] directions can be observed as well, together with an anisotropy for $B_{c2}(0)$ of roughly 1% (Fig. 3.8). The $T_c(B)$ and the $T_{FFLO}(B)$ phase boundary lines meet at T^*:

$T^* \approx 0.130$ K for $B \parallel c$ [3],

$T^* \approx 0.310$ K for $B \parallel (a,b)$ [3].
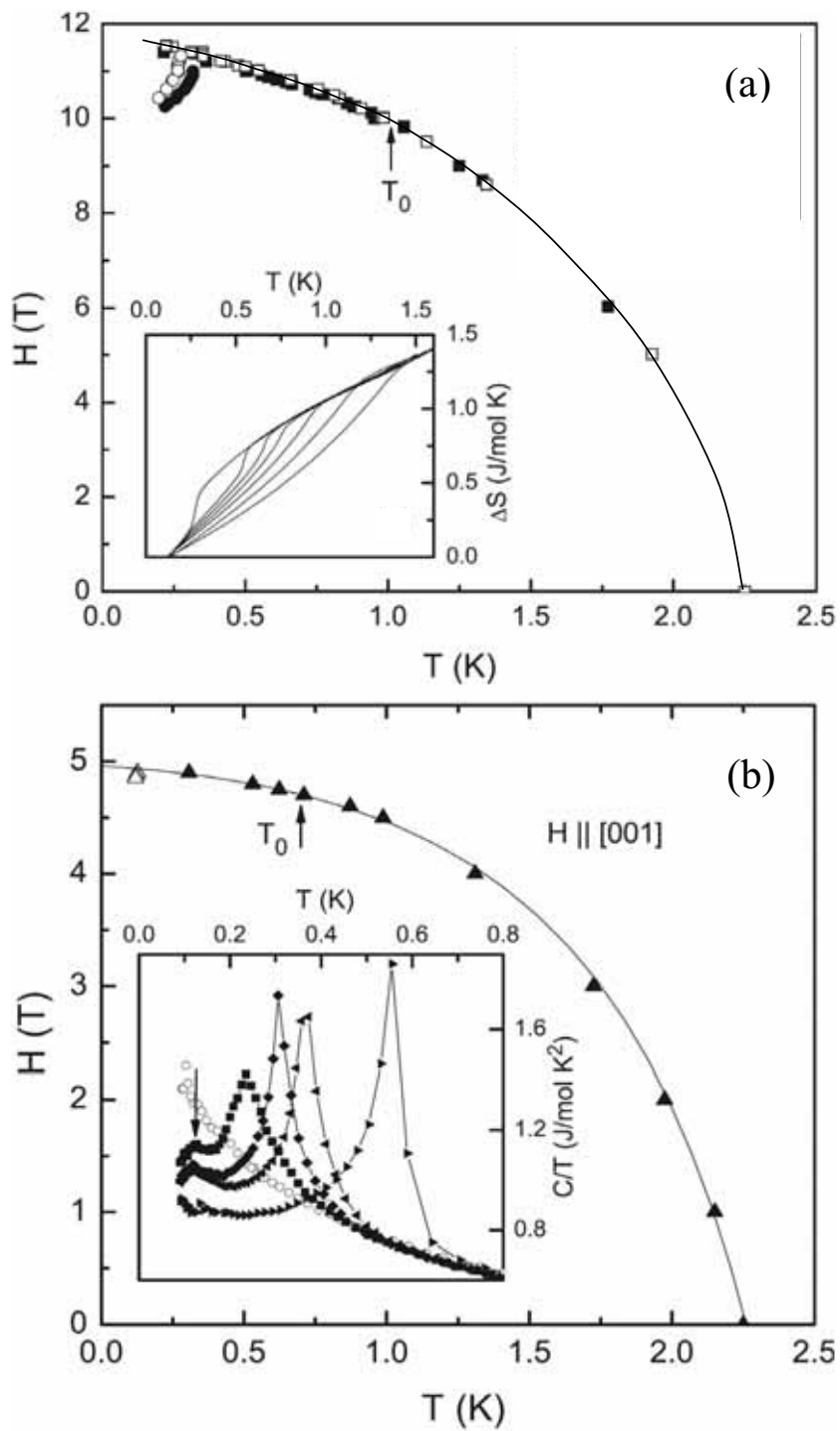
Figure 3.8:   (a). B_{c2} phase diagram for $B \parallel [110]$ (filled symbols) and $B \parallel [100]$ (open symbols). Inset: Entropy gain for $B = 11.4, 11, 10.8, 10.6, 10.2, 9.5$ and 8.6 T from left to right. (b). B_{c2} phase diagram for $B \parallel [001]$. Inset: $C(T)/T$ for $B = 4.9, 4.875, 4.85$ and 4.8 T from left to right. The arrow indicates the FFLO anomaly. From Ref. [3].
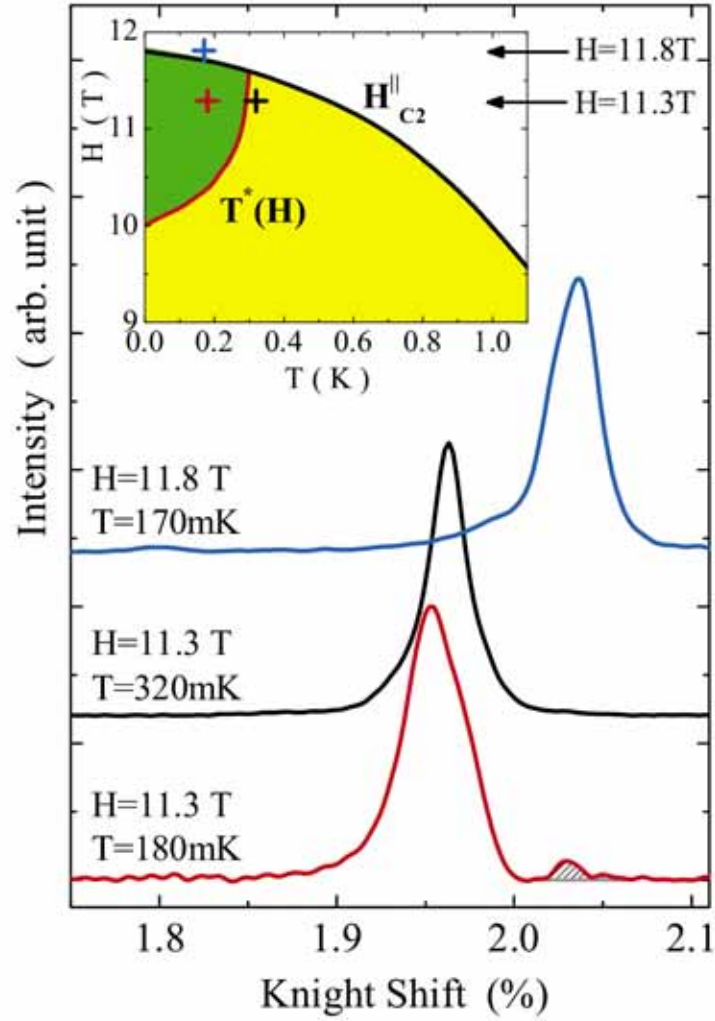
Figure 3.9: The ^{115}In-NMR spectra at different points in the phase diagram marked with "+" in the inset: - in the normal state, slightly above B_{c2} (upper spectrum); - in the classical superconducting state, close to the SC-FFLO boundary line (middle spectrum); - well inside the FFLO state (lower spectrum). From Ref. [108].

The much higher T^* value for $B \parallel (a, b)$ indicates that the FFLO state is more stable when the magnetic field is applied in the basal plane, as expected for this quasi-2D compound since in this direction orbital-limiting effects are less favored by the Fermi-surface geometry.

Moreover, the signature of the possible FFLO state was confirmed for $B \parallel (a, b)$ also by thermal conductivity [105], penetration depth [106] and ultrasound velocity measurements [107].

[115]In nuclear magnetic resonance studies provide first microscopic insight into the superconducting order parameter texture in $CeCoIn_5$ [108]. In the conventional superconducting state, at $B = 11.3$ T and $T = 0.320$ K, close to the SC-FFLO phase boundary, the NMR spectrum is almost symmetric as shown in Fig. 3.9, in the middle spectrum. This indicates that the influence of the field distribution inside the high-field superconducting region is negligible as the spatial distribution of the magnetic field, arising from the flux-line lattice structure, would produce an asymmetric NMR spectrum. Inside the presumed inhomogeneous superconducting state at $B = 11.3$ T and $T = 0.180$ K, the NMR spectrum has a remarkable feature: a new resonance peak appears, with small but finite intensity at higher frequency (dashed peak in the lower spectrum in Fig. 3.9). The intensity of this higher resonance is about $3\% - 5\%$ of the total intensity and is almost T-independent below $T = 0.180$ K. It was stressed by Kakuyanagi *et al.* [108] that, based on the different intensity of the two resonance lines, the higher frequency peak is unlikely to be generated by the occurrence of magnetic order.

Should antiferromagnetic order set in, the alternating hyperfine fields would produce two inequivalent ^{115}In(1) sites, which would generate two resonance lines with equal intensities. Moreover, an important characteristic of the NMR spectrum is that the small feature coincides rather well in frequency with the resonance line obtained in the normal state (upper spectrum in Fig. 3.9). Therefore it was argued that the higher resonance line observed in $CeCoIn_5$ is a manifestation of a novel normal quasiparticle structure in the low-temperature $-$ high-field region of the phase diagram, consistent with the formation of the FFLO state, where normal and the SC regions are expected to be placed alternately perpendicular to the magnetic field and the vortices.

3.2 Non-Fermi liquid behavior in the normal state in CeCoIn$_5$

Although no magnetic order is evident in CeCoIn$_5$ down to the lowest temperatures, the power-law behavior in the normal state observed for different physical properties show a non-Fermi liquid regime persisting over an extended temperature range.
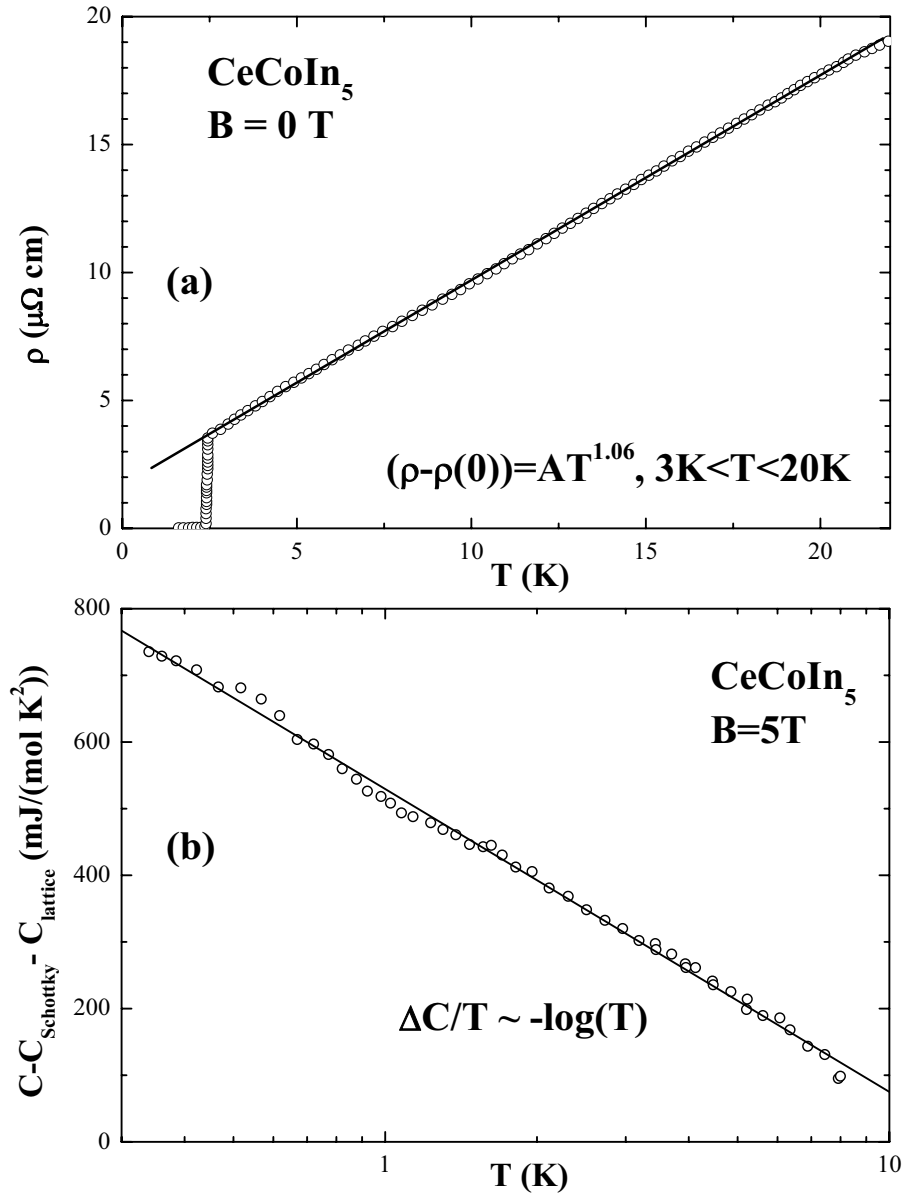

Figure 3.10: (a) The resistivity of CeCoIn$_5$ is linear for $T_c < T < 20$ K [109]. (b)The electronic specific heat $C/T \propto -\log(T)$ in the normal state [110].

Table 3.2: Power-law behavior in the normal state for different physical properties in CeCoIn$_5$ and related compounds indicating NFL behavior.

Compound	C/T	ρ	$1/T_1$	χ
CeCoIn$_5$	$-\ln(T)$ [1, 110]	$T^{1.0\pm0.1}$ [109, 111]	$T^{1/4}$ [84]	$T^{-0.42}, B \parallel c$ [110] $\frac{1}{\text{ct.}+AT^{0.1}}, B \perp c$ [110]
CeIrIn$_5$	$\gamma_0 - AT^{1/2}$ [110] $B = 6$ T	$T^{1.3}$ [69]	$\frac{T}{(T+0.86\text{K})^{1/2}}$ [84] $\frac{T}{(T+8\text{K})^{3/4}}$ [112]	$-\log(T)$ [110]
CeRhIn$_5$	-	T [113] $p = 3.2$ GPa	$\frac{T}{(T^*+1.5\text{K})^{1/2}}$ [95] $p = 2.1$ GPa	-

Specific heat measurements in a field $B = 5$ T parallel to the c-axis (the upper critical field for this orientation is $B = 4.95$ T) reveal an increase for C/T down to the lowest temperatures [1, 114]. The electronic specific heat obtained after subtracting the lattice and the Schottky contribution is plotted for $B = 5$ T in Fig. 3.10-(b) and shows $C/T \propto -\log(T)$ behavior for more than a decade in temperature. This dependence is associated with strong spin-fluctuations. Moreover, the temperature dependence of the electrical resistivity $\rho(T)$ in normal state is linear over an extended temperature range $T_c < T < 20$ K [1, 109, 115] (Fig. 3.10-(a)). The spin-fluctuation theory predicts for the nuclear spin-lattice relaxation rate, near an antiferromagnetic instability, a $1/T_1 \propto T^{1/4}$ dependence [116, 117], which is observed in CeCoIn$_5$ in the normal state (Fig. 3.5-(b)) [84].

For a Landau-Fermi liquid, $C/T \approx$ constant, $\Delta\rho = \rho(T) - \rho(0) \propto T^2$, $1/T_1 \propto T$ and $\chi \approx$ constant are expected at low temperatures. As summarized in Table 3.2, this is not the case for CeCoIn$_5$ and its related isostuctural compounds. The functional dependencies are strongly suggestive of NFL behavior induced by antiferromagnetic quantum critical fluctuations.

All this facts, corroborated with the comparison to the closely related anti-ferromagnet (ordering temperature $T_N = 3.8$ K) CeRhIn$_5$ [118], argue for a nearby quantum-critical point in CeCoIn$_5$ situated at an assumed slightly negative pressure.

3.3 Specific heat experiments under pressure and in magnetic field

All the prerequisites required by the FFLO state formation are met in CeCoIn$_5$: it is a very clean superconductor, Pauli-limited with a high Maki parameter ($\alpha >$ 1.8). Its reduced electronic dimensionality provides a path to lower orbital currents and favors magnetically mediated superconductivity. The d-wave symmetry of the superconducting order parameter would increase as well the stability of a FFLO state against impurities [32]. Moreover, the formation of a new phase at high magnetic fields and low temperatures is revealed by a number of experiments like specific heat and NMR measurements (see previous section).

However, this compound seems to be located close to a quantum critical point (QCP) manifested by the presence of strong antiferromagnetic fluctuations. This rises the possibility of a magnetic nature for the low-T anomaly which, in this case, would indicate the onset of an undisclosed type of magnetically ordered phase superseded by superconductivity.

In order to rule out the QCP-related origin of this phase, one has to drive the system away from the influence of the strong magnetic fluctuations. This is accomplished by applying hydrostatic pressure p as the system recovers Fermi liquid behavior for $p \geq 1.6$ GPa as indicated by resistivity [111, 119] and specific heat data [120]. Moreover, the residual resistivity ρ_0 is rapidly decreasing by almost two orders of magnitude from its atmospheric pressure value to $p \approx 1.4$ GPa, suggesting the suppression of spin-fluctuations [111]. Additional evidence for the damping of magnetic fluctuations with increasing pressure comes from dHvA [121] and NQR [122] studies under pressure. Therefore, hydrostatic pressure is an ideal tool to investigate the possible formation of the FFLO state in CeCoIn$_5$ while suppressing the strong magnetic fluctuations.

3.3.1   Heat capacity setup

To explore the nature of the low-T phase in CeCoIn$_5$ we measured specific heat under hydrostatic pressure, down to low temperatures and in high magnetic fields on high quality single crystals[1]. They were synthesized in In flux by combining stoichiometric amounts of Ce and Co in an alumina crucible and encapsulated in a quartz ampoule [1]. The single crystals grow in a plate-like geometry with the short side along the crystallographic c-axis. To cut the single crystals selected for the measurements a spark-erosion device was employed. The mass of the measured sample was $m = 1.532$ mg, i.e., $1.982 10^{-6}$ mol.

We used a new piston-cylinder type pressure cell, specially developed for this type of experiments, machined entirely from CuBe and described in more detail in the experimental introductory chapter. The reduced mass of the cell, of only 160 mg, and the absence of magnetic parts ensure a very high ratio between the sample and pressure cell (addenda) heat capacity and make this cell suitable to use even in high magnetic fields and low temperatures. A comparison between the heat capacity of the sample, addenda and the loaded cell is presented in Fig. 3.11 for a pressure of $p = 0.45$ GPa. At the maximum temperature, where the phononic contribution of the cell is highest, the sample represents 16% of the total (cell, pressure transmitting medium and sample) heat capacity and its contribution increases well above 50% at the top of the superconducting transition anomaly. At low-T, the sample heat capacity drops to around 15% of the total value. Under pressure and upon applying magnetic field the sample/addenda heat capacity ratio is further reduced, but remains at reasonably large values, significantly higher than observed for other standard pressure cells.

We used, as pressure transmitting medium, Pb and a very small amount of Apiezon-N grease. The pressure was determined by the inductively measured shift of the superconducting transition of the Pb inside the cell relative to a reference Pb sample placed outside the cell (inset Fig. 3.11). This shift was converted into pressure following the $T_c(p)$ calibration from Eiling *et al.* [60]. The relatively sharp superconducting transition of Pb and a comparison of the zero field data under pressure

---

[1]The single crystals were prepared in the group of Dr. J. L. Sarrao at Los Alamos National Laboratory, Los Alamos, USA.
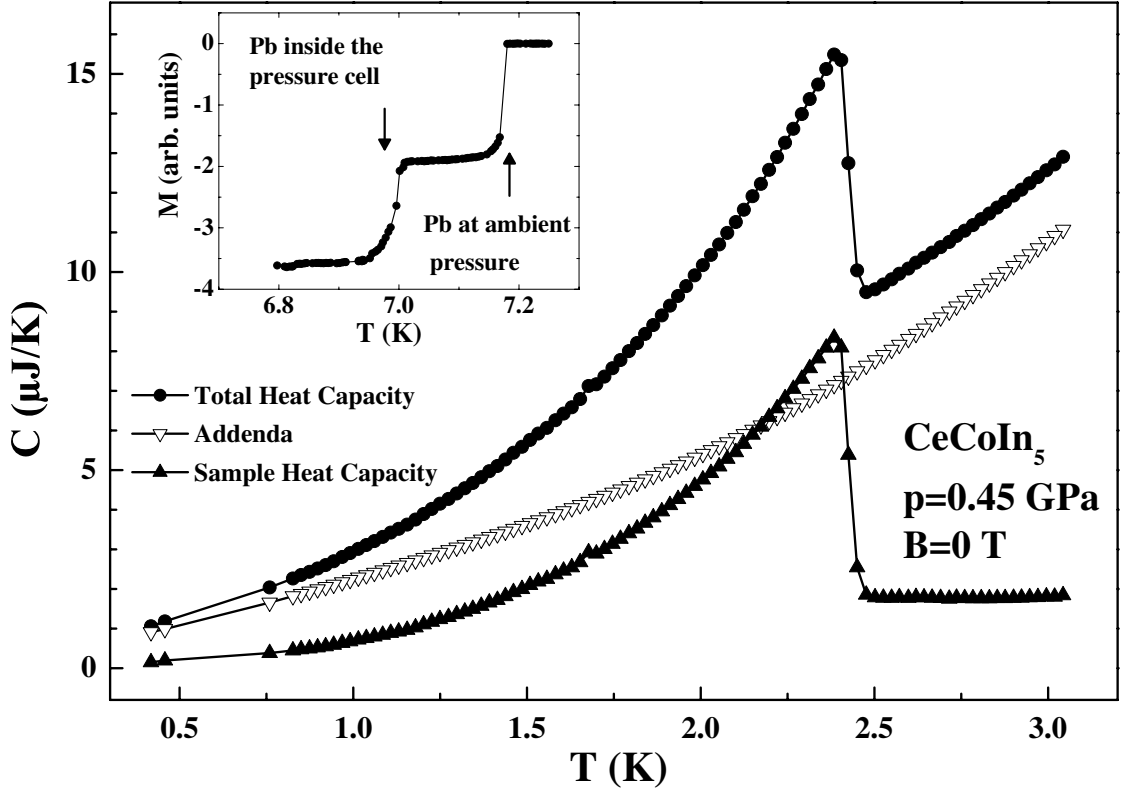
Figure 3.11: Comparison between the sample heat capacity and addenda. Total heat capacity is given by the cell, pressure transmitting medium and the sample.

with previous measurements where a liquid [120, 123] or argon gas [124] was used as pressure transmitting medium, confirm the good quasi-hydrostatic conditions of our setup.

3.3.2   Experimental results

The experiments were carried out with the magnetic field applied parallel to the (a, b)-plane as well as parallel to the c-axis. Temperatures down to $T = 0.1$ K and magnetic fields up to $B = 12$ T could be reached in a dilution refrigerator cryostat. A quasi-adiabatic specific heat measurement method was employed using a specially built specific heat platform made out of 80 μm thick silver foil suspended on thin nylon wires. At low temperatures $T < 0.2$ K and in high magnetic field, the Schottky contribution to the heat capacity coming from both, pressure cell (contains Cu and Be) and sample (contains In) becomes increasingly important. This causes
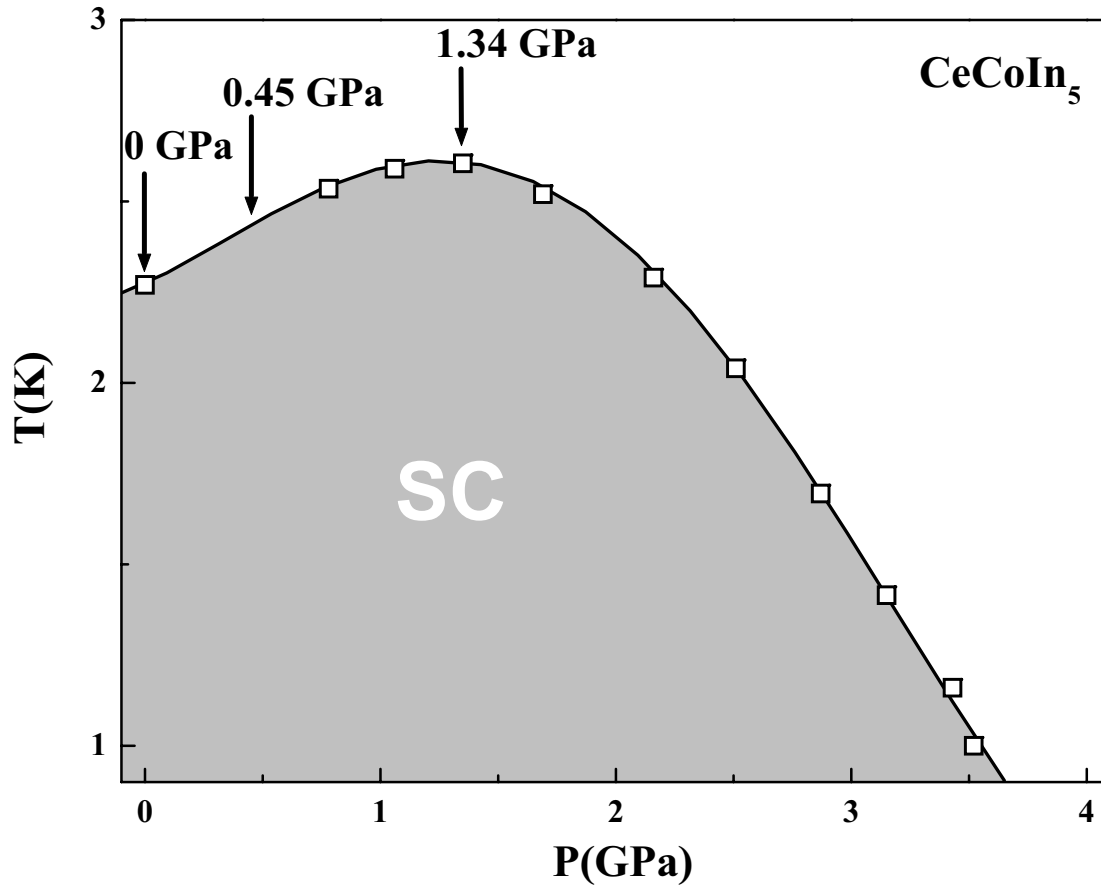
Figure 3.12: $T_c(p)$ phase diagram obtained from resistivity measurements [119]. The specific heat studies were carried out at the pressures depicted by arrows.

an increased scattering in the low temperature specific heat. In order to avoid any artifacts in the data, every measurement in the dilution refrigerator was performed at least twice for each magnetic field. Temperatures down to $T = 0.35$ K and fields up to $B = 14$ T where achievable in a PPMS (Quantum Design) system and a relaxation method was used to measure the specific heat in this case. The shape of the pressure cell allows a precise orientation of the c-axis and the (a, b)-plane of the crystals relative to the magnetic field direction.

Our study was mainly focused on the evolution of the presumed FFLO anomaly with pressure and in addition, we investigated carefully if the theoretical prerequisites for the formation of the FFLO state are still satisfied under pressure. The measurements were conducted at $p = 0$ GPa, $p = 0.45$ GPa and $p = 1.34$ GPa, pressures depicted by arrows in the $T_c(p)$ phase diagram (Fig. 3.12) obtained from resistivity
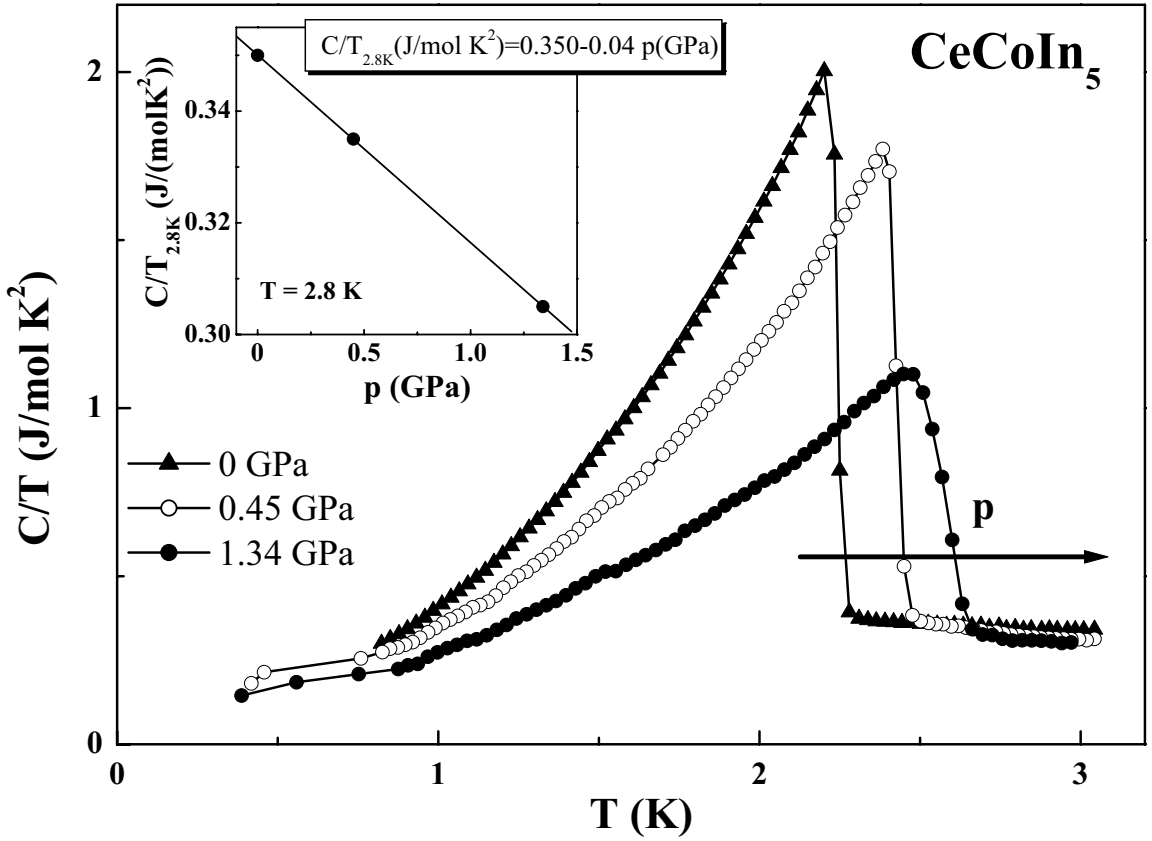
Figure 3.13: $C/T(T)$ dependence at different pressures. Inset: C/T above T_c is linearly decreasing with increasing p.

measurements [119]. The highest pressure was chosen in such a way that it is situated right at the maximum of $T_c(p)$, where the system starts to recover FL behavior and the strong antiferromagnetic quantum critical fluctuations present at ambient pressure are already drastically reduced. To study the evolution of the $B-T$ phase diagram also measurements at intermediate pressure $p = 0.45$ GPa were carried out.

The zero field heat capacity data at each measured pressure are presented in Fig. 3.13. The lattice contribution to the specific heat is negligible in this temperature range for CeCoIn$_5$. At ambient pressure, we find a superconducting transition temperature, defined at the 50% value of the specific heat jump, of $T_c = 2.24$ K, consistent with the literature [1]. In the normal state, just above the superconducting transition temperature, C/T has a large value, typical for strongly correlated electron systems: $\gamma = C/T(T = 2.5 \text{ K}) = 0.360$ J/(mol K^2). This value is slightly higher

than $\gamma = C/T(T = 2.5 \text{ K}) = 0.290 \text{ J/(mol K}^2)$ reported in [1], but in excellent agreement with [120, 123]. This difference in C/T probably can be accounted for by some sample dependency between the earlier prepared single crystals and the most recent ones. While the superconducting state sets in, C/T is still increasing upon decreasing temperature, which might be a manifestation of the probable incomplete condensation of the Kondo centers into the heavy-fermion ground state [77]. A linear fit of the $C(T)/T$ data for 2.4 K$< T < 3.1$ K yields:

$$C/T = 0.464 \text{ (J/(mol K}^2)) - 0.043 \text{ (J/(mol K}^3)) \cdot T. \tag{3.3}$$

At ambient pressure, a remarkably high jump in the specific heat is observed at T_c, which could be explained in part by the not completely formed heavy-fermion state at T_c and in part by strong correlations:

$$\frac{\Delta C}{\gamma T_c} = 4.64, \tag{3.4}$$

where $\Delta C = C_{SC \, state}|_{T_c} - C_{nomal \, state}|_{T_c}$.

Under pressure the temperature dependence of C/T remains similar to the one observed at ambient pressure. However, the considerable reduction of the specific heat jump and of the C/T value just above the superconducting transition, point to a reduction in the correlation strength and implicit of the effective mass m^* with increasing p. Intriguingly enough, this occurs while T_c is enhanced upon pressurizing the sample at an initial rate of:

$$\left.\frac{\partial T_c}{\partial p}\right|_{p=0 \text{ GPa}} \approx (0.405 \pm 0.030) \text{ K/GPa}. \tag{3.5}$$

The simultaneous increase of T_c with the reduction of the quasiparticle interaction might be induced by an enhancement of the chemical potential as suggested by a d-wave density wave (dDW) based theory of superconductivity [125]. Neglecting the strong coupling effects, the jump in the specific heat normalized to the effective mass and T_c must fulfill:

$$\frac{\Delta C}{T_c m^*} \approx \text{const.} \tag{3.6}$$

Table 3.3: The pressure evolution of T_c, ΔC, C/T, effective mass m^* and transition width ΔT.

p (GPa)	0	0.45	1.34
T_c (K)	2.242 ± 0.005	2.428 ± 0.005	2.584 ± 0.010
$\Delta C = (C_s - C_n)\vert_{T_c}$ (J/mol K)	3.743	3.325	1.872
$C/T\vert_{2.8\ \mathrm{K}}$ (J/mol K^2)	0.350	0.335	0.305
$m^*(p)/m^*(0)$	1	0.83	0.43
ΔT (K)	0.020 ± 0.005	0.042 ± 0.005	0.110 ± 0.010

The "weakness" of the coupling would be justified if one assumes an incomplete condensation of the Kondo centers into a coherent heavy-fermion state and as well by the temperature dependence of the upper critical field. The latter can be expressed in a weak coupling model with strong Pauli-limiting effect and d-wave pairing [46]. Therefore, using the equation 3.6, we can roughly estimate a reduction of the effective mass at $p = 0.45$ GPa down to 83% of its ambient pressure value and down to approximately 43% at $p = 1.34$ GPa, in reasonable good agreement with [124].

Despite the good hydrostatic conditions attained in the pressure cell, a slight increase in the transition width is observed as also seen in [120, 123, 124] . This is a reflection of the significant anisotropy in the physical properties of CeCoIn$_5$. A steady increase in the c/a ratio upon applying pressure up to $p \approx 2.5$ GPa is revealed by X-ray diffraction measurements [126]. Indeed, the low temperature physics in this compound seems to be dominated by the in-plane $p - f$ hybridization between Ce and In(1) ions. This is supported also by the increase of hybridization V_{pf} across the CeTIn$_5$ series in the order Rh→Ir→Co [126]. For CeRhIn$_5$, SC sets in only under pressure as V_{pf} increases, while in CeIrIn$_5$ at ambient pressure $T_c = 0.4$ K is well below $T_c = 2.24$ K for CeCoIn$_5$. For small V_{pf} magnetic order is favored but this is replaced by superconductivity as V_{pf} is enhanced as schematically shown in Fig. 3.14.

The importance of the Ce-In hybridization is suggested also by thermal expansion measurements which find an increase in T_c upon reducing the a lattice
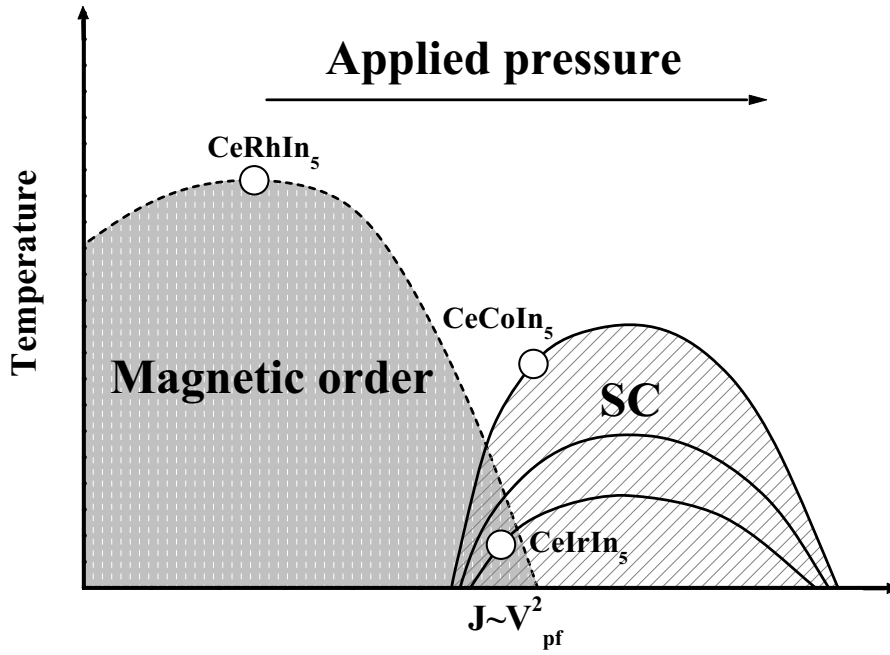
Figure 3.14: Schematic phase diagram for $CeTIn_5$ showing the competition of magnetism and superconductivity as function of the hybridization V_{pf}, according to Ref. [126]. The SC line for $CeRhIn_5$ lies between $CeIrIn_5$ and $CeCoIn_5$.

constant, four times faster than upon reducing c [104]:

$$\frac{\partial T_c}{\partial p_a}\bigg|_{p_a=0 \text{ GPa}} = (0.290 \pm 0.030) \text{ K/GPa}, \qquad (3.7)$$

$$\frac{\partial T_c}{\partial p_c}\bigg|_{p_c=0 \text{ GPa}} = (0.075 \pm 0.010) \text{ K/GPa}, \qquad (3.8)$$

where p_a and p_c are the uniaxial pressures along a and c, respectively. The different rates at which T_c is enhanced when uniaxial stress is applied along the a or c direction is probably the main cause for the increase in the superconducting transition width upon applying hydrostatic pressure.

AC-specific heat measurements under uniaxial stress along the crystallographic a-axis, performed as part of this thesis (experiment briefly described in the appendix), reveal an increase of T_c in the low pressure regime in good agreement with the thermal expansion measurements:

$$\frac{\partial T_c}{\partial p_a}\bigg|_{p_a=0 \text{ GPa}} = (0.305 \pm 0.010) \text{ K/GPa}. \qquad (3.9)$$

The superconducting transition is gradually moved to higher temperature as p_a increases and T_c seems to approach a broad maximum around the highest pressure achieved $p_a = 0.7$ GPa. ΔC is decreasing drastically under small uniaxial stress similar with the behavior under hydrostatic pressure. ΔC tends to saturate above $p_a \geq 0.3$ GPa.

3.3.3 Magnetic field effect on the SC transition for $B \parallel (a, b)$

At ambient pressure the specific heat measurements were only conducted with the magnetic field applied in the (a, b)-plane. At low magnetic fields the SC specific heat anomaly exhibits a mean-field-like shape, characteristic for a second-order phase transition. With increasing B, the anomaly moves to lower temperatures and at high magnetic fields sharpens up and becomes more symmetrical, indicating the change from a second- to a first-order phase transition (Fig. 3.15, upper panel). This is even more convincing if one bears in mind that in the $B(T)$ phase diagram the superconducting phase transition is crossed at glancing angle in high fields which would actually lead to a broadening of the specific heat anomaly.

Additionally, the height of the anomaly C_{peak} shows a minimum (Fig. 3.16) indicating also the crossover from second- to first-order. We used this minimum to define the crossover temperature T_0 ($T_0 = T_c$ at minimum C_{peak}) and the corresponding crossover magnetic field B_0. We find $T_0 = (0.875 \pm 0.050)$ K and $B_0 = (10.5 \pm 0.1)$ T. This yields $T_0 = 0.39\, T_c$ smaller than the upper theoretical threshold of $0.55\, T_c$ found in the purely paramagnetic limit [16]. The first-order character of the phase transition at high magnetic fields is also established by the hysteretic behavior in specific heat measurements [3] and magnetization data [102].

Above $B \geq 11.55$ T no signature of the superconducting phase transition is observed anymore, down to the lowest temperature achievable with our setup $T = 0.1$ K. We estimate an upper critical field of $B_{c2}(0) = 11.6$ T by extending our $B_{c2}(T)$ phase diagram to $T = 0$ K and assuming $B_{c2} \propto (1 - (T/T_c)^2)$. As it will be shown later in a detailed analysis of the $B_{c2}(T)$, our estimates for the upper critical field are in good agreement with the theoretical calculations.
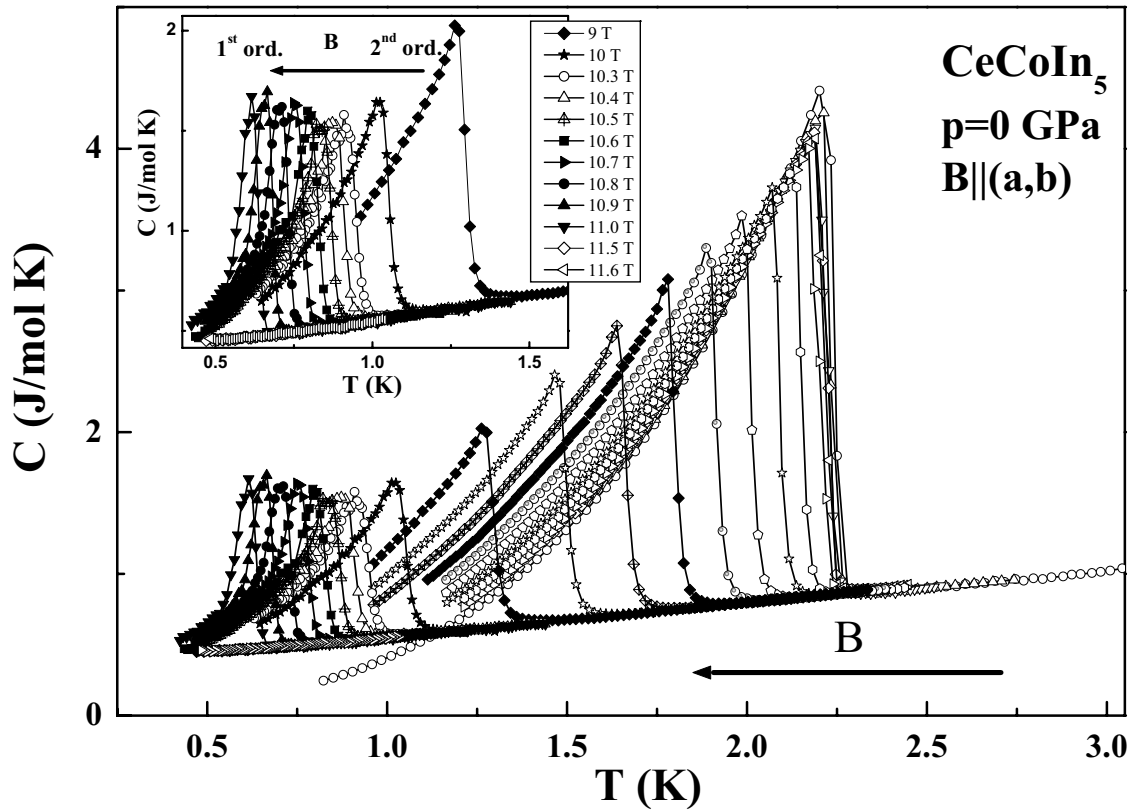
Figure 3.15: The ambient pressure evolution of the SC transition with the magnetic field applied in the basal plane for fields up to 11.6 T. Inset: Above 10.5 T the transition sharpens up and becomes more symmetric indicating a crossover to a first-order phase transition.

The ambient pressure findings for $B \parallel (a,b)$ are in good agreement with the results of A. Bianchi *et al.* [3]. They find $T_0 \approx 1$ K for B in the plane and $T_0 = 0.7$ for $B\|c$. The small difference in T_0 can be explained by the different way of defining the crossover temperature which in reference [3, 101] was determined using the magnetocaloric effect. However, C_{peak} in the specific heat data published in the latter mentioned reference, corresponds to a T_0 and B_0 in excellent agreement with our findings. Our attempts to follow the first-order phase transition using the magnetocaloric effect, with the sample inside the pressure cell, and employing the same method as described in [101] did not provide a precise enough tool to define T_0.

The main goal of the low temperature measurements performed in the dilution refrigerator was to identify the low-T anomaly previously ascribed to a transition into
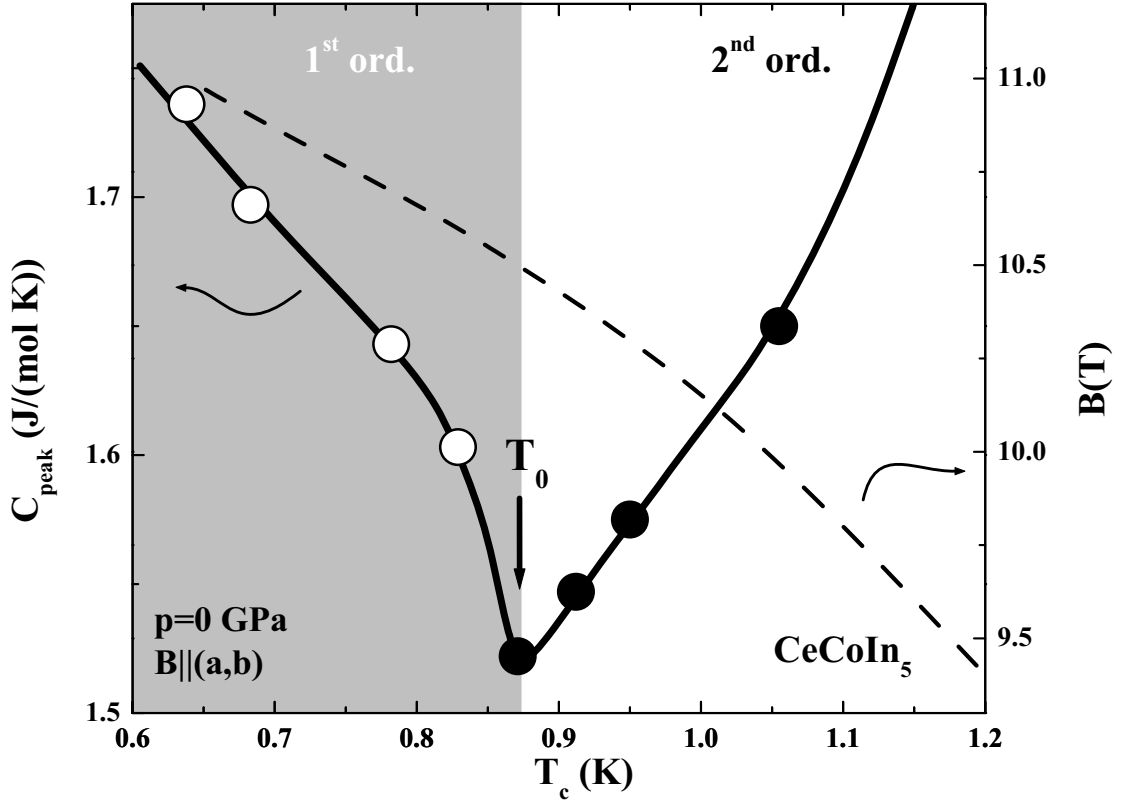
Figure 3.16: $C_{peak}(T_c)$ dependency at ambient pressure and in high magnetic fields. $C_{peak}(T_c)$ has a minimum at $T_0 = (0.875 \pm 0.050)$ K which corresponds to $B_0 = 10.5$ T on the right axis. We take T_0 as the crossover temperature from the second to first-order phase transition. For $B > B_0$ the SC transition is first-order (shaded area). $B_{c2}(T)$ is depicted by the dashed line.

a FFLO state [3].

The total heat capacity of the loaded cell (no addenda subtracted) is presented in Fig. 3.17 for different magnetic fields. We chose to plot $CT^3(T)$ in order to compensate for the T^{-2} dependence of the nuclear term which dominates the low-T heat capacity. The upper two curves in Fig. 3.17 are shifted for convenience by 0.07 μJK^2 and 0.14 μJK^2, respectively. Our measurement reveals, above $B = 10.4$ T, a tiny but clear anomaly which can be traced with changing B. This is consistently reproduced in successive runs at the same field. The size of the anomaly is around $3\% - 4\%$ of the total heat capacity. For the sake of clarity we denote this anomaly T_{FFLO} though the verification of its true nature is the aim of this specific heat study under pressure. We define T_{FFLO} as the temperature corresponding to the top of the transition as it
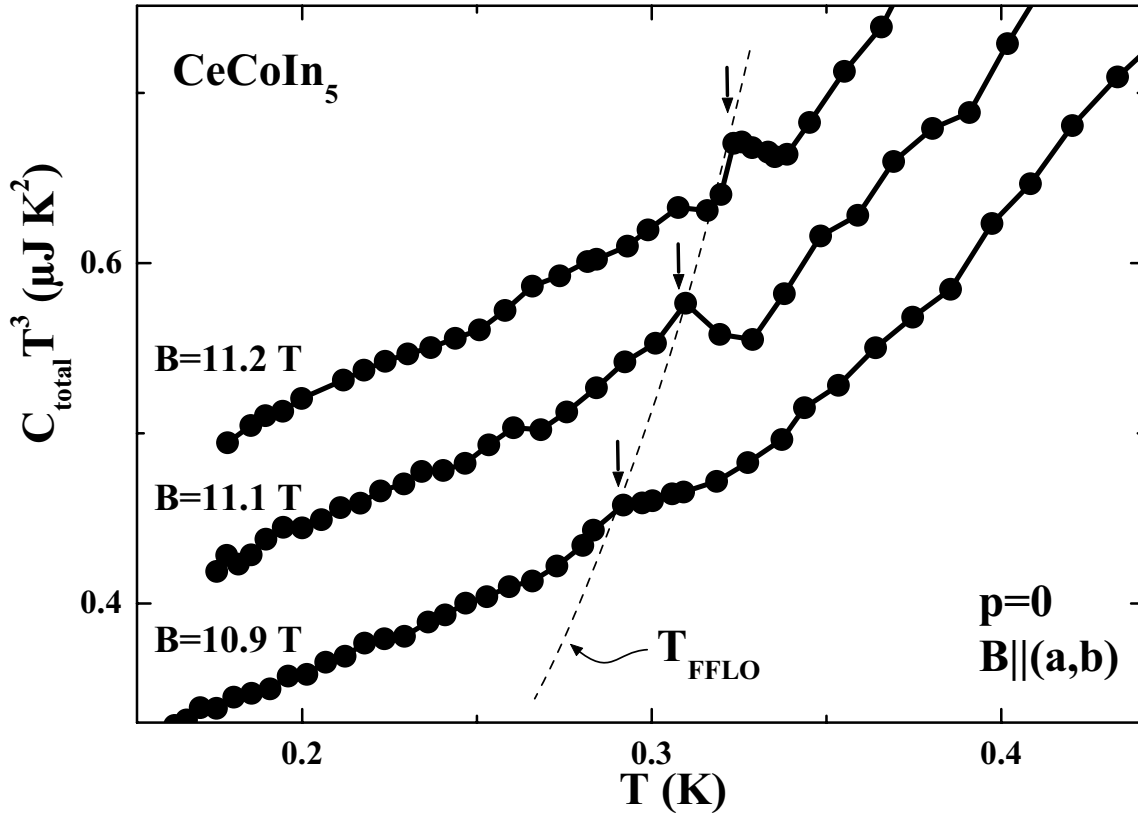
Figure 3.17: The heat capacity of the loaded pressure cell multiplied with T^3 as function of T for $B = 10.9$ T, 11.1 T and 11.2 T. The upper two curves are shifted, for convenience, by 0.07 μJK^2 and 0.14 μJK^2 respectively. The T_{FFLO} anomaly, depicted by arrows in figure, is identified unambiguously.

is depicted by arrows in Fig. 3.17.

T_{FFLO} has a weak B dependence: upon increasing the magnetic field, T_{FFLO} is enhanced monotonically while T_c is gradually moved to lower temperatures. Close to the upper critical field B_{c2}, T_{FFLO} is almost field independent. As T_{FFLO} and T_c approach each other upon rising the field, it becomes increasingly difficult to deconvolute the two anomalies as most of the entropy comes from the high-T superconducting phase. We find a $T_{FFLO}(B)$ dependency in excellent agreement with [3].

Qualitatively similar result to the ambient pressure findings are obtained for $p = 0.45$ GPa. The superconducting transition is gradually suppressed upon increasing the magnetic field and finally driven, close to $B_{c2}(0)$, from second- to first-order. A change of symmetry and a sharpening of the superconducting transition is clearly visible in the specific heat data obtained after subtracting the addenda (Fig. 3.18).

Figure 3.18: The evolution of the SC transition upon applying high magnetic field in the basal plane, at $p = 0.45$ GPa. With increasing B the transition sharpens up and becomes more symmetrical indicating a crossover to a first-order phase transition.

The resolution of the specific heat measurement at this pressure, remains very high even at such elevated magnetic fields due to the remarkably good filling factor of this pressure cell.

The height of the anomaly C_{peak} shows a distinct minimum (Fig. 3.19) while the phase transition changes to first-order at $T_0 = (1.025 \pm 0.050)$ K $= 0.42\,T_c$. T_0 corresponds to a crossover field $B_0 = 11.2$ T. Both T_0 and B_0 are higher compared with the ambient pressure values. The pressure stabilizes the superconductivity against B for $B \parallel (a,b)$ as the upper critical field is enhanced as well to $B_{c2}(0) = 12.5$ T. This trend continues up to the maximum pressure of our experiment ($p = 1.34$ GPa) where, despite the reduction of the quasiparticle interaction, T_c is enhanced together with the upper critical field which reaches $B_{c2}(0) = 14.3$ T.

A change in the symmetry of the superconducting transition can still be ob-

Figure 3.19: $C_{peak}(T_C)$ dependency at $p = 0.45$ GPa and in high magnetic field. $C_{peak}(T_C)$ has a pronounced minimum at $T_0 = 1.025 \pm 0.050$ K which corresponds to $B_0 = 11.2$ T on the right axis. For $B > B_0$ the SC transition is first-order (shaded area). $B_{c2}(T)$ is depicted by the dashed line.

served close to $B_{c2}(0)$ (Fig. 3.20). However, as the superconducting jump ΔC has been already substantially reduced by pressure at zero field and as the measurement has to be carried out at higher B, only a shallow minimum can be observed if we plot the height of the SC transition C_{peak} as function of T_c (Fig. 3.21). We obtain a crossover temperature $T_0 = 1.17 \pm 0.10$ K $= 0.44\, T_c$ and the corresponding magnetic field $B_0 = 12.4$ T. The first-order character of the phase transition is confirmed as well by magnetization measurements under pressure which display a clear thermal hysteresis and a step like feature in $M(B)$ [127]. This magnetization study yields a $T_0 \approx 1.1$ K at $p = 1.34$ GPa, in excellent agreement with our results.

A very important result of our study is the fact that we are able to follow the pressure evolution of T_{FFLO}. Indeed, a small anomaly in the electronic contribution to the low temperature specific heat $C - C_{Schottky}$ (depicted in Fig. 3.22 for
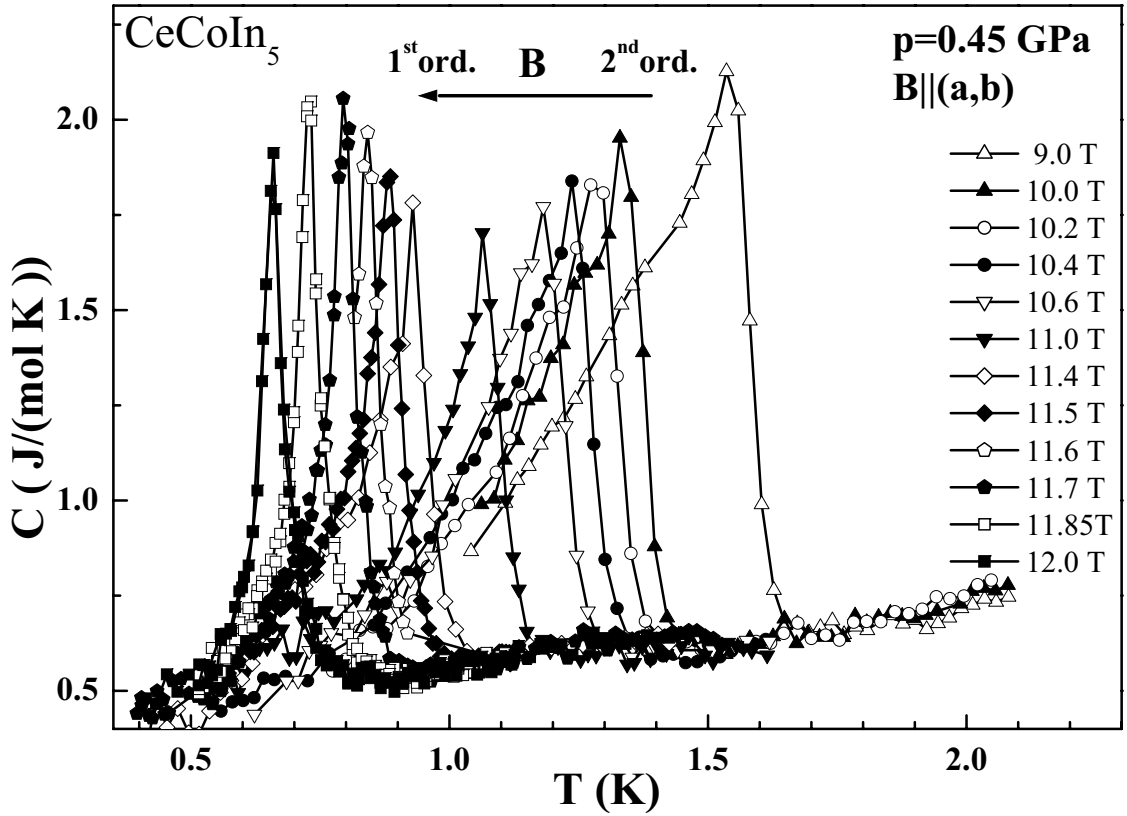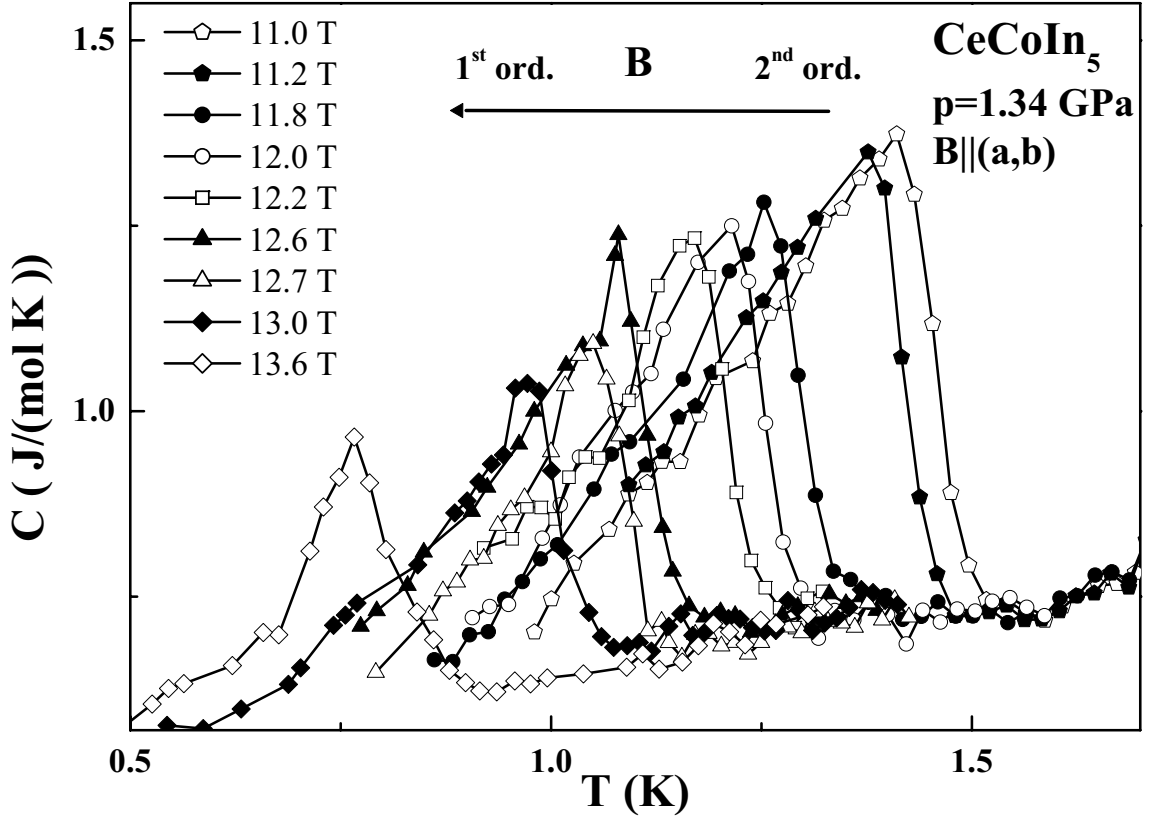
Figure 3.20: The evolution of the SC transition upon applying high magnetic field in the basal plane at $p = 1.34$ GPa. Above 11.2 T the transition sharpens up and becomes more symmetrical indicating a crossover to a first-order phase transition.

selected fields), is resolved unambiguously in the low-T range for both, $p = 0.45$ GPa (Fig. 3.22, upper panel) and $p = 1.34$ GPa (Fig. 3.22, lower panel). This feature is confirmed by at least two successive runs at each magnetic field. Similar to the ambient pressure findings, the anomaly is easily visible even in the raw data (not shown here) before subtracting the addenda. In order to determine the Schottky contribution of In we assumed that for very low temperatures

$$C \approx \gamma T + \frac{\alpha_N}{T^2} \, , \tag{3.10}$$

where the second term is the nuclear contribution to the specific heat. After subtracting the pressure cell contribution, the zero temperature intercept of a $CT^2(T^3)$ plot yields the α_N values. The size of the anomaly is comparable with the one found at ambient pressure, in fair agreement with [3]. Under finite pressure, with our ex-
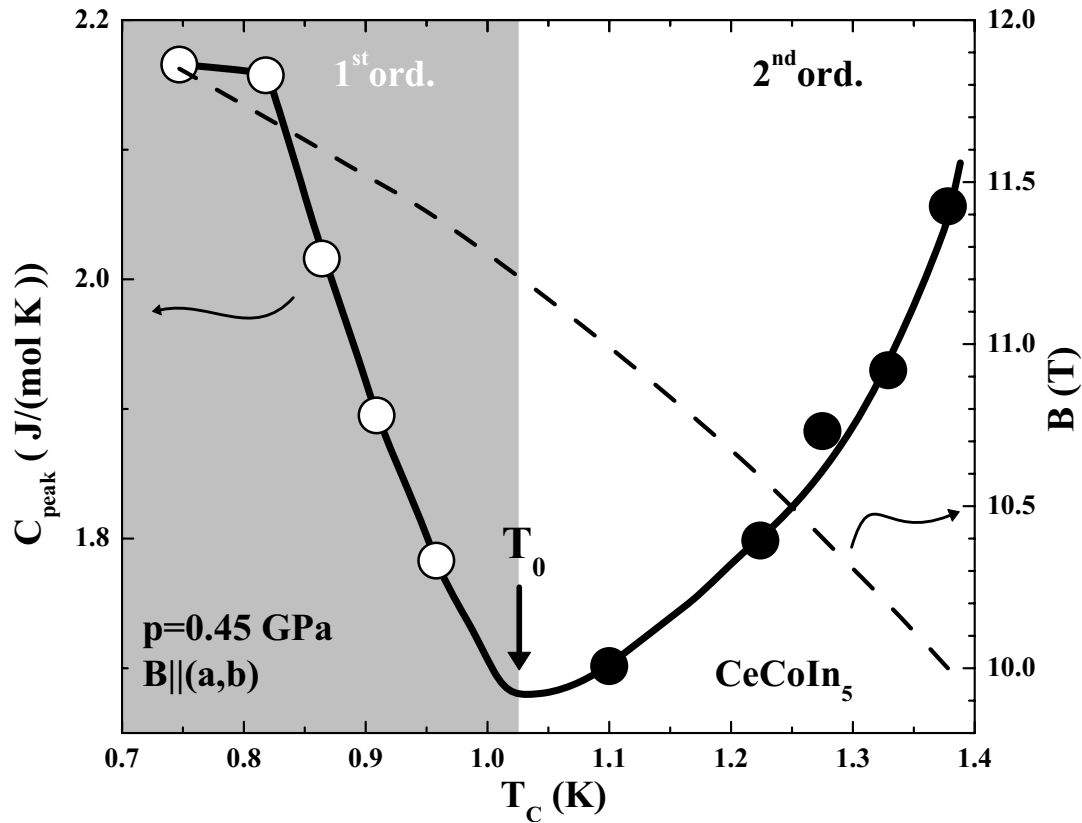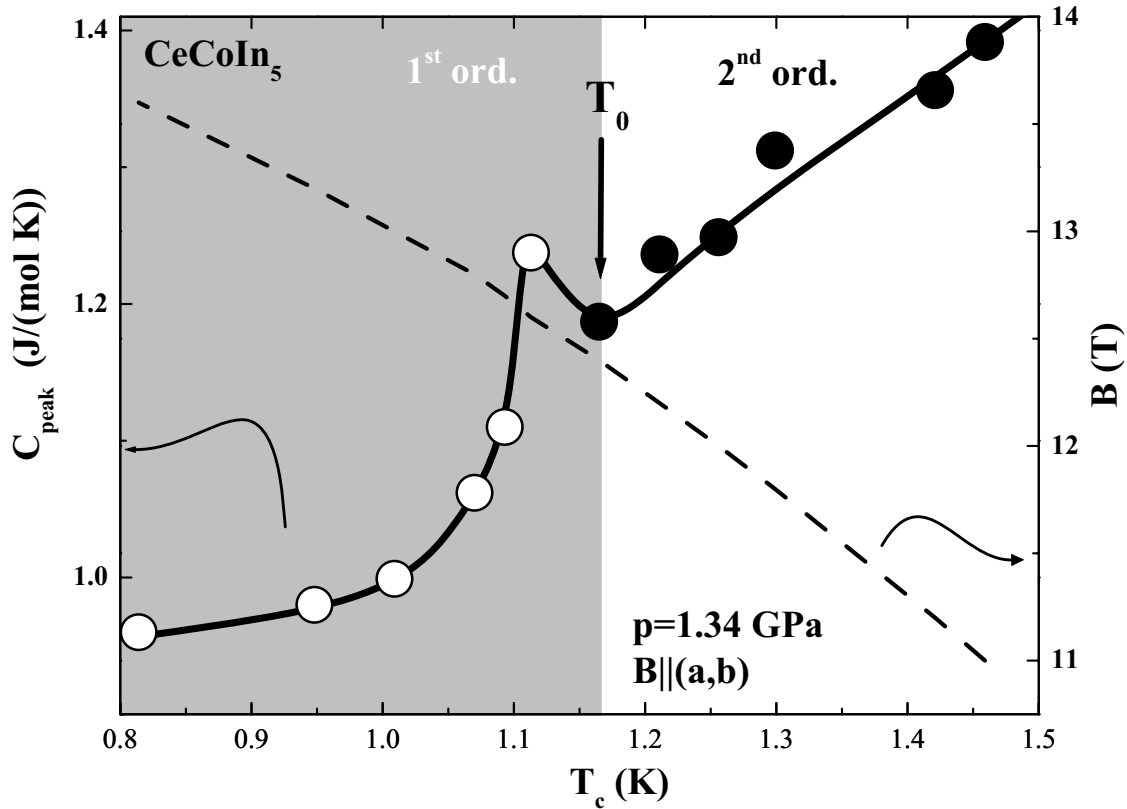
Figure 3.21: $C_{peak}(T_c)$ dependency at $p = 1.34$ GPa and in high magnetic field. $C_{peak}(T_c)$ has a shallow minimum at $T_0 = (1.17 \pm 0.10)$ K which corresponds to $B_0 = 12.4$ T on the right axis. For $B > B_0$ the SC transition is first-order (shaded area). $B_{c2}(T)$ is depicted by the dashed line.

perimental setup, we are not able to follow $T_{FFLO}(H)$ all the way to the tricritical point in the phase diagram, because at lowest temperatures our maximum magnetic field is limited to $B = 12$ T.

For $p = 0.45$ GPa, at $B = 10.4$ T the transition from the normal to the superconducting state is still of second-order, but a second anomaly is already observable at low temperatures. Only for fields higher than 11.2 T (11.5 T and 12 T depicted in Fig. 3.22) the superconducting phase transition is of first-order. This behavior is different from results at ambient pressure: for $p = 0$ GPa, at the field where the second anomaly is initially found, the transition from the normal to the SC state is already of first-order. We obtain similar results for $p = 1.34$ GPa, where, at fixed field, a normal to superconducting state phase transition, of second-order, is followed, upon lowering T, by a second anomaly in $C(T)$.
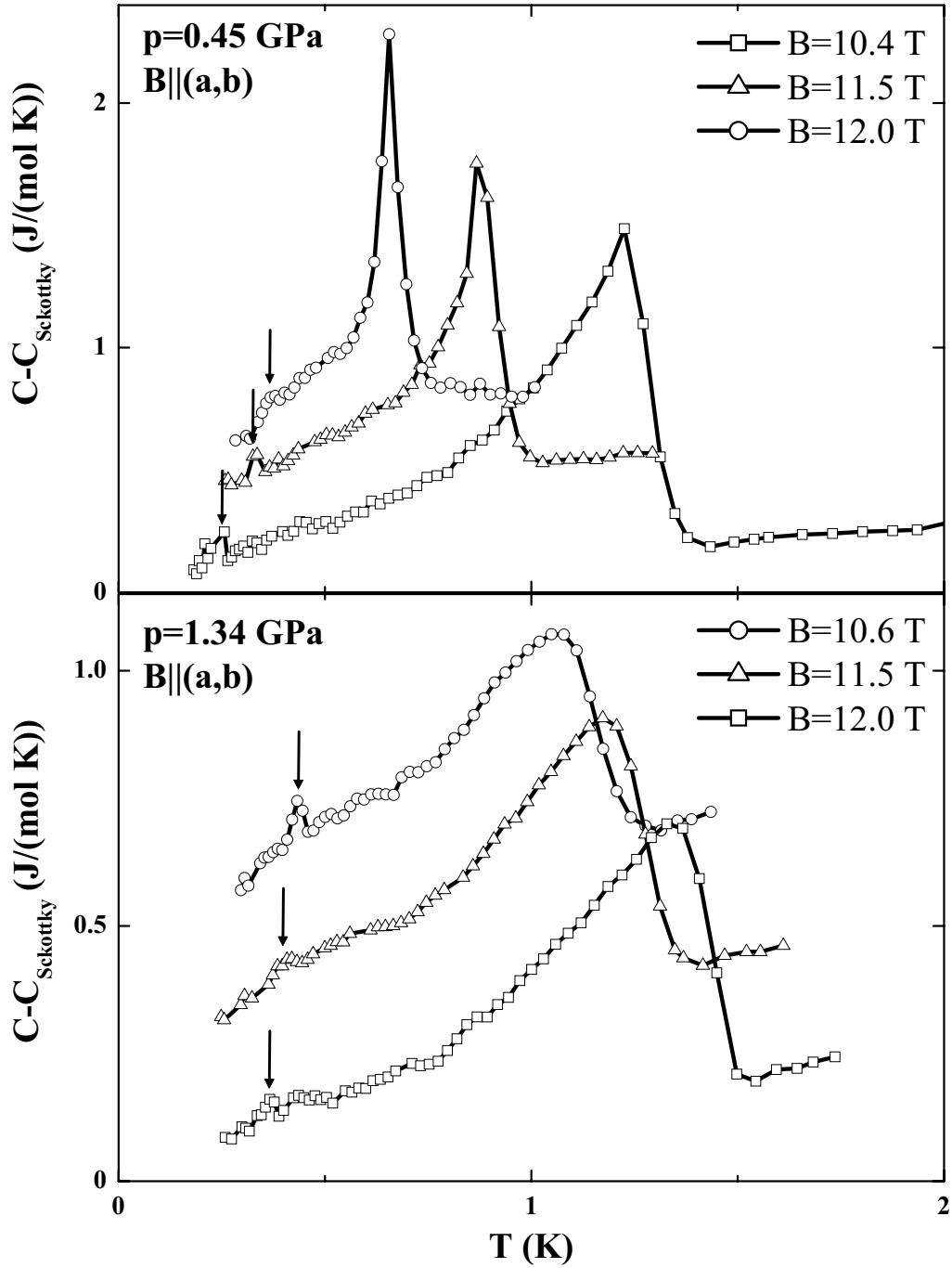
Figure 3.22: Electronic contribution to the low temperature specific heat $C-C_{Schottky}$ for selected magnetic fields B close to $B_{c2}(0)$ at $p = 0.45$ GPa (upper panel) and $p = 1.34$ GPa (lower panel). Data at 11.5 T ($\triangle$) and 12 T ($\circ$) are shifted by 0.25 J/(mol K) and 0.5 J/(mol K), respectively. The arrows indicate the T_{FFLO} anomaly.

3.3.4 Magnetic field effect on the SC transition for $B \parallel c$

Specific heat measurements under pressure were carried out also for the magnetic field perpendicular to the basal plane (i.e., $B \parallel c$). A change in symmetry of the SC
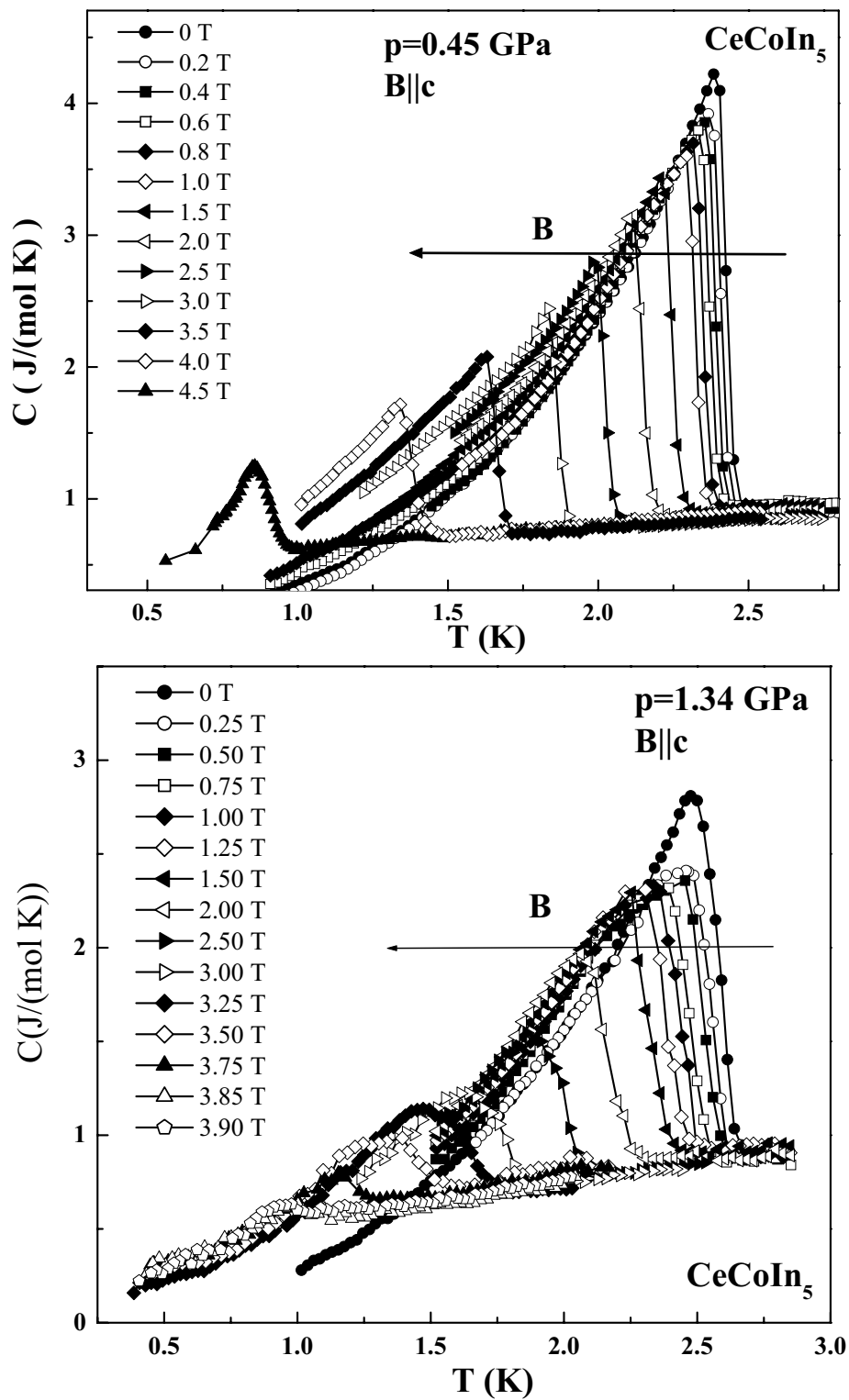
Figure 3.23: $C(T)$ dependence for different magnetic fields applied along the c-axis at $p = 0.45$ GPa (upper panel) and $p = 1.34$ GPa (lower panel).

anomaly is observed close to the upper critical field for $p = 0.45$ GPa (Fig. 3.23, upper panel). At $B = 4.5$ T the transition appears to be first-order, however we can not determine T_0 precisely from our data. In contrast, no obvious change of the phase transition character is observed at $p = 1.34$ GPa probably due to the drastic reduction of the superconducting jump (Fig. 3.23, lower panel). Magnetization experiments, however, reveal similar T_0 values for both field orientations [127].

Already at ambient pressure a significant anisotropy has been observed for the upper critical field. This is not surprising given the quasi-cylindrical Fermi-surface structure which would allow a more pronounced orbital-limiting effect in the $B \parallel c$ case. At each pressure, as it will be shown later, the orbital-limiting effect is roughly by a factor of three stronger for $B \parallel c$ compared to the $B \parallel (a, b)$ case. Interestingly, while the pressure stabilizes the superconducting state against the in-plane magnetic field, it has just the opposite effect for $B \parallel c$. In the latter case the upper critical field is reduced upon applying pressure from $B_{c2}(0) = 4.9$ T at ambient pressure [101] to $B_{c2}(0) = 4.7$ T at $p = 0.45$ GPa and lower to $B_{c2}(0) = 4.2$ T at $p = 1.34$ GPa. For this field orientation we do not pursue any possible FFLO anomaly at low temperature. Though, at ambient pressure an anomaly in specific heat was detected [3], for this field orientation the FFLO state is less stable as T_{FFLO} is less than half its value for $B \parallel (a, b)$ (i.e., $T_{FFLO} \approx 0.130$ K). Moreover, the existence of the low-T anomaly for $B \parallel c$ has not yet been confirmed, to our knowledge, in subsequent studies at ambient pressure.

3.3.5   Discussion and conclusions

The superconducting transition temperature T_c determined from our specific heat data rises with increasing p, in excellent agreement with previous pressure studies [111, 119, 120]. The electronic specific heat coefficient γ decreases linearly with increasing p and the drastic reduction of the superconducting jump indicates a substantial drop of the effective mass above $p = 0.45$ GPa, a tendency confirmed also by dHvA studies [121]. At $p = 1.34$ GPa the electronic effective mass drops below 50% of its ambient pressure value, in reasonably good agreement with [124].

At ambient pressure we have established a $B - T$ phase diagram for CeCoIn$_5$ as was previously observed [3, 4]. Figure 3.24 displays the combined $B - T$ phase diagram for $p = 0$, 0.45, and 1.34 GPa for $B \parallel (a, b)$ and for $B \parallel c$. First we note the increasing anisotropy between $B_{c2}(0)_{B\parallel(a,b)}$ and $B_{c2}(0)_{B\parallel c}$; in the first case the upper critical field $B_{c2}(0)$ is enhanced and in the latter suppressed upon increasing pressure. Remarkably, for $B \parallel c$ the upper critical field is suppressed by pressure while T_c is enhanced, behavior which remains a challenge to understand.

As the main goal of our study is to probe the possible realization of the FFLO state in CeCoIn$_5$, we discuss in the following the evolution of the $B - T$ phase diagram with pressure and show that the necessary prerequisites for the FFLO state formation are still satisfied as the system is driven away from the influence of the quantum critical point.

Foremost, we were able to track the low-T anomaly up to the highest applied pressure for $B \parallel (a, b)$. The anomaly at T_{FFLO} appears first at almost the same magnetic field, $B \approx 10.5$ T, independent of pressure. With further increasing the field, $T_{FFLO}(B)$ moves gradually to higher temperatures for all pressures. The $T_{FFLO}(B)$ line remains almost unaffected as the applied pressure is increased to $p = 0.45$ GPa despite the enhancement of T_c, T_0 and $B_{c2}(0)$. As can be seen in Fig. 3.24, the $T_{FFLO}(B)$ lines overlap almost perfectly for $p = 0$ GPa and $p = 0.45$ GPa. However, a further increase up to $p = 1.34$ GPa moves $T_{FFLO}(B)$ to significantly higher temperatures and $B_{c2}(0)$ increases considerably too.

Interestingly, like $T_{FFLO}(B)$ at $p = 0$ GPa and $p = 0.45$ GPa, the initial slope of the upper critical field $B'_{c2} = \frac{\partial B_{c2}}{\partial T}\big|_{T=T_c}$ remains roughly the same. For the initial slope of the upper critical field B'_{c2} we obtain for $B \parallel (a, b)$: $B'_{c2}(0 \text{ GPa}) = -30.5$ T/K, and $B'_{c2}(0.45 \text{ GPa}) = -29.4$ T/K.

Correspondingly, the orbital critical field

$$B_{orb} = h_0^* T_c \left| \left(\frac{\partial B_{c2}}{\partial T} \right)_{T=T_c} \right| \tag{3.11}$$

does not change significantly. The value of h_0^* depends on the ratio of the mean-free path ℓ_{tr} and the superconducting coherence length ξ_0; h_0^* ranges from 0.69 in
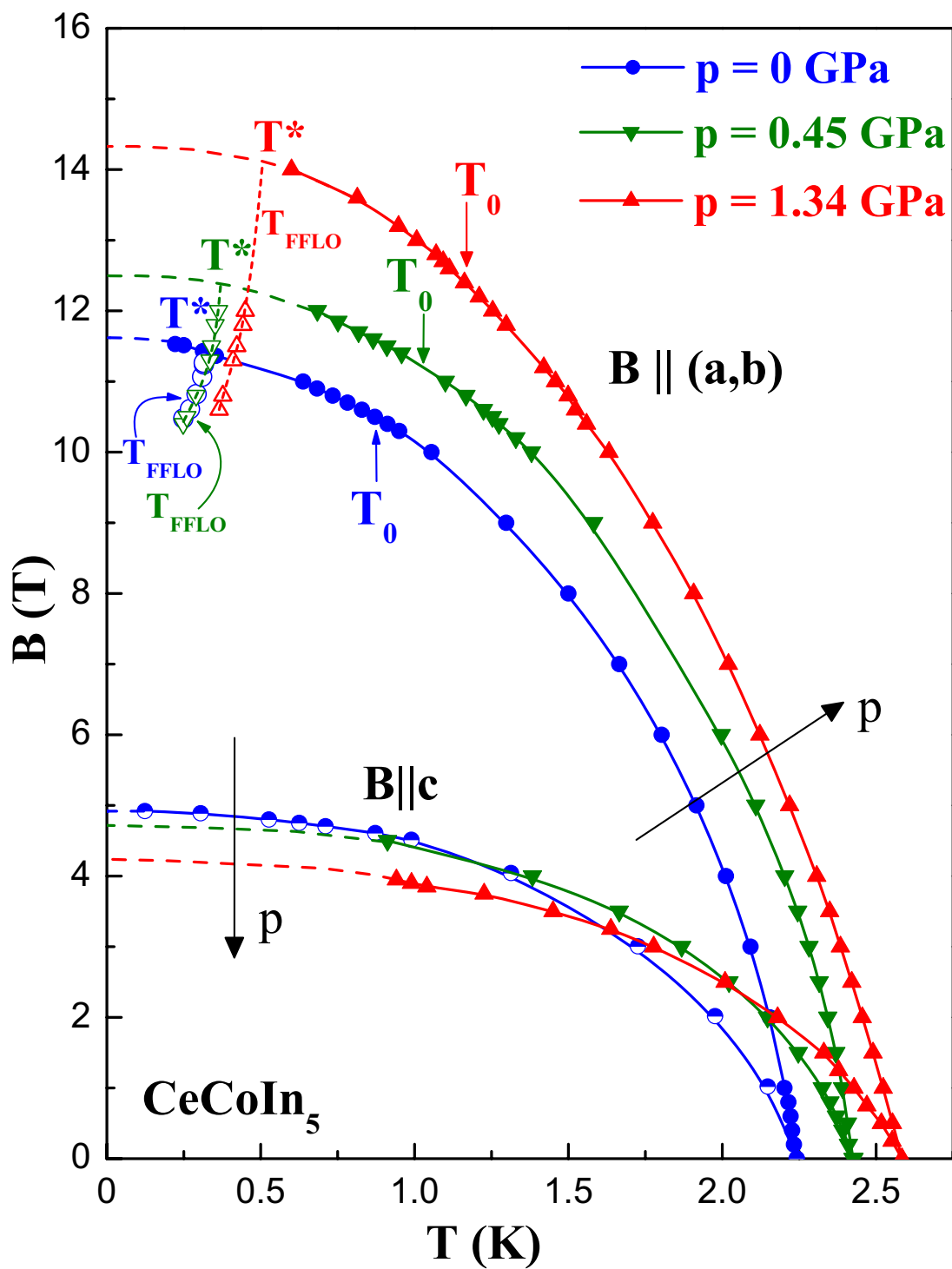
Figure 3.24: $B - T$ phase diagram for $B \parallel (a,b)$ and $B \parallel c$. Arrows mark the crossover temperature T_0 from a second- to a first-order SC phase transition and T^* the tricritical point. Data for $p = 0$ and $B \parallel c$, shown by half-filled symbols, are taken from [101].

the dirty-limit ($\ell_{tr}/\xi_0 \ll 1$) to 0.73 in the clean-limit case ($\ell_{tr}/\xi_0 \gg 1$) [128], this last condition being satisfied in CeCoIn$_5$ also under pressure as we will discuss later. Therefore we obtain:

$$B_{orb}(0 \text{ GPa}) = 47.9 \text{ T and } B_{orb}(0.45 \text{ GPa}) = 49.9 \text{ T}.$$

However, at $p = 1.34$ GPa, $|B'_{c2}|$ decreases drastically, by roughly 50% to $B'_{c2} = -16.4$ T/K and consequently $B_{orb}(1.34 \text{ GPa}) = 29.7$ T.

A similar behavior is also observed for the field perpendicular to the basal plane ($B \parallel c$), as the initial slope of the upper critical field changes significantly only above $p = 0.45$ GPa: $B'_{c2}(0 \text{ GPa}) = -10.8$ T/K, $B'_{c2}(0.45 \text{ GPa}) = -10.2$ T/K, $B'_{c2}(1.34 \text{ GPa}) = -6.5$ T/K and correspondingly: $B_{orb}(0 \text{ GPa}) = 16.9$ T, $B_{orb}(0.45 \text{ GPa}) = 17.3$ T and $B_{orb}(1.34 \text{ GPa}) = 11.7$ T.

To determine the Maki parameter

$$\alpha = \sqrt{2}\frac{B_{orb}}{B_P} \tag{3.12}$$

we need to estimate the Pauli-limiting field B_P. An accurate estimation of B_P could be obtained considering:

$$B_P = \frac{B_c}{2\sqrt{\pi \chi_{spin}}} \quad [20], \tag{3.13}$$

where χ_{spin} is the magnetic susceptibility due to the electron spin and

$$B_c = T_c\sqrt{2\pi \frac{\gamma_0}{V_{mole}}} \quad [20], \tag{3.14}$$

is the thermodynamical critical field with γ_0 the Sommerfeld coefficient and V_{mole} the molar volume. However, no spin susceptibility or Knight shift data under pressure are available at the moment.

It is reasonable to assume, as a first approximation, $B_P \approx B_{c2}(0)$. With this estimate for B_P we get

$$\alpha(0 \text{ GPa}) = 5.8,$$

$$\alpha(0.45 \text{ GPa}) = 5.7,$$

$$\alpha(1.34 \text{ GPa}) = 2.9.$$

This is still sufficiently large, even at the maximum pressure, compared to the minimum value $\alpha = 1.8$ for s-wave superconductors required to realize the FFLO state [36].

It is as well necessary to verify if the system remains in the clean-limit under pressure. We find that the ratio between the mean-free path and the coherence length, ℓ_{tr}/ξ_0, increases substantially with pressure for both field orientations. To estimate the coherence length ξ_0 we used the BCS relation

$$\xi_0 = \sqrt{\frac{\Phi_0}{2\pi B_{c2}(0)}}, \tag{3.15}$$

where $\Phi_0 = h/(2e) = 2.0678 \, 10^{-15}$ Wb is the flux quantum. There is no straightforward alternative to determine ξ_0 without considering as starting assumption the system either in the clean- or dirty-limit. However, the equation 3.15 gives an upper limit estimation for ξ_0 as it is deduced taking into account the orbital effects. Replacing B_{c2} by B_{orb} in 3.15 would yield significantly smaller values for ξ_0 and, therefore, higher ℓ_{tr}/ξ_0 ratios.

For the mean-free path, ℓ_{tr}, we then followed the scheme of Orlando *et al.* developed for s-wave superconductors [129]:

$$\ell_{tr} = 9 \times 10^{19} \, \hbar (3\pi^2)^{\frac{1}{3}} \frac{1}{e^2 \rho_0 (\Omega \text{cm})(n^{\frac{2}{3}} \frac{S}{S_F})} = 1.27 \times 10^{12} \frac{1}{\rho_0 (\Omega \text{cm})(n^{\frac{2}{3}} \frac{S}{S_F})} \quad (\text{Å}), \tag{3.16}$$

$$\xi_0 = 1.781 \frac{\hbar <v_F>}{\pi^2 k_B T_c} = 1.781 k_B (3\pi^2)^{-\frac{1}{3}} \frac{n^{\frac{2}{3}} \frac{S}{S_F}}{\gamma T_c} = 7.95 \times 10^{-9} \frac{n^{\frac{2}{3}} \frac{S}{S_F}}{\gamma T_c} \quad (\text{Å}), \tag{3.17}$$

where ρ_0 is the low temperature normal state resistivity, S/S_F is the Fermi-surface in units of the Fermi-surface of a free-electron gas density n, $<v_F>$ is the average Fermi velocity and γ is the normal state electronic specific heat coefficient expressed in (erg cm^{-3} K^{-2}). Replacing $n^{2/3}S/S_F$ determined from equation 3.17 into 3.16 we obtain:

$$\ell_{tr} = 1.00965 \times 10^4 \frac{1}{\rho_0 \, \xi_0 \, \gamma \, T_c} \quad (\text{Å}). \tag{3.18}$$

Table 3.4: The mean-free path ℓ_{tr}, coherence length ξ_0 and ℓ_{tr}/ξ_0 at different pressures and field orientations.

$p(GPa)$	0	0.45	1.34
ℓ_{tr} (Å) for $B \parallel (a, b)$	318	451	925
ξ_0 (Å) for $B \parallel (a, b)$	53	51	48
ℓ_{tr}/ξ_0 for $B \parallel (a, b)$	6	9.2	20
ℓ_{tr} (Å) for $B \parallel c$	206	277	502
ξ_0 (Å) for $B \parallel c$	82	84	88
ℓ_{tr}/ξ_0 for $B \parallel c$	2.5	3.2	5.7

Using the measured γ and T_c values (Table 3.3) together with ρ_0 data from [119] and ξ_0 given by equation 3.15 we find the values listed in Table 3.4.

ℓ_{tr}/ξ_0 is enhanced substantially with rising p for both field orientations, indicating that the system becomes even "cleaner" when pressurized. The increase of ℓ_{tr} with increasing pressure is essentially caused by the drop of the normal state resistance reflecting the reduction of the spin-fluctuations [111, 119]. The difference we find for ℓ_{tr}/ξ_0 at ambient pressure compared to [79] is due to the different normal state resistivity values we used for our calculation.

Extrapolating the $T_{FFLO}(B)$ lines to higher fields, unaccessible experimentally with our present setup, we can estimate for the tricritical point T^*: $T^*(0 \text{ GPa}) \approx (0.320 \pm 0.015)$ K $\approx 0.14\, T_c$, $T^*(0.45 \text{ GPa}) \approx (0.37 \pm 0.02)$ K $\approx 0.15\, T_c$ and $T^*(1.34 \text{ GPa}) \approx (0.50 \pm 0.05)$ K $\approx 0.19\, T_c$. This indicates that the FFLO state forms well below the temperature T_0 where the paramagnetic effect starts to dominate the orbital effect in lowering the upper critical field. This is in good agreement with a weak coupling BCS model involving singlet $d_{x^2-y^2}$ pairing, AFM fluctuations and which takes into account both orbital and spin depairing [47]. T^*/T_0 ratios at different pressures are depicted in Table 3.5.
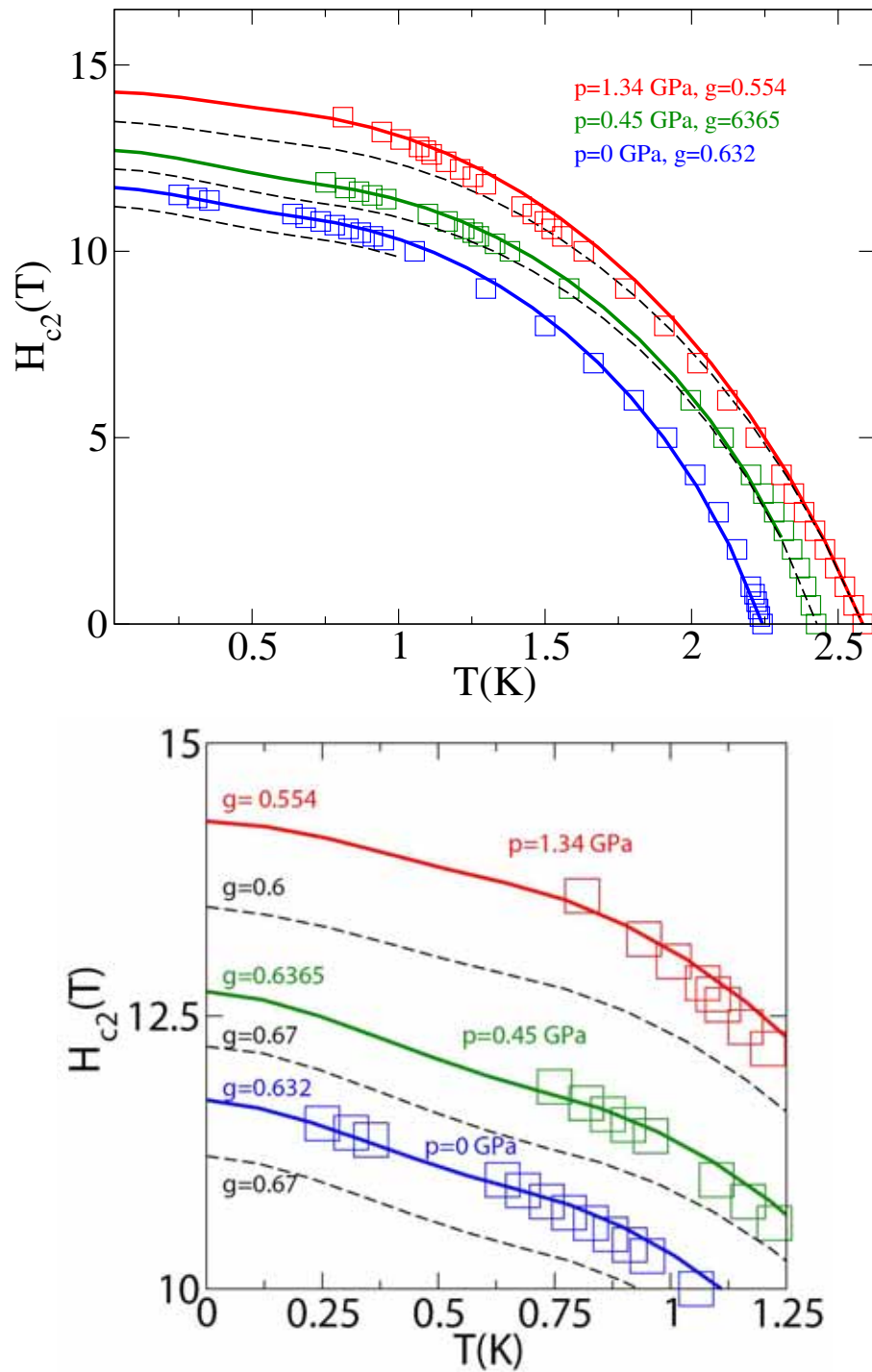
Figure 3.25: Theoretical fits to upper critical field data at different pressures for $B \parallel (a,b)$. Upper panel: the whole T range. Lower panel: low-T range. The dashed lines are generated with different g-factors. See text for details.

The $B_{c2}(T)$ data in Fig. 3.24 for $B \parallel (a, b)$ were analyzed [130] in terms of the theory developed in [45, 46] in which d-wave SC and the Gruenberg-Gunther ansatz [36] are incorporated within a weak-coupling BCS model. The effect of the quasiparticle mean-free path is neglected, which is valid for CeCoIn$_5$ since $\ell_{tr}/\xi_0 \gg 1$. We can describe $B_{c2}(T)$ for both $B \parallel c$ and $B \parallel (a, b)$ (we neglected the small in-plane anisotropy for $B \parallel (a, b)$). The result is summarized in Table 3.5. The Fermi velocities v_a and v_c are deduced from B'_{c2} at $T = T_c$ for $B \parallel c$ and $B \parallel (a, b)$, respectively, while the g-value is obtained from $B_{c2}(T)$ for $B \parallel (a, b)$ and $T < 0.7$ K.

The theoretically estimated values for $B_{c2}(0)$ are in fair agreement with the experimental data. The theoretical $B_{c2}(T)$ curves, plotted in Fig. 3.25, are obtained using T_c, v_a, v_c and g as parameters and found to describe the experimental phase diagram quite well. The relevance of the g-factor at low-T is underscored by the considerable offset induced by only a slight change of the g-value (dashed lines in Fig. 3.25).

At $p = 1.34$ GPa, the high-T data are well described by $g = 0.6$. However, a small decrease of the g-factor to $g = 0.554$ seems to describe the data better for $T < T_0$. The latter value is also used to calculate $B_{c2}(0)$. Such a weak $g(B)$ dependence is not accounted for by the current theory and a different theoretical approach using, e.g. a generalized Fermi liquid theory might be required. The reduction of the g-factor at low temperatures is a consequence of an additional enhancement of the upper critical field at low-T suggesting maybe a stronger effect of the FFLO state on B_{c2} than already included in the theoretical model. This enhancement is easily seen in the phase diagram if we compare the $B_{c2}(T)$ lines: while for $p = 0$ GPa and $p = 0.45$ GPa the $B_{c2}(T)$ are roughly parallel to each other for $p = 1.34$ GPa, B_{c2} increases at a faster pace upon lowering T below T_0. This is underlined in Fig. 3.26 where the upper critical field $B_{c2}(T)$ normalized to $B_{c2}(0)$ is plotted as a function of the reduced temperature T/T_c: the $p = 1.34$ GPa curve starts with a lower slope but finally, as the transition becomes first-order, at $T = T_0 = 0.44\, T_c$, exceeds the values for ambient pressure. This indicates, together with the enhancement of T_0, T^* and $B_{c2}(0)$ that the FFLO state becomes more robust under pressure, despite a smaller
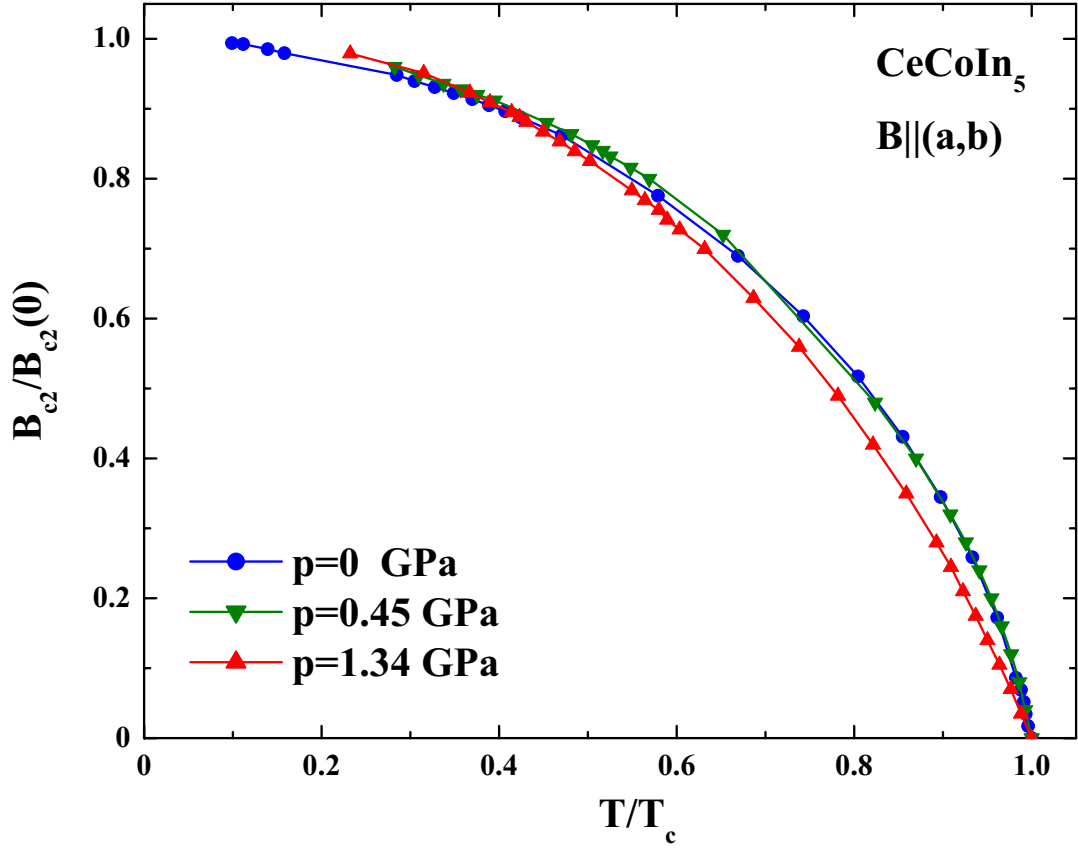
Figure 3.26: $B_{c2}/B_{c2}(0)$ as function of T/T_c. For $p = 1.34$ GPa a clear enhancement of B_{c2} is visible as the superconducting transition becomes first-order.

Maki parameter α.

In order to further check for the consistency of the model used we compare the Pauli field calculated with the theoretical g-values against the experimental findings. To obtain B_P we follow the scheme proposed by Clogston [13] and adapt it to d-wave pairing. In the weak coupling limit for a d-wave superconductor, the superconducting gap can be expressed as:

$$\Delta_0 = 2.14 \, k_B T_c \quad [39, 131].\tag{3.19}$$

The condensation energy ΔF for a d-wave superconductor is given by:

$$\Delta F = \frac{1}{4} N(0)\Delta_0^2 \quad [132],\tag{3.20}$$

where $N(0)$ is the density of states at the Fermi-level and the normal state spin

P (GPa)	0	0.45	1.34
T_c (K)	2.242	2.428	2.584
$B_{c2}(0)$ (T) for $B \parallel (a,b)$	11.6	12.5	14.3
$(\partial B_{c2}/\partial T)_{T_c}$ (T/K) for $B \parallel (a,b)$	-30.5	-29.4	-16.4
$B_{c2}(0)$ (T) for $B \parallel c$	4.9	4.7	4.2
$(\partial B_{c2}/\partial T)_{T_c}$ (T/K) for $B \parallel c$	-10.8	-10.2	-6.5
T_0 (K)	0.875 ± 0.050	1.025 ± 0.050	1.170 ± 0.100
T_0/T_c	0.39	0.42	0.44
T^* (K)	0.320 ± 0.015	0.370 ± 0.015	0.500 ± 0.050
T^*/T_c	0.14	0.15	0.19
T^*/T_0	0.36	0.36	0.43
α for $B \parallel (a,b)$	5.8	5.7	2.9
g	0.632	0.6365	0.554
v_a (cm/s)	7.47×10^5	7.89×10^5	9.59×10^5
v_c (cm/s)	3.39×10^5	3.37×10^5	3.60×10^5
$B_{c2}(0)^{fit}$ (T)	11.73	12.72	14.28

Table 3.5: Experimental values for T_c, $B_{c2}(0)$, $(\partial B_{c2}/\partial T)_{T_c}$, T_0 and T^* and estimation for α (see text for details). g-factor, Fermi velocity v_a and v_c, and $B_{c2}(0)^{fit}$ extracted from fitting of $B_{c2}(T)$.

susceptibility χ_n is:

$$\chi_n = \frac{1}{2}(g\mu_B)^2 \, N(0). \tag{3.21}$$

Upon applying magnetic field, the Cooper pairs are broken up when $B = B_P$ and the free energy will be lowered by:

$$\Delta F = \frac{1}{2}(\chi_n - \chi_s)B_P, \tag{3.22}$$

where the spin susceptibility in the superconducting state χ_s is zero for $T = 0$ K. We therefore obtain for the Pauli field in a d-wave superconductor:

$$B_P = \frac{\Delta_0}{g\mu_B} = 3.185(\text{T/K}) \, \frac{T_c}{g}. \tag{3.23}$$

This yields using our calculations for the g factor:

$$B_P(0 \text{ GPa}) \approx (11.3 \pm 0.4) \text{ T},$$

$$B_P(0.45 \text{ GPa}) \approx (12.2 \pm 0.4) \text{ T},$$

$$B_P(1.34 \text{ GPa}) \approx (14.8 \pm 0.4) \text{ T},$$

values which are in reasonable agreement with the experimental findings, indicating that the orbital-limiting effect is indeed very small.

In conclusion, we have studied the pressure evolution of the superconducting $B - T$ phase diagram of CeCoIn$_5$ by measurements of the specific heat. The system remains in the clean-limit, ℓ_{tr}/ξ_0 even increases upon applying pressure and the Maki parameter α remains well above the minimum required value for the formation of the FFLO state. Moreover, the FFLO anomaly inside the SC state is present at all pressures, reinforcing the existence of the FFLO state at low-T close to $B_{c2}(0)$. Under pressure, the FFLO region in the phase diagram expands to higher temperatures and higher fields indicating that the FFLO state becomes more robust upon increasing p. The first-order character of the SC phase transition at high fields is maintained under pressure and the FFLO state stability increases upon reducing the spin-fluctuations, as expected in the frame of the AFM-fluctuations based model proposed in [47]. Our result represents the first evidence of the existence of this state away from the influence of the strong magnetic fluctuations, clearly suggesting its genuine FFLO nature.

Since the FFLO state should be enhanced with increasing α our results imply that the AFM fluctuations tend to suppress the FFLO state (i.e., the AFM QCP is unrelated to the FFLO phenomena) and this is as well supported by theoretical calculations [47, 133]. The AFM fluctuations may lead to a damping of quasiparticle interactions and at least one origin of the increase of T_c upon applying pressure is the suppression of this damping effect. However, theoretical calculations [133] suggest that the AFM fluctuations have the opposite effect at high B and low-T and tend to increase B_{c2} at lower temperatures. This means that at high B and low-T

the AFM fluctuations are competitive to the paramagnetic effect. However, further theoretical insight is required to fully understand the intricate role played by the AFM fluctuations and the development of a theoretical model which accounts for the AFM fluctuations is under way [133].

We have analyzed the $B_{c2}(T)$ data of CeCoIn$_5$ within the microscopic model which includes:

a) the layered structure (or quasi-two-dimensionality);

b) $d_{x^2-y^2}$ symmetry for the SC order parameter ;

c) Gruenberg-Gunther ansatz.

This weak-coupling model gives an excellent description of the observed $B_{c2}(T)$ curves for both $B \parallel c$ and $B \parallel (a, b)$. From Table 3.5 we can read that there are pronounced changes in g and the Fermi velocity in the basal plane v_a, between $p = 0.45$ GPa and $p = 1.34$ GPa. The reduction of the effective mass m^* and the increase of v_a with rising p indicate a damping of the quasiparticle-quasiparticle interaction while the simultaneous enhancement of T_c might be induced by an increase of the chemical potential [125]. We recall that $p = 1.34$ GPa corresponds to the top of the SC dome in CeCoIn$_5$, in analogy to the top of the doping-induced dome in the high-T_c cuprate superconductors. However, in the high-T_c compounds, the anisotropy is increased as the antiferromagnetic fluctuations are enhanced with decreasing doping. This feature is opposite to the pressure effect in CeCoIn$_5$. Very strong fluctuations impede probably the formation of the FFLO state in high-T_c or organic superconductors while in CeCoIn$_5$ less pronounced fluctuations allow the inhomogeneous SC state to form [47]. We find that the damping of the fluctuations stabilize even further the FFLO state and this might be the route to induce a FFLO state in high-T_c or organic superconductors. However, there is thus an inescapable parallel between the high-T_c cuprates and CeCoIn$_5$ [125]. Indeed the exploration of CeCoIn$_5$ from this point of view should be very fruitful.

Chapter 4

Superconducting order parameter symmetry in UBe$_{13}$ probed by uniaxial stress

4.1 Introduction

Despite of more than two decades of intensive experimental and theoretical efforts to characterize the heavy-fermion superconductor (SC) UBe$_{13}$, many aspects of its physics remain enigmatic. It crystallizes in the NaZn$_{13}$ cubic structure with a lattice constant $a = 10.261$ Å and two different Be-sites [134]. The U-U distance is of about 5.13 Å with each U-atom placed in an almost cubic environment of 24 Be-atoms (Be-II sites) forming a cage around the U-atom. 12 out of the 13 Be-atoms of one formula unit sit on such Be-II sites, the last one being situated on a non-symmetry equivalent site, in an icosahedral environment. The CsCl-type sublattice of U-atoms and Be-I are presented in Fig. 4.1.

A full understanding of the physics in UBe$_{13}$, in both normal and superconducting state, remains elusive.
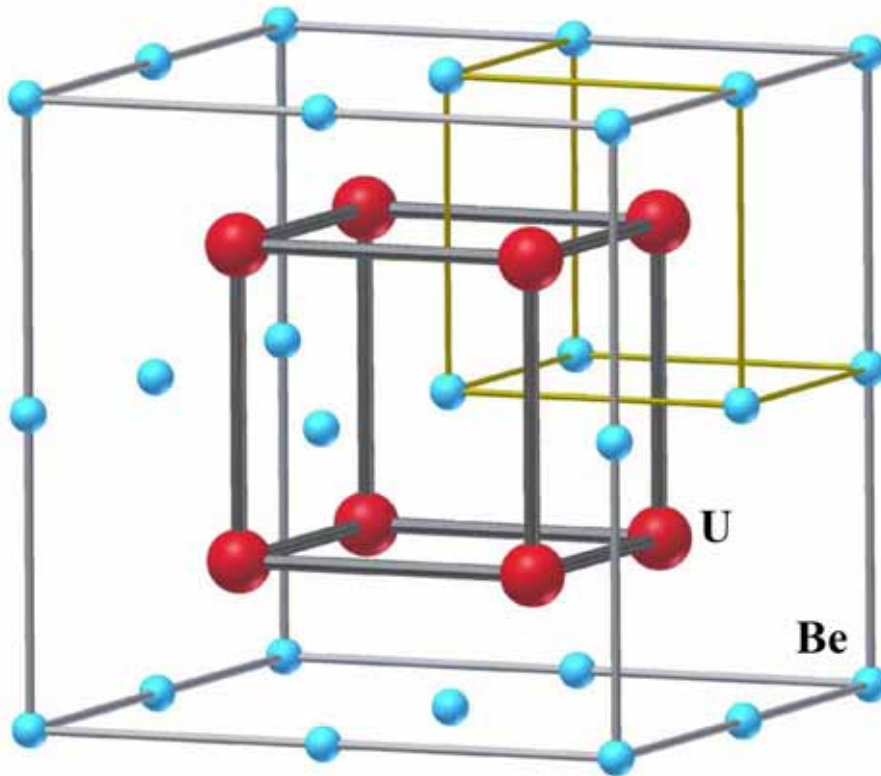
Figure 4.1: The crystal structure of UBe_{13}.

4.2 Normal state and non-Fermi liquid behavior in UBe_{13}

Even in the normal state the actinide intermetallic compound UBe_{13} is a rather un-usual metal. It was the first discovered actinide-based system which revealed extreme heavy-electron behavior [135]. Its properties are dictated by the partially filled $5f$ shell. It was shown by photoemission results [136] that the $5f$ electron level in UBe_{13} is close to the Fermi energy. Therefore, the heavy-fermion behavior that sets in below a characteristic fluctuation temperature T^*, would not correspond well to the Kondo picture which requires that the $5f$ states are well separated from the Fermi-level. However, the system still can be reasonably well described within the framework of the single- [137] or multi-channel [138, 139] Kondo effect and is in general considered to be a reasonably good example of a Kondo lattice. Moreover, the quasiparticles have
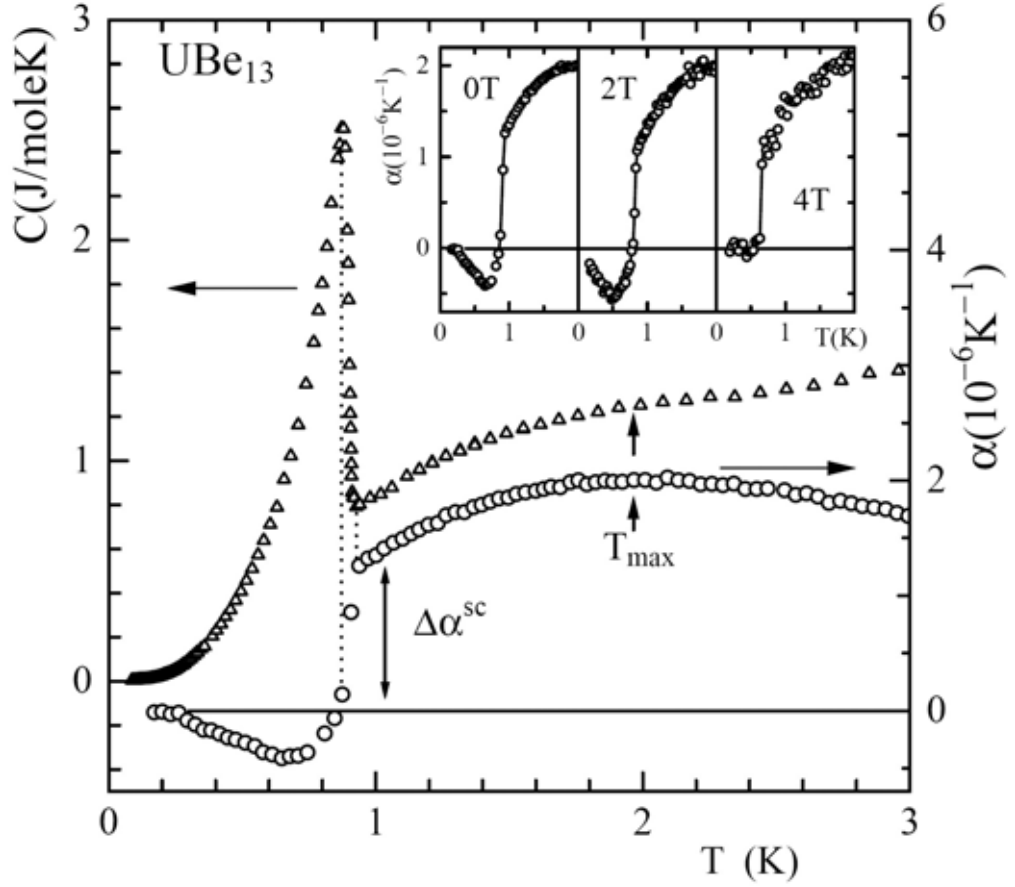
Figure 4.2: Low-T specific heat (C) and thermal expansion α of single crystalline UBe$_{13}$. The width of the SC transition is indicated by the vertical dotted lines. Vertical arrows indicate the position of the T_{max} (see text). From Ref. [144].

a record effective mass as a renormalization, by a factor of 1000 compared to the free electron mass, has been suggested [140, 141]. T^* estimates range from $T^* = 8$ K [142] to $T^* = 30$ K [143].

Furthermore, resistivity [135, 143], thermal expansion [144, 145] and specific heat measurements [146] (the specific heat and thermal expansion data are depicted in Fig. 4.2) suggest the presence of a second low energy scale $T_{max} \approx 2$ K, where these quantities exhibit an additional maximum. At low temperature $T \sim T_{max}$, a coherent Landau-Fermi liquid has not yet formed and the superconductivity emerges out of an anomalous non-Fermi liquid (NFL) state. If superconductivity is suppressed upon applying high magnetic field ($B \approx 12$ T), C/T displays a logarithmic increase with

reducing T [146] as is characteristic for NFL behavior. This is in contrast with many other heavy-fermion systems but is similar to $CeCoIn_5$ where the superconductivity sets in before the complete condensation of the Kondo centers [115]. It is possible that the magnetic fluctuations of the residual incoherent Kondo liquid are responsible for the anomalous behavior in the normal state.

Upon applying hydrostatic pressure, the 2 K maximum in both the specific heat and resistivity grows in magnitude and shifts to higher temperatures at roughly the same rate $dT_{max}/dp = 2.3$ K/GPa [147], whereas the superconducting transition temperature decreases at a rate of $dT_c/dp = -0.16$ K/GPa [148, 149].

The low temperature resistivity data follow a $\rho(T) = \rho_0 + bT^{3/2}$ dependence [150] in good agreement with theoretical prediction for a three-dimensional system of itinerant AFM spin fluctuations in the vicinity of a quantum critical point [151]. An additional anomaly is revealed as a broad minimum in thermal expansion [144, 145] (inset Fig. 4.2) and as an inflection point in $C/T(B)$ data [144]. This anomaly is gradually shifted to lower T upon applying magnetic field and finally suppressed at $B \approx 4$ T ($B^*(T)$ anomaly line in Fig. 4.3). It was suggested [152] that this might point out toward a field induced QCP responsible for the NFL behavior found in UBe_{13}.

Similar to $CeCoIn_5$, a low temperature upturn in C/T is observed for $T < 0.2$ K even after subtracting the nuclear contribution due to Zeeman splitting of the ^{9}Be spin states. Its origin is not yet understood but might be related to the possibility that superconductivity precludes a certain type of magnetic order. However, no clear signature of magnetic order has been observed down to the lowest temperature.

In addition, the two-channel Kondo effect has been proposed as well as a possible route to explain the non-Fermi liquid regime in UBe_{13} [153, 154]. UBe_{13} starts to recover Fermi liquid behavior at high magnetic fields, above $B = 14$ T, as the low-T resistivity turns to a $\Delta\rho \propto T^2$ dependency [150].

The normal state properties of UBe_{13} clearly reveal the attributes of a heavy-electron metal. The high temperature specific heat C for $T > 10$ K can be well

described by the typical expression for an ordinary metal

$$C(T) = \gamma T + \beta T^3, \tag{4.1}$$

where the first term is the electronic contribution to the specific heat while the latter is the lattice contribution for $T \ll \Theta_D$, where $\Theta_D \geq 600$ K is the Debye temperature [155, 156]. The electronic specific heat divided by temperature C_{el}/T is strongly T-dependent below 7 K and, upon reducing T increases its value by more than a factor of 4 down to $T = 1$ K. This upturn of C_{el}/T with decreasing temperature is a general feature of heavy-electron systems [157].

The magnetic susceptibility χ of UBe$_{13}$ at elevated temperatures shows a Curie-Weiss type behavior with an effective moment $\mu_{eff} = 3.05\mu_B$/U ion and a negative paramagnetic Curie-Weiss temperature $\theta = -53$ K [155]. This indicates the existence of fairly well localized moments due to the partially filled $5f$-electron shell of the U atoms. Below $T = 120$ K, deviations from the Curie-Weiss law are detected and attributed to single-ion effects [142]. At low temperatures, $T < 1.2$ K, the magnetic susceptibility becomes almost temperature independent, which is again regarded as general feature of heavy-electron systems. The room temperature resistivity is rather large ($\rho(300$ K$) \approx 100$ $\mu\Omega$cm [135]) compared to ordinary metals. On cooling from room temperature, $\rho(T)$ steadily increases and saturates around $T = 10$ K and shows the already mentioned distinct maximum at $T_{max} \approx 2$ K. Just above the superconducting transition $\rho(T)$ has still a very high value ($\rho(1$ K$) \approx 200$ $\mu\Omega$cm [135]) attributed to scattering on magnetic fluctuations.

4.3 Unconventional superconductivity in UBe$_{13}$

UBe$_{13}$ was the second heavy-fermion after CeCu$_2$Si$_2$ [158] discovered to display superconductivity [135]. The superconductivity in UBe$_{13}$ has been found to be of extreme type-II, with a coherence length $\xi_0 \approx 50$ Å and a penetration depth $\lambda(0) \approx$ 8000 Å yielding a Ginzburg-Landau parameter $\kappa \approx 150$ [159]. The superconducting phase transition temperature T_c depends considerably on the type of the sample.
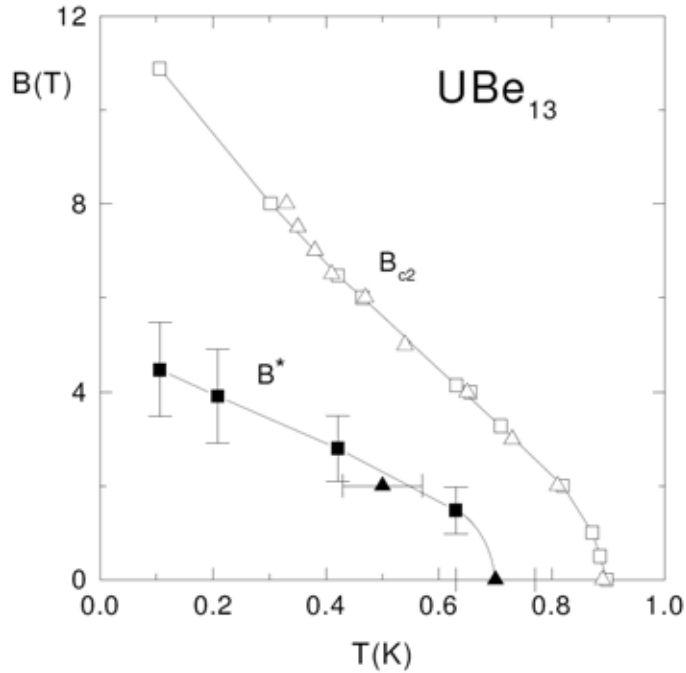
Figure 4.3: The upper critical field B_{c2} and the magnetic anomaly line B^* as determined by specific heat (squares) and thermal expansion (triangles). From Ref. [144].

There are two classes of UBe$_{13}$ single crystals [160] which, however, are not much different in their impurity content: the "H"-type ("high-T_c", $T_c \approx 0.9$ K) and "L"-type ("low-T_c", $T_c \approx 0.75$ K). A comparative investigation of both types reveals important differences, both in normal and superconducting state [160]. The determining factor leading to "L"- or "H"-type behavior is most likely related to details of the sample preparation process.

The enormous Sommerfeld coefficient $\gamma \approx 1.1$ J/molK^2 [135], a specific heat jump ratio $\Delta C/\gamma T_c \approx 2.5$ [161], considerably larger than the BCS value of 1.43 and an energy gap $2\Delta/k_B T_c \approx 6.7$ [162] (BCS value: 3.5) clearly point to strong coupling effects in the superconducting UBe$_{13}$. Several experiments probing the superconducting state of this material, revealed anomalous features which are regarded as evidence for unconventional superconductivity. Thus, well below T_c, the penetration depth $\Delta\lambda \propto T^2$ [163, 164] and $C \propto T^3$ [157], therefore departing from the temperature dependence expected for a conventional superconductor. NMR spin-lattice relaxation rate measurements [86] find $1/T_1 \propto T^3$ strongly deviating from

the exponential temperature dependence predicted by the BCS theory. Moreover, no Hebel-Slichter coherence peak has been observed. All these are taken as evidences for a strongly anisotropic order parameter, for which the gap function shows zeros on certain parts of the Fermi-surface, in contrast with the overall non-zero gap function of a conventional superconductor. The most compelling evidence obtained so far for unconventional superconductivity regards the giant ultrasonic absorption anomaly observed directly below T_c [8, 9] which was ascribed to collective modes or domain-wall damping due to a multi-component order parameter [10].

The $B - T$ phase diagram (Fig. 4.3) is quite unusual as the upper critical field curve $B_{c2}(T)$ shows an inflection point around $T = 0.45$ K (visible only for the "H"-type samples) and has a huge initial slope $\partial B_{c2}/\partial T|_{T_c} \approx 55$ T/K, one of the highest ever reported for a bulk superconductor [141, 165]. Even higher values, ranging from 100 T/K to infinity have been reported in [166]. The anomalous inflection point in the $B - T$ phase diagram was suggested to reflect the formation of an FFLO state [165], a scenario which however has not been confirmed. The zero temperature value of the upper critical field is around $B_{c2}(0) \approx 14$ T (for "H"-type) [165], extremely large for a superconductor with a superconducting transition temperature of less than $T_c = 1$ K. Lower values of $B_{c2}(0) \approx 8$ T have been reported for the "L"-type crystals [160]. The lower critical field $B_{c1}(0)$ was reported to be around 4.2 mT and to decrease quadratically as T increases [167].

4.4   Possible uniaxial strain effect on the SC order parameter

The behavior of a multi-component order parameter for an anisotropic superconductor (with p- or d-wave pairing symmetry) under uniaxial stress has been theoretically investigated by M. Sigrist, R. Joynt and T. M. Rice [11, 12]. By lowering the crystal symmetry in such a non s-wave superconductor, the degeneracy in the order parameter representation might be lifted, leading to a split of the superconducting phase

transition. In the following we are referring to the original analysis of M. Sigrist *et al.* [11, 12] resuming our attention to the effect on the order parameter of the strain applied along a main crystal axis in a cubic crystal.

In a system with spin-orbit coupling only the following symmetry transformations are possible:

- proper rotation transformation $\hat{R}$ which is the point group of the lattice;

- time reversal symmetry;

- inversion symmetry;

- $U(1)$ gauge transformation which corresponds to a multiplication with a phase factor.

The possible superconducting phases for cubic systems including spin-orbit coupling have been catalogued in [168, 169]. For such a crystal structure (symmetry group O) with p- or d-wave pairing, four different irreducible representations are possible for the symmetry group. Following Blounts notations [169] they are: Γ_1 - one dimensional, Γ_3 - two dimensional, Γ_4 and Γ_5 both three dimensional (see table 4.1).

Table 4.1: Cubic basis functions for different irreducible representations following Ref. [169].

Irreducible representations	Cubic basis functions
Γ_1	$\mathbf{d}(\Gamma_1) = \frac{1}{\sqrt{3}}(\hat{\mathbf{x}}k_x + \hat{\mathbf{y}}k_y + \hat{\mathbf{z}}k_z)$
Γ_3	$\mathbf{d}(\Gamma_3, u) = \frac{1}{\sqrt{6}}(2\hat{\mathbf{z}}k_z - \hat{\mathbf{x}}k_x - \hat{\mathbf{y}}k_y)$
	$\mathbf{d}(\Gamma_3, v) = \frac{1}{\sqrt{2}}(\hat{\mathbf{x}}k_x - \hat{\mathbf{y}}k_y)$
Γ_4	$\mathbf{d}(\Gamma_4, x) = \frac{1}{\sqrt{2}}(\hat{\mathbf{y}}k_z - \hat{\mathbf{z}}k_y)$
	$\mathbf{d}(\Gamma_4, y) = \frac{1}{\sqrt{2}}(\hat{\mathbf{z}}k_x - \hat{\mathbf{x}}k_z)$
	$\mathbf{d}(\Gamma_4, z) = \frac{1}{\sqrt{2}}(\hat{\mathbf{x}}k_y - \hat{\mathbf{y}}k_x)$
Γ_5	$\mathbf{d}(\Gamma_5, \xi) = \frac{1}{\sqrt{2}}(\hat{\mathbf{y}}k_z + \hat{\mathbf{z}}k_y)$
	$\mathbf{d}(\Gamma_5, \eta) = \frac{1}{\sqrt{2}}(\hat{\mathbf{z}}k_x + \hat{\mathbf{x}}k_z)$
	$\mathbf{d}(\Gamma_5, \zeta) = \frac{1}{\sqrt{2}}(\hat{\mathbf{x}}k_y + \hat{\mathbf{y}}k_x)$

Since the system of these basis functions is complete, a general gap function may be written as linear combination:

$$\mathbf{d}(\mathbf{k}) = \sum_{\Gamma} \sum_{\gamma} \lambda(\Gamma, \gamma) \mathbf{d}(\Gamma, \gamma, \mathbf{k}) \quad [12], \tag{4.2}$$

where $\Delta = i(\mathbf{d}(\mathbf{k})\sigma)\sigma_y$ is a 2×2 gap matrix and $\sigma = (\sigma_x, \sigma_y, \sigma_z)$ denotes the three Pauli spin matrices. $\lambda(\Gamma, \gamma)$ are arbitrary coefficients and $\mathbf{d}(\Gamma, \gamma, \mathbf{k})$ is the γ-th basis function of the representation Γ for the wave vector $\mathbf{k}$. The gap function near T_c is given by a linear eigenvalue equation:

$$\omega \mathbf{d}(\mathbf{k}) = -\frac{1}{2} N(0) \langle V(\mathbf{k}, \mathbf{k}') \mathbf{d}(\mathbf{k}') \rangle_{\mathbf{k}'} \quad [12], \tag{4.3}$$

where $N(0)$ is the density of states and $V(\mathbf{k}, \mathbf{k}')$ is the pairing interaction. The brackets represent an average over the whole Fermi-surface. The eigenvalue ω is related to T_c by:

$$T_c = 1.14 \, \varepsilon_c \, \mathrm{e}^{-\frac{1}{\omega}} \quad [12], \tag{4.4}$$

with ε_c the cutoff energy.

The form of the interaction potential determines which representation gives the highest T_c (i.e., the actual T_c) so that only one Γ enters the sum in equation 4.2. There remains a sum over γ with arbitrary coefficients giving a degeneracy greater or equal to the dimension of the representation. Under uniaxial stress this degeneracy might be lifted. If we regard λ as order parameter we can write the Ginzburg-Landau expansion for the free energy as:

$$F = F_s - F_n = \frac{2}{3} N(0) A(T) \sum_{\gamma} |\lambda(\Gamma, \gamma)|^2 + f(\lambda^4) \quad [12], \tag{4.5}$$

where $A(T) = \ln(T/T_c)$. $f(\lambda^4)$ denotes fourth order cross-terms in the order parameter which can be written for the cubic representation as:

for Γ_1: $f(\lambda^4) = \eta_1 |\lambda|^4$,

for Γ_3: $f(\lambda^4) = \eta_1(|\lambda_u|^2 + |\lambda_v|^2) + \eta_2(\lambda_u^* \lambda_v - \lambda_u \lambda_v^2)^2$,

for Γ_4 and Γ_5: $f(\lambda^4) = \eta_1(|\lambda|^2)^2 + \eta_2|\lambda^2|^2 + \eta_3(|\lambda_i|^2|\lambda_j|^2 + |\lambda_i|^2|\lambda_k|^2 + |\lambda_j|^2|\lambda_k|^2)$,
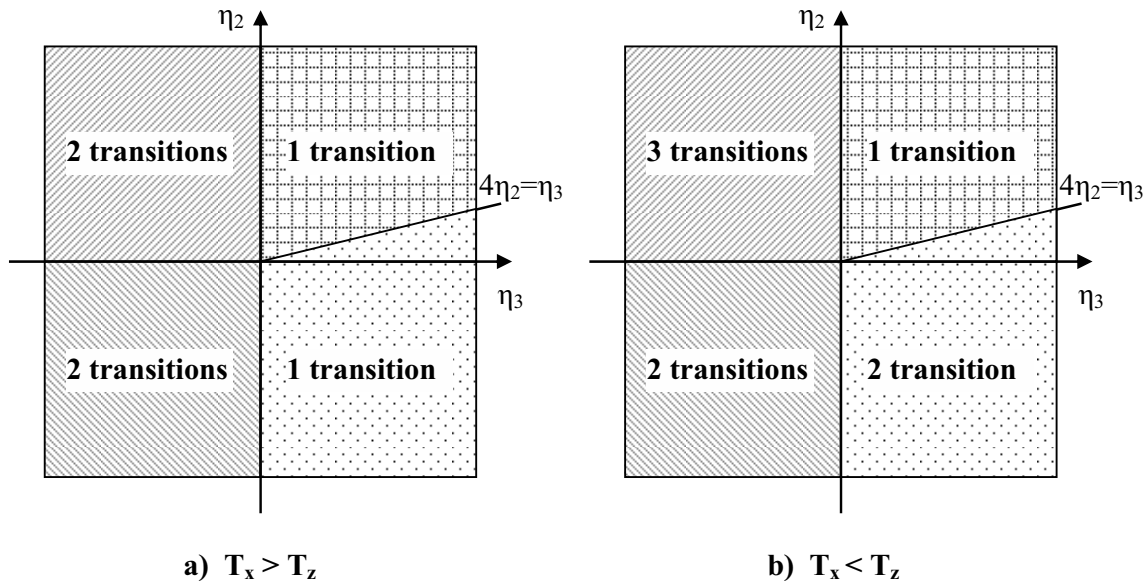
Figure 4.4: Summary of the possible phase diagrams for Γ_4 or Γ_5 representations.

where the coefficients η_i of the invariant terms are undetermined, independent parameters and $\lambda = (\lambda_x, \lambda_y, \lambda_z)$. The anisotropy in the second-order terms in equation 4.5 is due to the degeneracy of the basis functions of the same representation and therefore, they give the same transition temperature. However, uniaxial stress applied on a cubic crystal along the (0,0,1) direction, lowers its symmetry to a tetragonal one. The Landau expansion of the free energy for the Γ_4 case when the strain is applied along the z-axis becomes:

$$F = A_x(T)(|\lambda_x|^2 + |\lambda_y|^2) + A_z(T)(|\lambda_z|^2) + \eta_1(|\lambda|^2)^2 + \eta_2|\lambda^2|^2$$
$$+ \eta_3(|\lambda_x|^2|\lambda_y|^2 + |\lambda_x|^2|\lambda_z|^2 + |\lambda_y|^2|\lambda_z|^2), \qquad (4.6)$$

where $A_x(T) = A_y(T) = N(0)\log(T/T_x) \neq A_z(T) = N(0)\log(T/T_z)$ and T_x and T_y are the two superconducting transition temperatures. For stability $\eta_1 > 0$ is required but the η_2 and η_3 values have no additional constrains. Qualitatively η_3 determines the anisotropy. Depending on the sign of η_3 and on how T_x compares to T_z multiple superconducting transitions are possible as can be seen in Fig. 4.4. A generic phase diagram for Γ_4 and strain along z with $T_x > T_z$ and $\eta_3 < 0$ is depicted in Fig. 4.5.

For the Γ_5 representation the form of the Landau free energy is identical with the Γ_4 case, only the basis functions are different. Therefore the phase diagrams for those
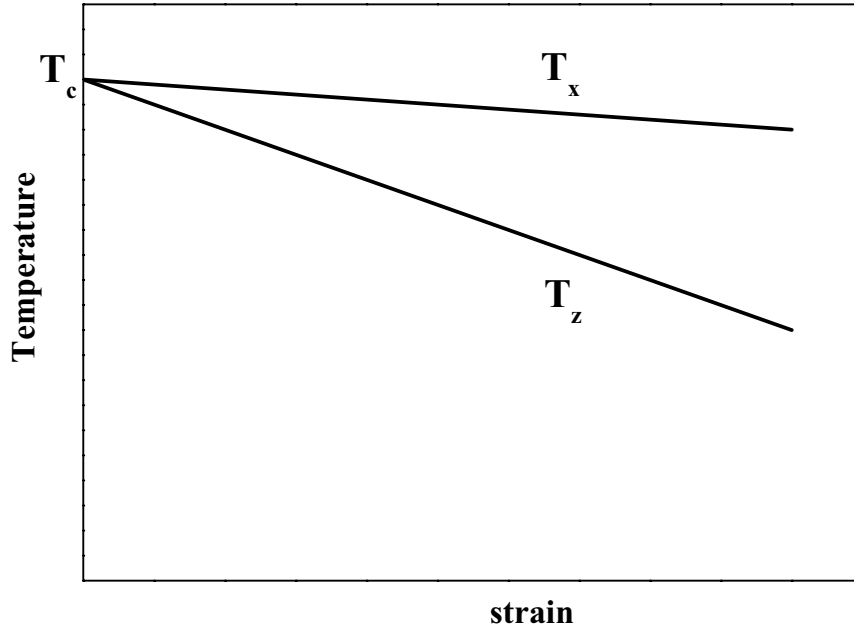
Figure 4.5: Generic phase diagram in 3D representation, Γ_4 or Γ_5 for $T_x > T_z$ and $\eta_3 < 0$.

two representations are identical. However, for the two dimensional Γ_3 representation in the case of a tetragonal distortion, the free energy is:

$$F = A_u(T)|\lambda_u|^2 + A_v(T)|\lambda_v|^2 + \eta_1(|\lambda_u|^2 + |\lambda_v|^2)^2 + \eta_2(\lambda_u^*\lambda_v - \lambda_u\lambda_v^*) \qquad (4.7)$$

with $A_u \neq A_v$ and $\eta_1 > 0$. A splitting of the transition is possible for $\eta_2 > 0$ with a degenerated low temperature phase.

For the one dimensional Γ_1 representation no splitting of the phase transition can take place, only a shift of T_c. No splitting is expected for s-wave pairing as well. The analysis of Sigrist *et al.* [11, 12] does not distinguish between p- or d-wave symmetry as the results are qualitatively similar. The symmetry properties and therefore the possible phase diagrams are the same for both pairing cases.

For the UBe$_{13}$ case, assuming for the relative splitting $\Delta T_c/T_c \approx 20(c/a - 1)$ [11, 170], the splitting of the superconducting transition temperature is estimated to be around 0.5 K/GPa, where a and c are the lattice constants.

4.5 Effect of tetragonal distortion on the super-conducting transition in UBe$_{13}$

The theoretically predicted splitting of the SC phase transition as a crystal is distorted from a cubic to a tetragonal structure, was the motivation for us to measure, under uniaxial stress along [100] direction, the specific heat of high quality single crystals[1] of both "L"- and "H"-type [171].

Earlier specific heat measurements on "L"-type UBe$_{13}$ under uniaxial stress along the [110] direction show a linear decrease of T_c by approximately 10 mK/GPa but no double structure at T_c could be observed up to 0.68 GPa [172].

We measured the specific heat of our samples using an AC calorimetry method [66] which has the advantage of a high temperature resolution since enables heat-capacity measurements in a steady-state mode at continuously varying temperature. The UBe$_{13}$ crystals have been placed in the pressure cell between two stainless-steel anvils. In order to prevent the crystal from breaking and also to allow some sideways movement, we used copper foils and capton tape between the sample and the anvils. The pressure p on the sample, applied by a bellows filled with He via a very thin capillary, was kept constant within 10^{-4} GPa during a run using an proportional-integral pressure regulator at room temperature. For each run the pressure was increased linearly at a very low rate of approximative 0.075 kbar/hour. A RuO$_2$ thermometer and a 10 kΩ heater where attached to the sample using Ag-based glue, in a sandwich-like structure as described in the experimental introduction of this work. Superconducting wires were used for the electrical contacts for both, heater and thermometer. The "L"-type crystal had a mass of $m = 15.2$ mg and dimensions of 0.71 mm $\times$ 3.05 mm $\times$ 5.01 mm. For the "H"-type crystal, $m = 7.33$ mg and the dimensions were 1.095 mm $\times$ 1.355 mm $\times$ 1.417 mm. In both cases the force was applied parallel to the longer side of the crystal and the temperature oscillations were measured across the smaller dimension. An electrical current with frequency ω is applied through the heater resulting in sample-temperature oscillations ΔT_{ac} around

---

[1]The single crystals were prepared in the group of Prof. G. R. Stewart at the University of Florida, Gainesville, Florida, USA.
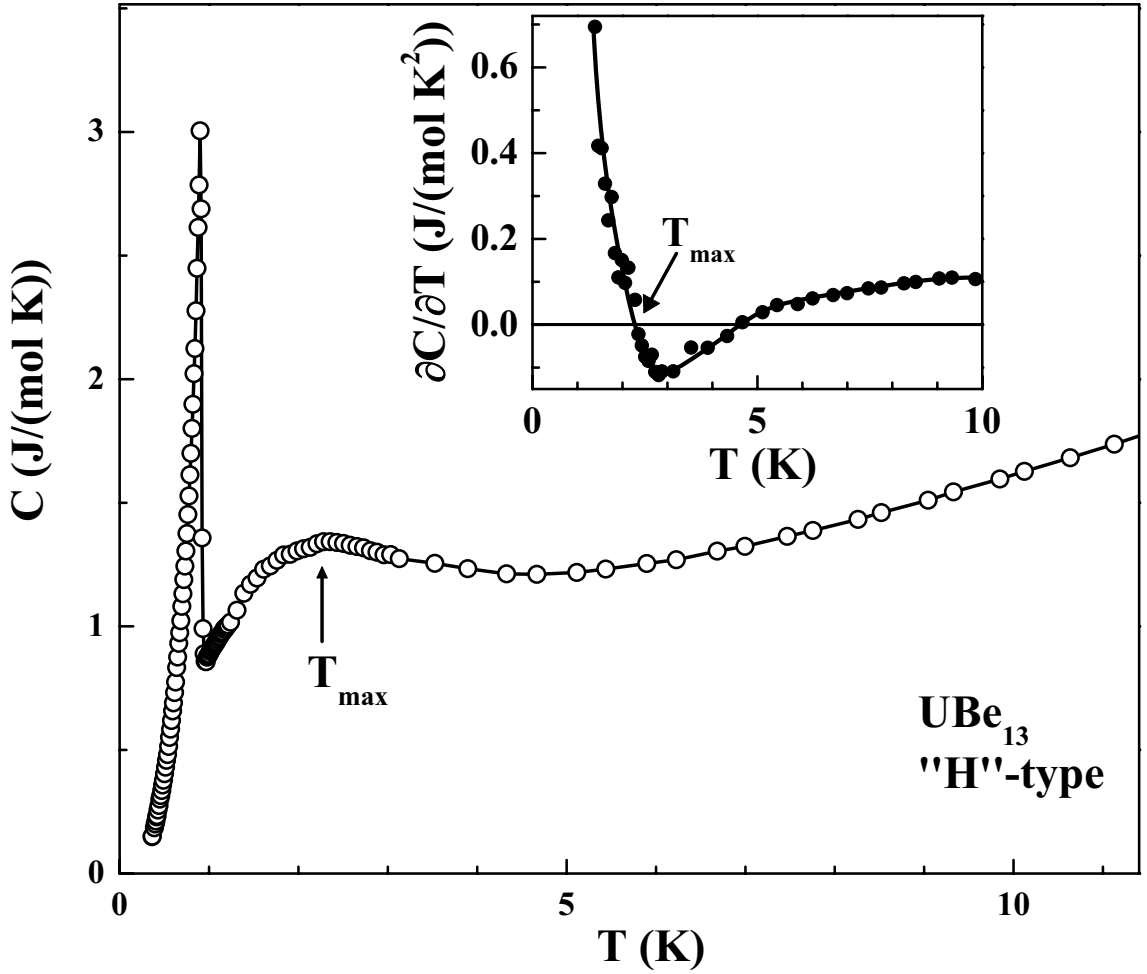
Figure 4.6: Specific heat as function of T at ambient pressure for a "H"-type single crystal. A clear maximum is observed at $T_{max} = 2.25$ K. Inset: $\partial C/\partial T(T)$ used to define T_{max}.

a mean temperature T. The specific heat of the sample is given by

$$C = F(\omega, \tau_i, \tau_e)P/(2\omega\Delta T_{ac}), \tag{4.8}$$

where P is the heating power and F is the frequency response function depending also on the internal and external relaxation times, τ_i and τ_e, respectively (for details see the experimental chapter). The sample thickness should be well below the thermal diffusion length and $1/\tau_e \ll \omega \ll 1/\tau_i$. When these conditions are fulfilled $F(\omega) \approx 1$. The thermal diffusion length is given by
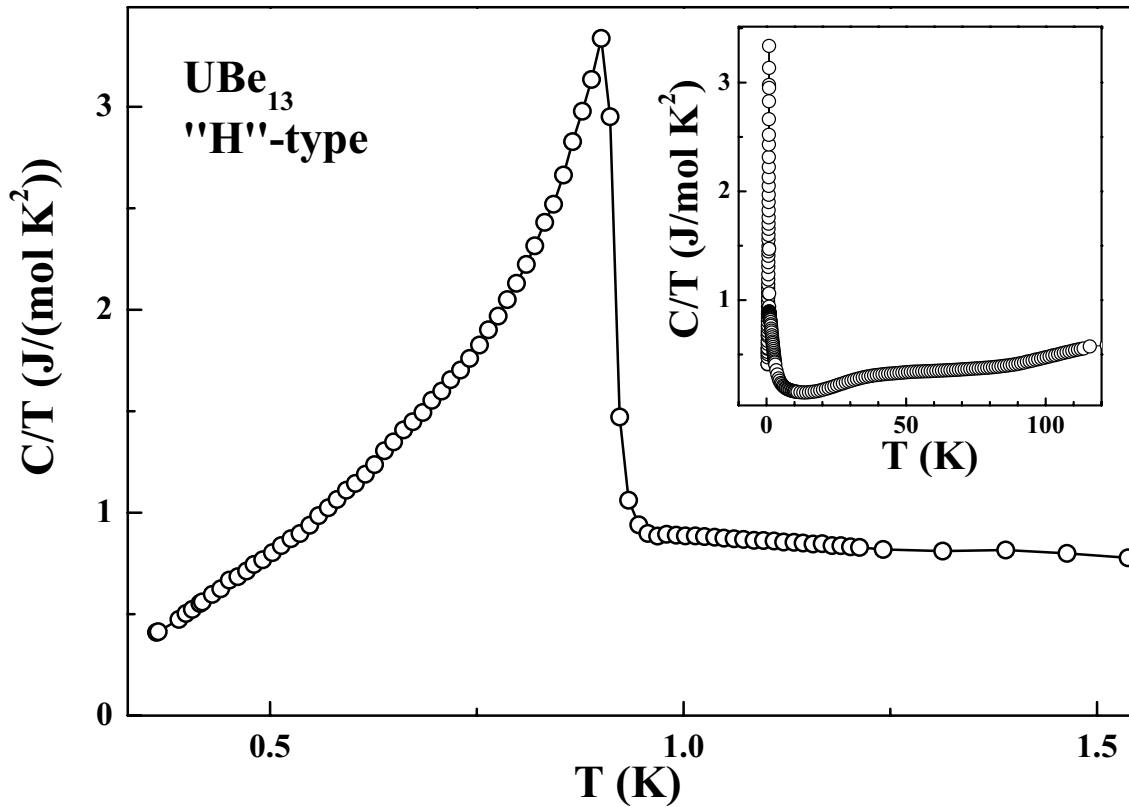
$$l = \sqrt{\frac{\kappa}{\omega\rho C}}, \tag{4.9}$$

Figure 4.7: C/T as function of T for the "H"-type single crystal at ambient pressure. Inset: $C(T)/T$ at high-T.

where κ is the thermal conductivity and ρ is the density. At $T = 1$ K, with $\kappa = 0.433$ mW/(K cm) [173] we obtain for a measurement frequency of $\omega = 0.132$ Hz, $l \approx 3.16$ mm. A digital lock-in system amplifying only the difference between the actual thermometer signal and one corresponding to the averaged T was allowing for very low frequency measurements with high relative accuracy.

The specific heat of the same "H"-type single crystal used for the uniaxial stress studies was also measured at ambient pressure employing a relaxation method (Quantum Design PPMS), in order to have a reference for the absolute specific heat values. Our findings are in good agreement with the literature data: we find a sharp superconducting transition (Fig. 4.6) at $T_c = 0.92$ K with a jump in the specific heat of $\Delta C/(\gamma T_c) = 2.7$. The superconducting transition width is $\Delta T \approx 0.022$ K, an indication for the good sample quality. As well a broad maximum in $C(T)$ is clearly observed in the normal state at $T_{max} = 2.27$ K and depicted by the arrows
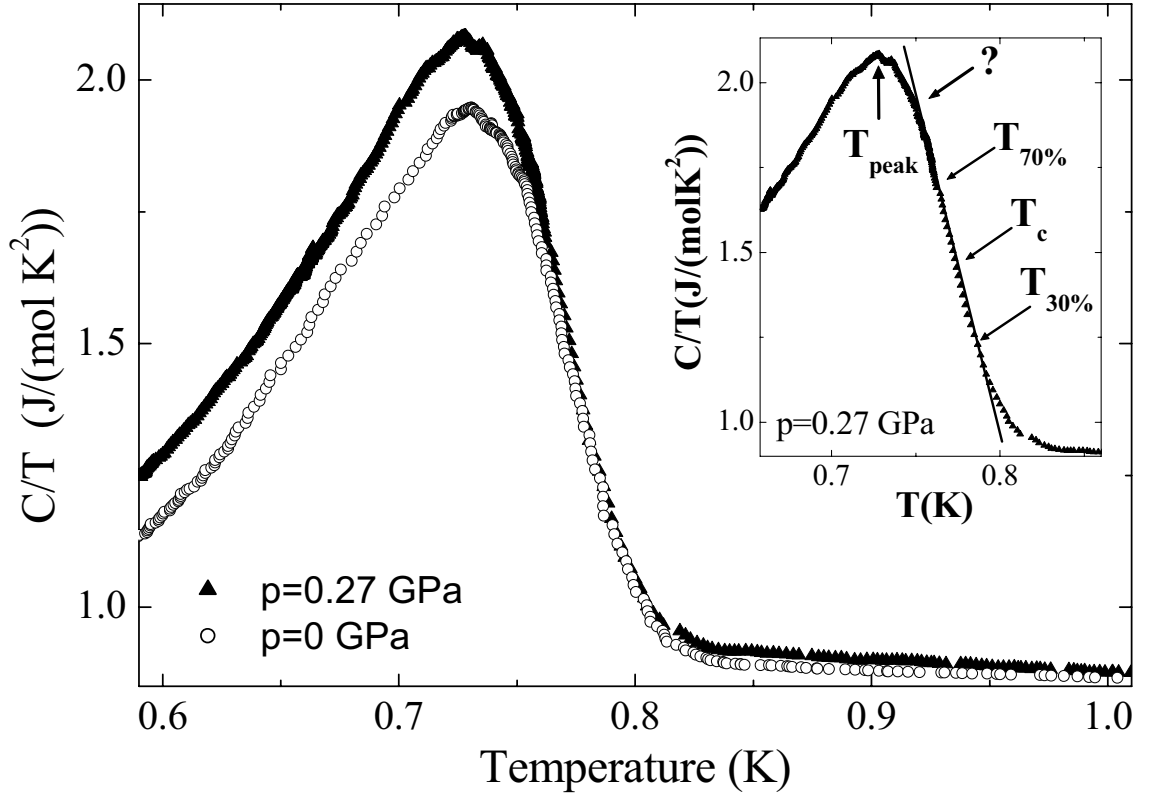
Figure 4.8: L-type UBe$_{13}$: C/T vs. T for $p = 0$ GPa and $p = 0.27$ GPa.

in Fig. 4.6. We define T_{max} as the temperature where $\partial C/\partial T = 0$ (inset Fig. 4.6). The $C(T)/T$ dependency is shown in figure 4.7 for low (main panel) and high (inset) temperatures. We find $\gamma = C/T(T = 1 \text{ K}) = 0.880 \text{ J}/(\text{mol K}^2)$ with $C(T)/T$ slightly increasing upon lowering T as the superconductivity sets in, with a slope of $\partial(C/T)/\partial(T) = -0.27 \text{ J}/(\text{mol K}^3)$. Another broad maximum is observed around $T = 31$ K in C/T caused probably by crystal field splitting effects [142].

Under uniaxial stress, the specific heat was measured at $0 \leq p \leq 0.27$ GPa for the "L"-type (Fig. 4.8) and at $0 \leq p \leq 0.55$ GPa for the "H"-type crystal (Fig. 4.9). The absolute values of $C(T)$ obtained by this technique differ from those published in the literature especially for the "H"-type sample due to a non-ideal frequency response caused by a less favorable sample geometry and the intrinsic low thermal diffusivity of UBe$_{13}$. Measurements at different ω have been performed to ensure a high relative accuracy of the data taken around the phase transition, where $F(\omega)$ is seen to be only
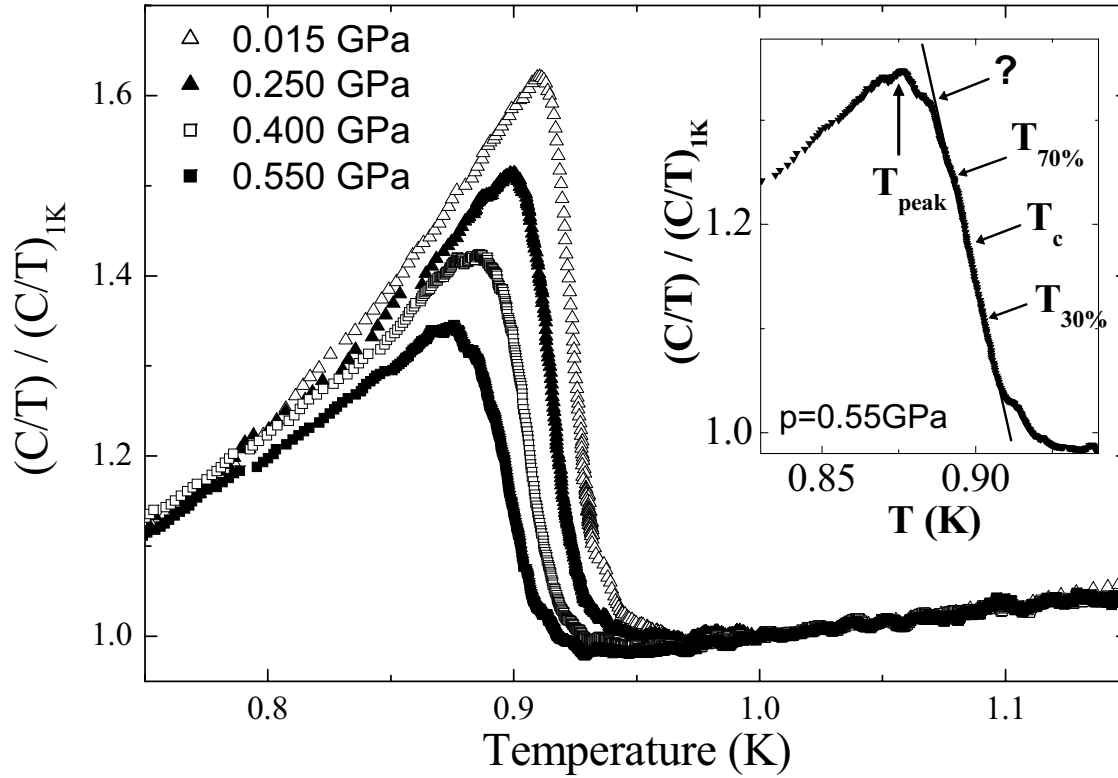
Figure 4.9: H-type UBe$_{13}$: C/T vs. T normalized to $C/T(1\ \mathrm{K})$. Inset: an anomaly develops at high pressure.

weakly T-dependent. To compensate for a weak p-dependence of $F(\omega)$, C/T for the "H"-type sample has been normalized against C/T at $T = 1$ K.

At $p = 0$ the transition width is about $\Delta T = 46$ mK for the "L"-type crystal ($T_c = 0.775$ K) and less than $\Delta T = 23$ mK for the "H"-type crystal ($T_c = 0.925$ K). T_c is taken at 50% of ΔC. The pressure dependence of T_c, together with that of $T_{30\%}$, $T_{70\%}$ (T at 30% and 70% of ΔC) and T_{peak} (T at the maximum point of the transition) are plotted in Fig. 4.10. For the "L"-type sample, T_c decreases very slowly with increasing p, $\partial T_c/\partial p = (8.5 \pm 6.8)$ mK/GPa, in good agreement with [172]. The "H"-type sample displays a stronger linear dependence of T_c on p with $\partial T_c/\partial p = (50 \pm 6)$ mK/GPa. This slope, given the cubic structure, multiplied by 3, is close to the value reported for hydrostatic pressure of $\partial T_c/\partial p_{hydrostatic} = 160$ mK/GPa [147].

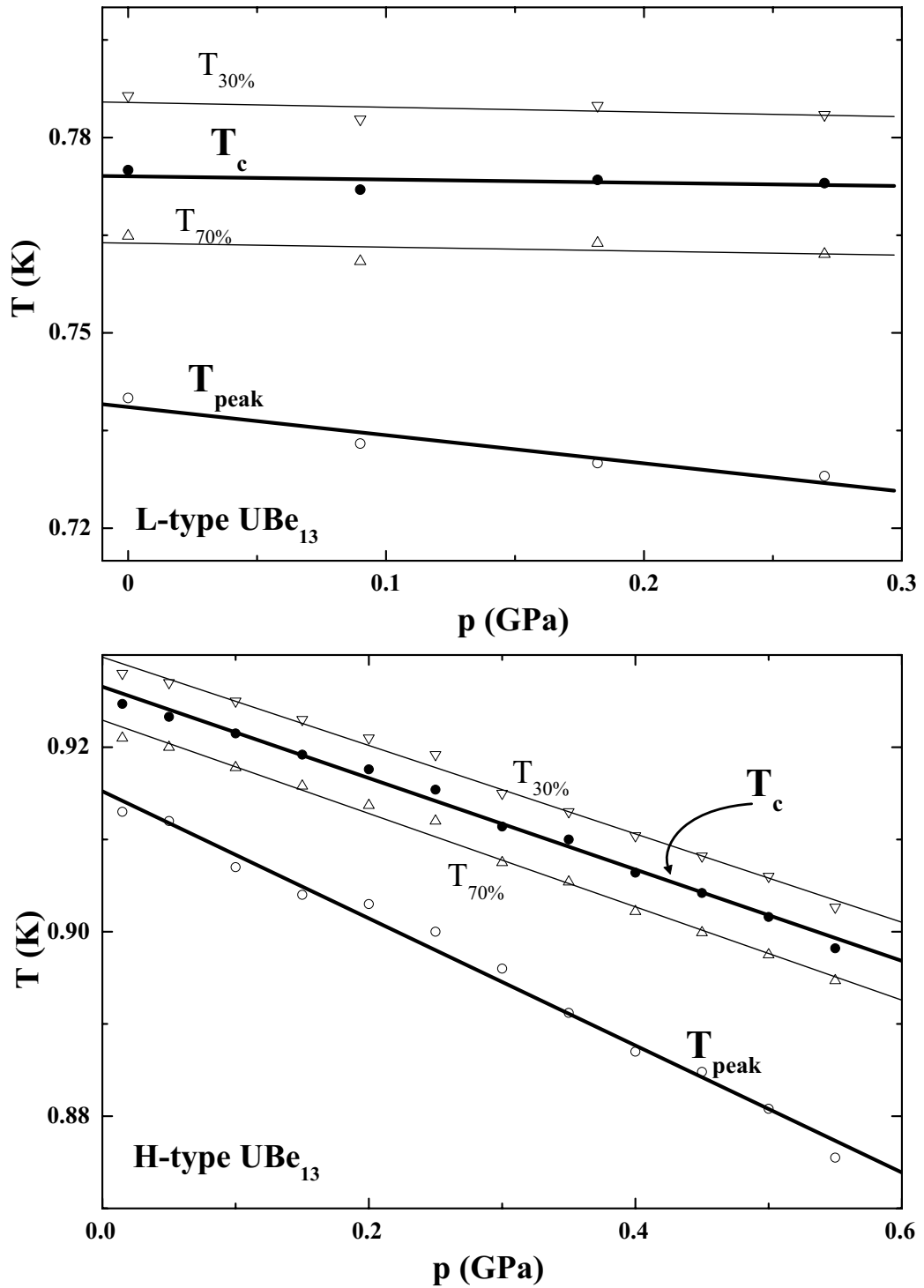In both cases T_c, $T_{30\%}$ and $T_{70\%}$ vary almost at the same rate while T_{peak} drifts

Figure 4.10: $T(p)$ phase diagram: T_c, $T_{30\%}$, $T_{70\%}$ and T_{peak} vs. pressure for both "L"- and "H"-type crystals.

away significantly, indicating that the transition becomes broadened at the top. More-over, a small change of the slope can be seen close to the maximum of the specific

heat at the transition. This feature is marked with "?" in the insets on Fig. 4.8 and 4.9 and is becoming more pronounced with increasing pressure. This is more clearly visible in the "H"-type case where a higher pressure is reached and this feature continuously develops into what could be regarded as a possible onset of a phase transition splitting (Fig. 4.9). Is should be mentioned that in the previous measurement of Reinders *et al.* [172], in the same pressure cell, with uniaxial stress along the [110] axis, no signature of a splitting or broadening of the transition has been observed up to $p = 0.68$ GPa. Their sample geometry was closer to our "L"-type crystal, therefore much longer than the "H"-type crystal we measured. In all cases the longer side of the sample is parallel with the applied force. Bulging resulting in pressure anisotropy is more probable to occur in longer samples. The fact that no such effect has been observed in [172] might be taken as an indication that the small feature we observed at the top of the transition might be indeed a genuine splitting. However, the effect is very small (≈ 0.01 K/GPa) compared with the predicted value (0.5 K/GPa [11]). It should also be emphasized that the theoretically calculated value is only a rough estimation based on the elastic constants in pure Be and that the real splitting rate, if any, might be considerably different.

4.5.1   Conclusions

Despite these observations, no unambiguous double structure could be detected so far for the "L"-type samples within our measurement resolution ($\Delta T_{ac} \sim 1$ mK on top of the transition). Moreover, the tiny splitting of T_c for the "H"-type sample has to be regarded carefully. Though improbable for such a small sample in this pressure range, a bulging of the sample which would induce a slight pressure inhomogeneity can not be completely ruled out. A lack of splitting could imply that: (1) the induced strain is still too small; (2) the order parameter is single component rather than multi-component; (3) depending on the details of the free energy fourth-order cross-terms may pin the order parameter at the higher temperature phase transition [11, 12] preventing the occurrence of the other one even for a multi-component order parameter.

Chapter 5

Interplay of superconductivity and charge-density wave instability in Tl$_x$V$_6$S$_8$

5.1   Introduction

For systems which display both superconductivity and charge-density wave (CDW) phenomena, superconductivity sets in from an already gapped normal state. It is important to understand, if the electron-hole gapping is detrimental or favorable to the SC state formation. The opening of a partial dielectric gap was shown to cause destructive effects on Cooper pairing [174–176] and, consequently, a direct way to enhance the superconducting transition temperature, T_c, would be to avoid the CDW formation. The model of partial gapping [177, 178] explains many of the characteristic features observed experimentally in CDW superconductors. However, there is also an opposite standpoint, according to which T_c is enhanced by the singular electron density of states near the dielectric gap edge [179–181]. This latter scenario, based on the model of the doped excitonic insulator with complete gapping [182] has not been verified experimentally so far.

The interplay of superconductivity and CDW instability remains therefore of great importance both theoretically and experimentally. In the following we study the properties of the SC and CDW states in Tl$_x$V$_6$S$_8$ compounds.

5.1.1 Crystal structure

TlV_6S_8 is a metallic system which has a quasi-one-dimensional structure based on hexagonal cells of the Nb_3X_4-type ($P6_3$ space group) [183]. VS_6 distorted octahedra are connected by shared edges and faces building up large hexagonal tunnels along the c-axis (Fig. 5.1). These tunnels are empty for the binary Nb_3X_4 structure but for TlV_6S_8, Tl-atoms are confined inside forming one-dimensional chains [183]. In addition, V-atoms are arranged in zigzag chains possessing a rather small interatomic distance (0.286 nm) comparable to the one found in the pure vanadium metal (0.261 nm). These zigzag-chains run along the c-axis as well and are well separated one to each other (Fig. 5.1, lower panel).

However, little is known about the electronic structure of this compound and scarce previous reports regarding its physical properties are often not in good agreement mainly due to the increased difficulty to grow high quality single crystals.

5.1.2 Possible charge-density wave formation in $Tl_xV_6S_8$

A slight change in the curvature for $\rho(T)$ at $T = T_{CDW}$ with 150 K $< T_{CDW} <$ 170 K [184] and a simultaneous drop in the magnetic AC susceptibility $\chi(T)$ [185] indicate a loss in density of states (DOS). This, coupled to a first-order structural phase transition revealed by X-ray measurements [186] and a sharp anomaly accompanied by latent heat in differential-scanning calorimetry (DSC) [184, 185] in the same temperature range, indicate the possible formation of a charge-density wave instability in this compound. Such an opening of a partial gap in the DOS is corroborated by calculations of the electronic band structure [187], which confirm nesting conditions for at least four characteristic wave vectors **k** as can be seen in Fig. 5.2. The band labeled 1 has considerable parallel regions connected by a nesting vector **k** along the Γ-A direction. For the same **k** direction there are also less prominent nesting regions of the band 3 sheet near the K point and to a lesser extent close to Γ. Also nesting conditions are fulfilled close to Γ for the bands 2 and 4.

Preliminary electron diffraction measurements reveal the existence of satellite
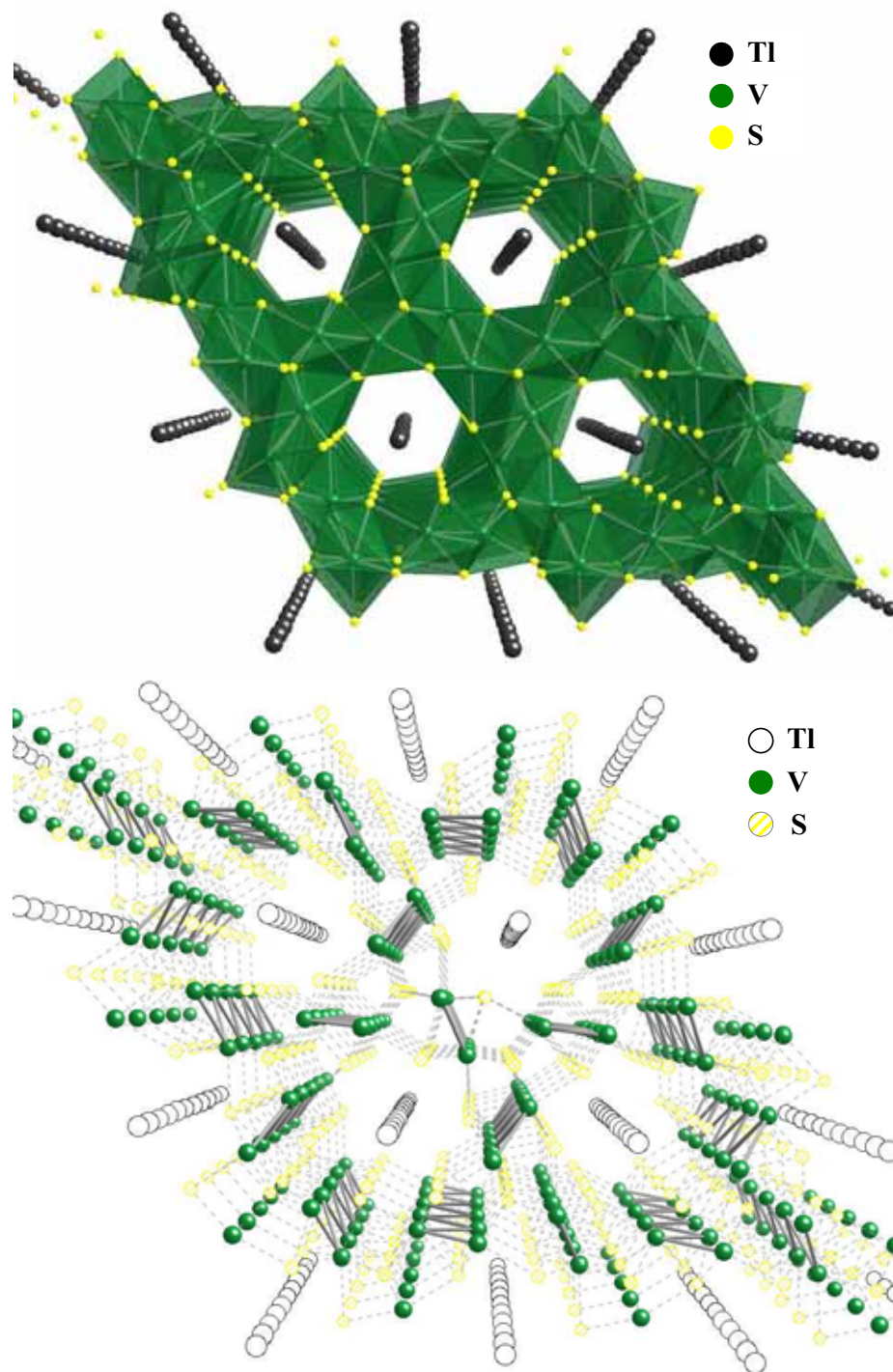
Figure 5.1: TlV_6S_8 crystal structure. Upper panel: VS_6 octahedra linked together forming large hexagonal tunnels along the *c*-axis. Lower panel: V-V zigzag chains are well separated one to each other.
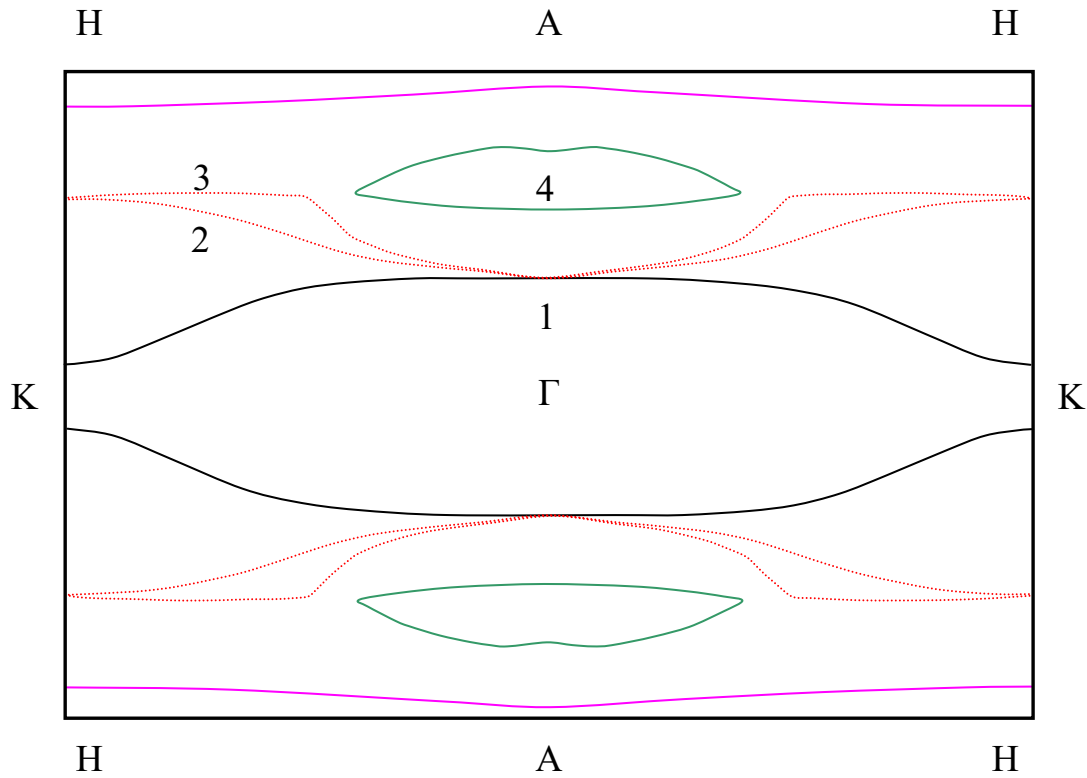
Figure 5.2: Fermi-surface sheets in the Γ-A-H-K plane. Nesting conditions are fulfilled for at least four wave vectors as explained in the text. Ref. [187].

spots at $T < T_{CDW}$ in addition to the main diffraction spots observed at low-T [184], similar to what was found for the CDW-compounds Nb_3Te_4 [188] and $InNb_3Te_4$ [189]. Moreover, the formation of a CDW state was suggested also for the iso-structural compounds AV_6S_8 with A = In, K, Rb and Cs and also for V_6S_8. This is an indication that the CDW instability might be a general feature of the whole sulfide series. The $\rho(T)$ dependency for selected members of the series is depicted in Fig. 5.3. An enhancement of $\rho(T)$ is observed for all the investigated compounds suggesting a reduction in the carrier density. The strongest anomaly with a clear hysteresis of about $\Delta T \approx 40$ K is found for the In compound.

5.1.3 Superconductivity in $Tl_xV_6S_8$

Despite the partial gapping at $T < T_{CDW}$, $Tl_xV_6S_8$ adopts a superconducting ground state at much lower temperatures. The superconductivity at $T_c \approx 3.5$ K was ini-

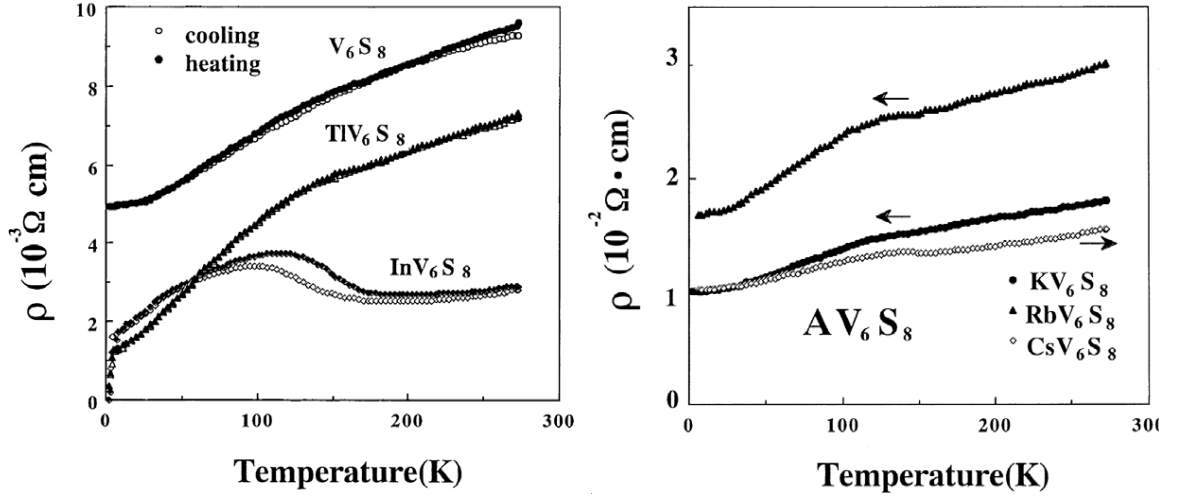Figure 5.3: The $\rho(T)$ dependency for different compounds of the AV_6S_8 series. Ref. [184]. For all the compounds an anomaly is observed in the high temperature range.

tially observed in 1995, in resistivity measurements on single crystals of $Tl_{0.1}V_6S_8$ and $Tl_{0.8}V_6S_8$ by Bensch *et al.* [190] and has been confirmed more recently by susceptibility studies on poly-crystalline samples [184, 191]. Similar to the high temperature anomaly, superconductivity is found to be a common feature among the members of the AV_6S_8 family as it is observed for intercalated Tl, In, K, Rb or Cs and also for the parent compound V_6S_8. At low temperatures all samples showed perfect diamagnetism (Fig. 5.4) and this was taken as an indication that superconductivity is a bulk property in this class of materials [184]. As the SC state sets in, a stepwise drop in susceptibility is reported for all the poly-crystalline samples [184, 191]. This feature is strongly influenced by the mechanical and thermal treatment received by the samples, being much reduced for the sintered ones. It was argued by Fujii *et al.* [191] that the higher temperature drop is a signature of intra-grain superconductivity while the low-T drop corresponds to the inter-grain transition temperature.

For $Tl_xV_6S_8$, a significant anisotropy is observed for the upper critical field B_{c2} determined from resistivity measurements on single crystals [190]. For $Tl_{0.8}V_6S_8$ for $B \parallel c$, $B_{c2}^{\parallel}(0) \approx 7$ T while for $B \perp c$, $B_{c2}^{\perp}(0) \approx 2.4$ T. The yielded anisotropy is $B_{c2}^{\parallel}(0)/B_{c2}^{\perp}(0) \approx 2.9$. This value seems to decrease slightly upon reducing the Tl content of the crystal [190]. Single crystal X-ray investigations reveal a reduction
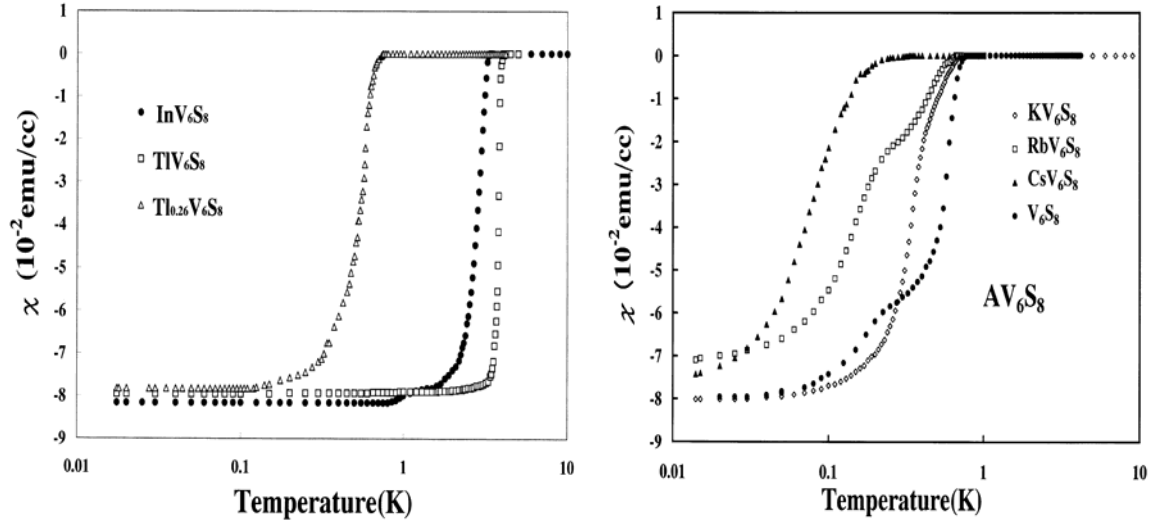
Figure 5.4: Temperature variations of the AC susceptibility for AV_6S_8 compounds. A clear stepwise decrease is observed for RbV_6S_8 and V_6S_8 samples. Ref. [184].

for the separation of the V-V zigzag chains upon decreasing Tl content [190]. The coherence lengths for the different field orientations are: $\xi^{\parallel} \approx 164$ Å and $\xi^{\perp} \approx 60$ Å almost unaffected by the amount of the intercalated Tl [190].

5.2   Interplay of SC and CDW in $Tl_xV_6S_8$

Even though bulk SC still has to be confirmed by Meissner effect or specific heat measurements, it appears challenging to understand how SC competes with the formation of the CDW. Moreover, if the CDW transition could be suppressed, an increase of T_c due to the increase of the DOS is expected. This is the aim of our studies of $Tl_xV_6S_8$ at different Tl-chain filling x and under hydrostatic pressure. In the following we present a thorough investigation of the atmospheric pressure properties by specific heat, resistivity and magnetization measurements together with a resistivity study under pressure.

5.2.1 Experimental setup

$Tl_xV_6S_8$ (x = 0.1, 0.15, 0.25, 0.47, 0.63 and 1) samples were pressed from powder[1] s into pellets and than sintered in closed silica tubes at $T = 800°C$ for seven days. A scanning electron microscope image of the powdered TlV_6S_8 sample, depicted in Fig. 5.5, clearly shows that the sample consists of small rod-like single crystals with lengths of roughly $10 - 30$ μm and $2 - 5$ μm in diameter.
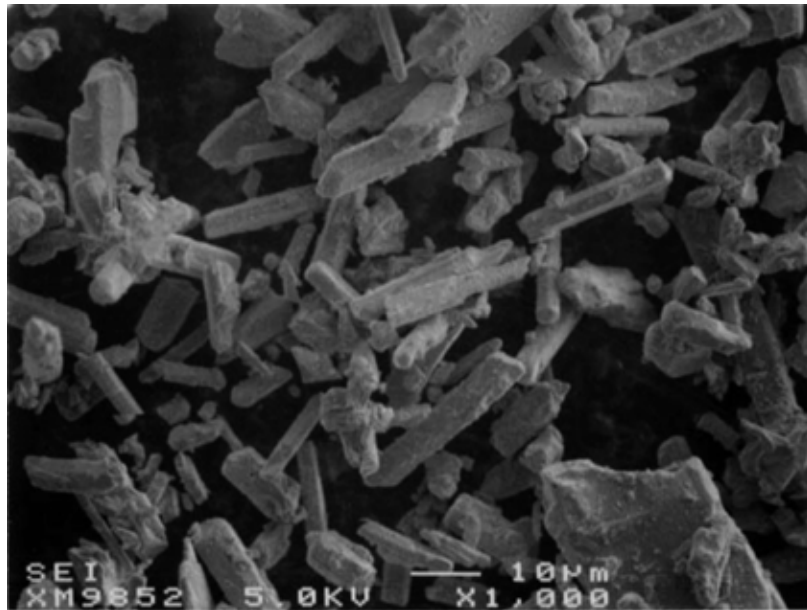
Figure 5.5: Scanning electron microscope image of the powdered TlV_6S_8 sample. Ref. [191].

During the sintering process the size of the crystals increases substantially and they start to merge. The actual sample composition for each nominal concentration was confirmed by X-ray and microprobe analysis.

For the resistivity experiments, the samples were cut in parallelepiped shape and on the clean surfaces gold wires were connected with gold paste. Standard four-probe AC resistivity measurements were performed at ambient pressure for all samples (0.35 K $< T <$ 300 K). In addition, for $x =$1, 0.15, 0.47 and 0.63, the resistivity, $\rho(T)$, was measured under hydrostatic pressure in a newly developed, double-wall, piston-cylinder type pressure cell at pressures up to $p = 2.5$ GPa. The pressure cell, described in the introductory part of this work, was designed to fit in a commercially

---

[1]The powder samples were prepared in the group of Prof. H. D. Hochheimer at Colorado State University, Fort Collins, USA.

Quantum Design PPMS. We used as pressure transmitting medium a mixture of n-pentane and iso-pentane which ensures excellent hydrostatic conditions. The shift of the superconducting transition temperature T_c of a Pb sample, used as manometer, was determined in a four-probe AC resistivity measurement and than converted into pressure using the $T_c(p)$ calibration from Ref. [60]. No pressure gradient was observed in the cell as the Pb sample was mounted along the whole sample space and its superconducting transition width remained narrow ($\Delta T_c \approx 5$ mK) and almost pressure independent.

Specific heat measurements employing a relaxation method (Quantum Design PPMS), were carried out at atmospheric pressure for the $x = 0.47$ and $x = 0.63$ concentrations. The weight of the samples were 5.23 mg and 86.97 mg, respectively. Moreover, DC magnetization measurements in a SQUID magnetometer (Quantum Design MPMS) and differential scanning calorimetry studies where performed for the $x = 0.63$ sample.

All the measurements (resistivity at all pressures, specific heat and magnetization) were performed both while cooling down and warming up in order to check for thermal hysteresis.

5.2.2   Influence of Tl content

For all Tl compositions studied, the resistivity measurements at ambient pressure showed an anomaly at $T = T_l$ upon cooling down and at $T = T_h$ while warming up (Fig. 5.6). The size of this anomaly varies strongly with the Tl content. T_l and T_h are defined as the temperatures where $\partial\rho/\partial T$ reaches a minimum while cooling down and warming up, respectively (Fig. 5.7). In the warming up temperature sweeps, $\rho(T)$, increases with higher absolute values around T_h than during cooling down. A clear thermal hysteresis (inset Fig. 5.6) which varies with the composition, is visible for all samples indicating a first-order phase transition. The resistivity measurements in magnetic field (not presented here) showed that both, the size of the transition anomaly and T_h are very robust against magnetic field as no effect was observed up to $B \approx 7$ T. T_l and T_h show a slight dependence on Tl concentration; they are
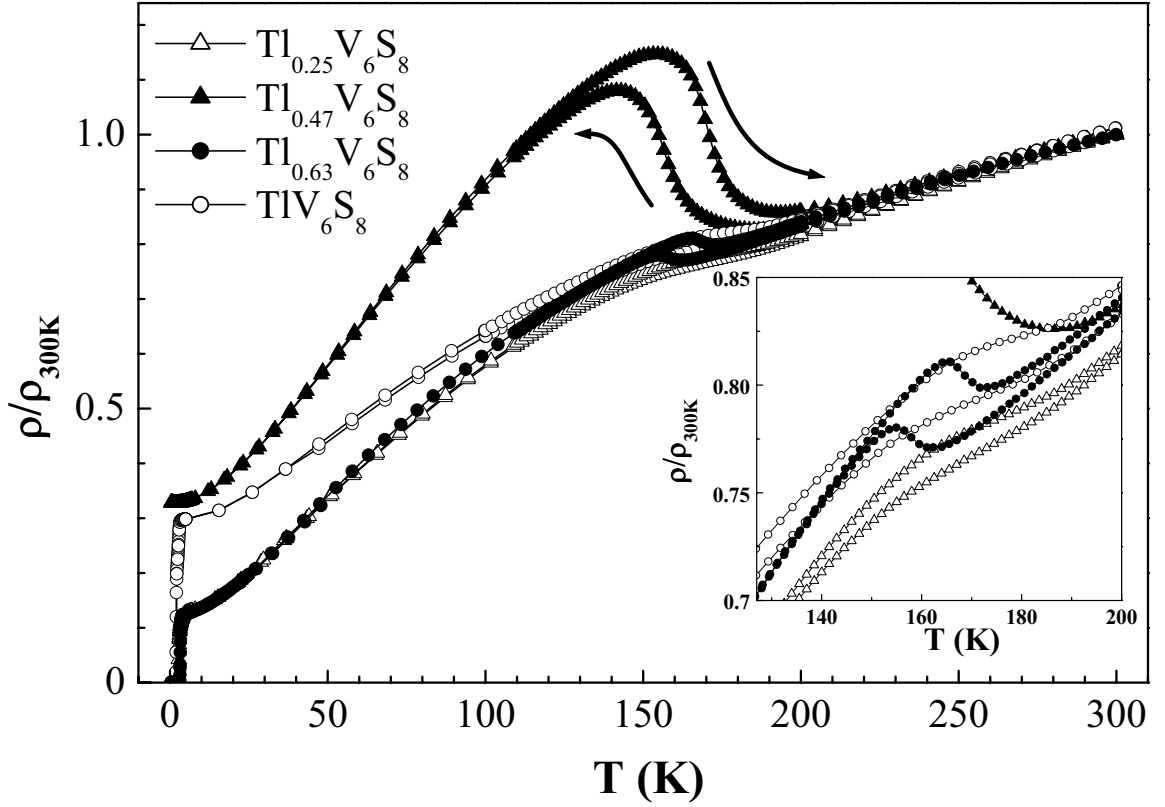
Figure 5.6: $\rho(T)/\rho(300K)$ dependency for different Tl concentrations. A clear anomaly and thermal hysteresis (inset) are visible for all the samples in the high temperature range.

continuously reduced upon increasing x up to $x = 0.63$ and than enhanced again at $x = 1$ (Table 5.1).

Table 5.1: T_h and T_l for different Tl concentration.

x	0.1	0.15	0.25	0.47	0.63	1
T_h (K)	179	175	172	170	169	178
T_l (K)	169	166	165	157	158	170

The strongly enhanced anomaly observed for $Tl_{0.47}V_6S_8$ corresponds to an increase in resistivity of about 36 %. Remarkably, this is the only composition, which does not display any signature of superconductivity. This might be taken as an
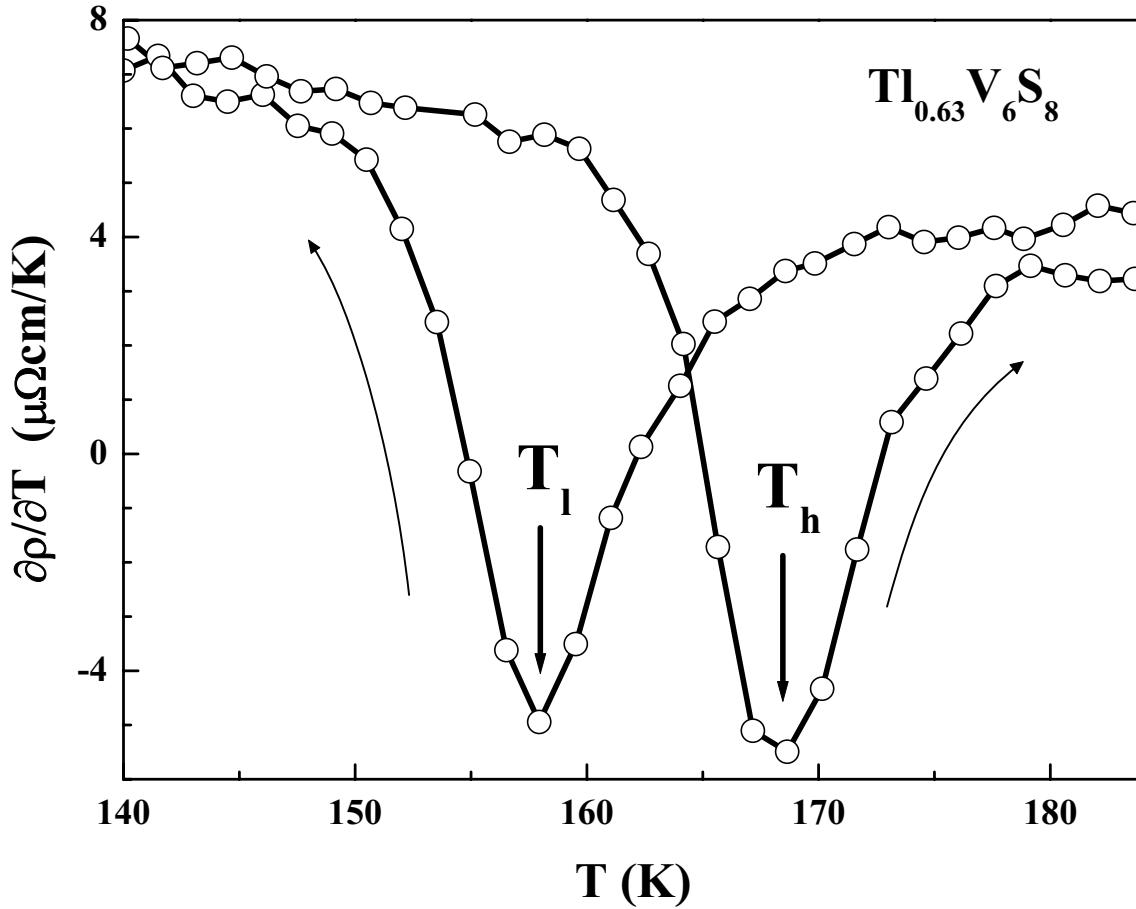
Figure 5.7: T_l and T_h are defined as the temperatures where $\partial\rho/\partial T(T)$ has a local minimum. Exemplified for $Tl_{0.63}V_6S_8$.

indication that the gap opened at the Fermi-surface due to the CDW instability is detrimental to SC. Moreover, a slight upturn of $\rho(T)$ could be observed for this sample at $T < 2$ K.

Zero resistivity in the temperature range of our cryostat, $T \geq 0.35$ K, was found only for $x = 0.25$, 0.63 and 1 at $T_c = 2.41$ K, 3.05 K and 1.72 K, respectively (Fig. 5.8). For $x = 0.10$ and 0.15, only the onset of superconductivity is visible below $T \approx 3.5$ K. A two-step transition as shown for TlV_6S_8 in the inset of Fig. 5.8 was also reported previously by Fujii *et al.* [191] and attributed to different T_c values for the intra-grain and inter-grain superconductivity. The upper temperature step is related to intra-grain SC while the zero resistance needs the development of inter-grain SC [191]. For $x = 0.25$ and $x = 0.63$, $\rho(T)$ drops to zero in one step. The width of
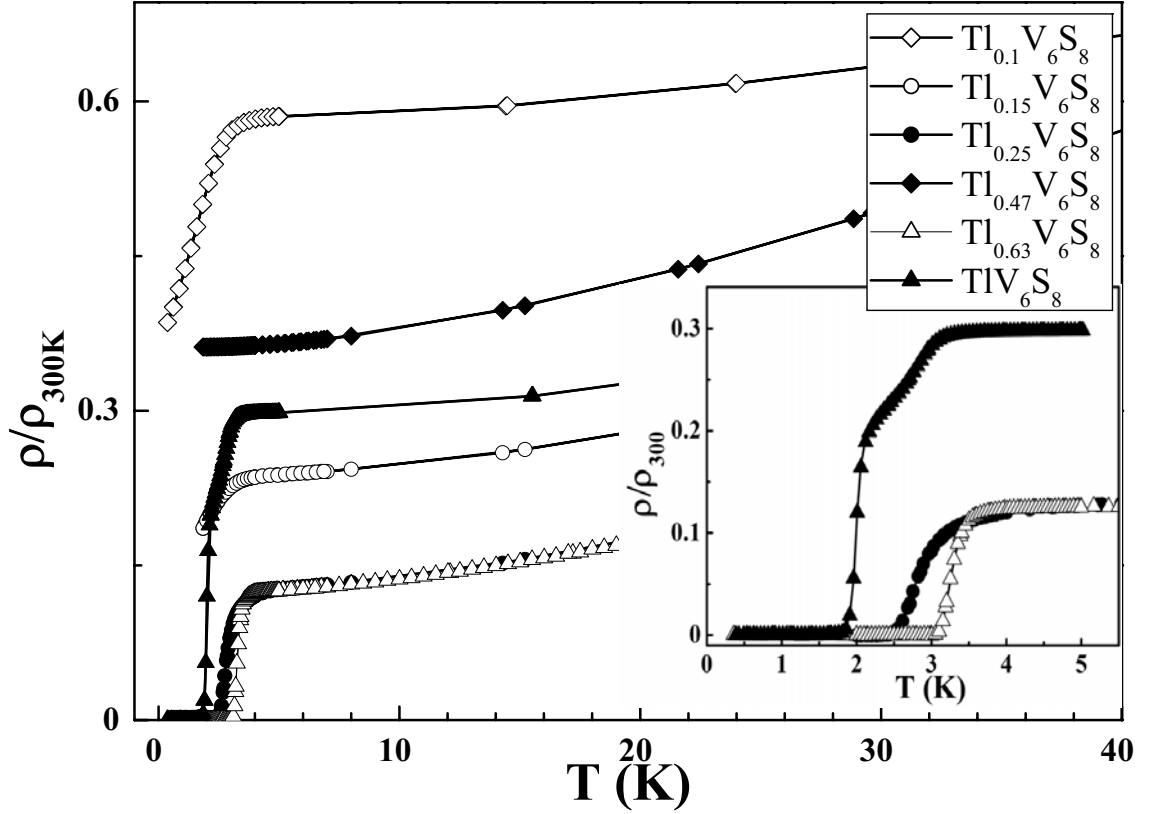
Figure 5.8: Low temperature dependency of $\rho(T)$ for different Tl contents. Zero resistivity is observed only for $x = 1$, 0.25 and 0.63. An onset of the SC transition is displayed by the $x = 0.1$ and $x = 0.15$ samples, while for $x = 0.47$ no trace of SC is observed. Inset: Two-step SC transition for $x = 1$.

the superconducting phase transition ΔT_c, is relatively large: $\Delta T_c \approx 1$ K for $x = 1$, $\Delta T_c \approx 0.5$ K for $x = 0.25$ and $\Delta T_c \approx 0.4$ K for $x = 0.63$. The strong variation of the normal state resistivity value among the measured samples could be related to the way the samples were prepared, especially to the mechanical treatment. The transition is sharper and the resistivity value just above the SC transition is lower for those samples for which a higher force was used for pressing the pellets: $x = 0.25$ and $x = 0.63$ (see the inset of Fig. 5.8). For all x, the SC upper critical fields are around $B_{c2}(0) \approx 3$ T.

The high temperature anomaly is also clearly evidenced by susceptibility measurements. A significant jump in $\chi(T)$ is observed upon cooling ($T \approx T_l$) and warming ($T \approx T_h$) as depicted in Fig. 5.9. We define T_h and T_l as local maxima in $\partial\chi(T)/\partial T$ upon cooling down and warming up, respectively (inset Fig. 5.9). The yielded val-
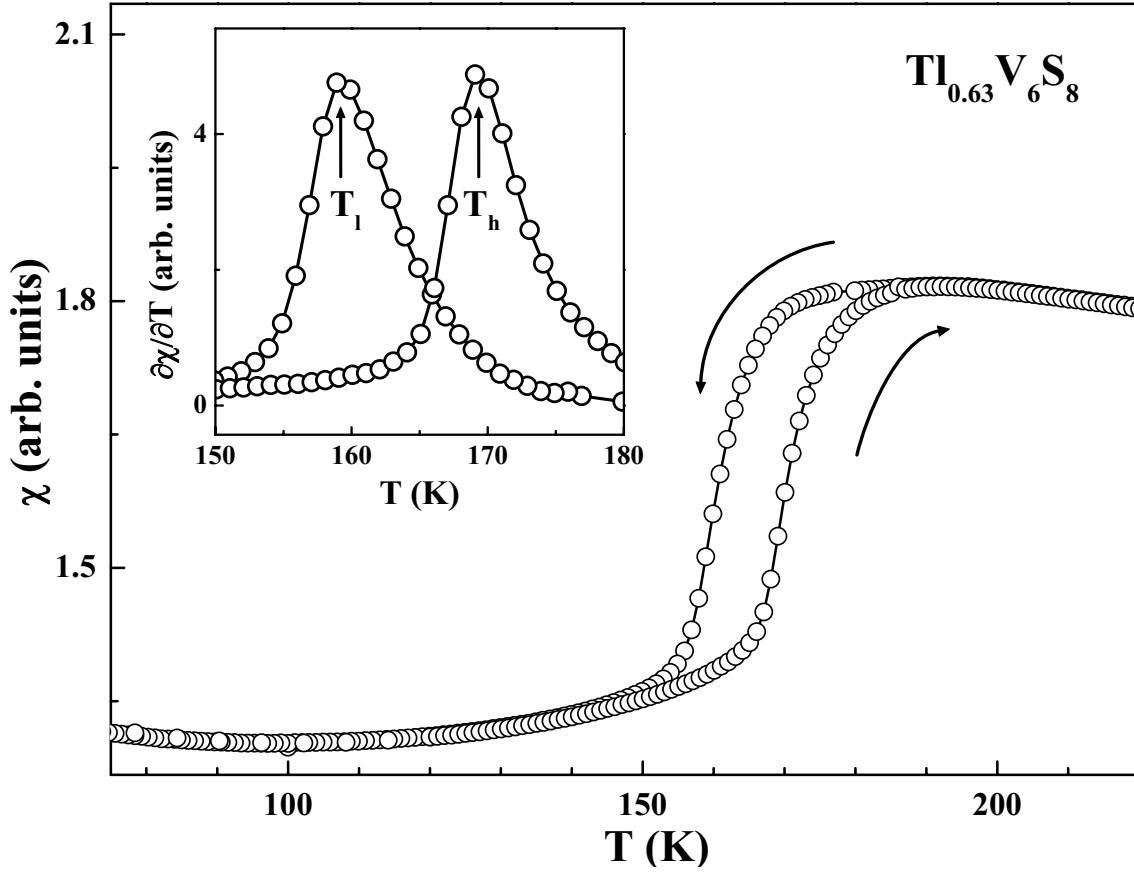
Figure 5.9: $\chi(T)$ for $Tl_{0.63}V_6S_8$. A significant jump in $\chi(T)$ is observed upon cooling $(T \approx T_l)$ and warming $(T \approx T_h)$. Inset: T_l and T_h defined as local maxima in $\partial\chi(T)/\partial T$ upon cooling and warming, respectively.

ues are the same as those found in the resistivity measurements: $T_l = 158$ K and $T_h = 169$ K.

The high temperature dependence of the susceptibility follows a Curie-Weiss law, above T_l. The saturation seen below $T \approx 140$ K can be regarded as an indication for Pauli paramagnetism. The drop in the susceptibility below $T = T_l$ is about 28% for the $Tl_{0.63}V_6S_8$ sample. This indicates an important reduction in the density of states at the Fermi-level as the susceptibility is given by:

$$\chi_{Pauli} = \mu_B^2 N(E_F)\frac{N_A}{M} \quad [192],\tag{5.1}$$

where μ_B is the Bohr magneton, $N(E_F)$ is the density of states at the Fermi-level E_F, N_A is the Avogadro number and M is the molar mass. Therefore, the density of states reduces by roughly 30% upon opening the CDW gap at T_l. The effective
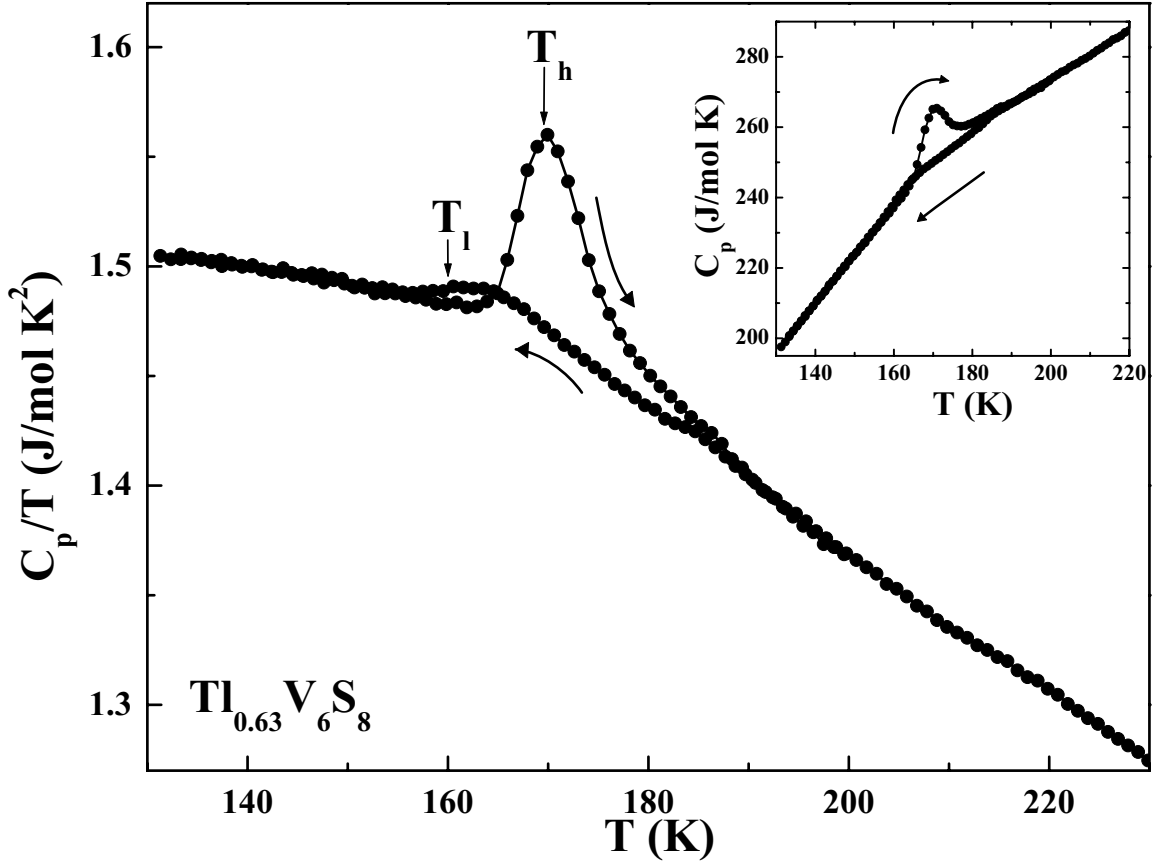
Figure 5.10: The $C(T)/T$ dependency for $Tl_{0.63}V_6S_8$ shows a clear signature of the high-T anomaly. Inset: $C(T)$ for the same Tl content.

reduction obtained from equation 5.1 is

$$\Delta N(E_F) \approx 0.83 \times 10^{17} \text{ states/(J molecule)}. \tag{5.2}$$

Moreover, the high temperature anomaly is detected also in the specific heat measurements. The results obtained for $x = 0.63$ are presented in Fig. 5.10. Similar results, not shown here, are found for the $x = 0.47$ sample. The T_l and T_h temperatures, determined from the resistivity and as well from the susceptibility measurements, are depicted by arrows in Fig. 5.10. T_h corresponds well to the temperature of the maximum in C/T upon warming up, while T_l is placed at slightly lower T than the corresponding cooling down maximum in C/T situated at $T = 161$ K. However, in the latter case the anomaly in specific heat is much broader. The height of the anomaly at $T = T_h$ is strongly enhanced compared to the one at $T = T_l$ and the shape
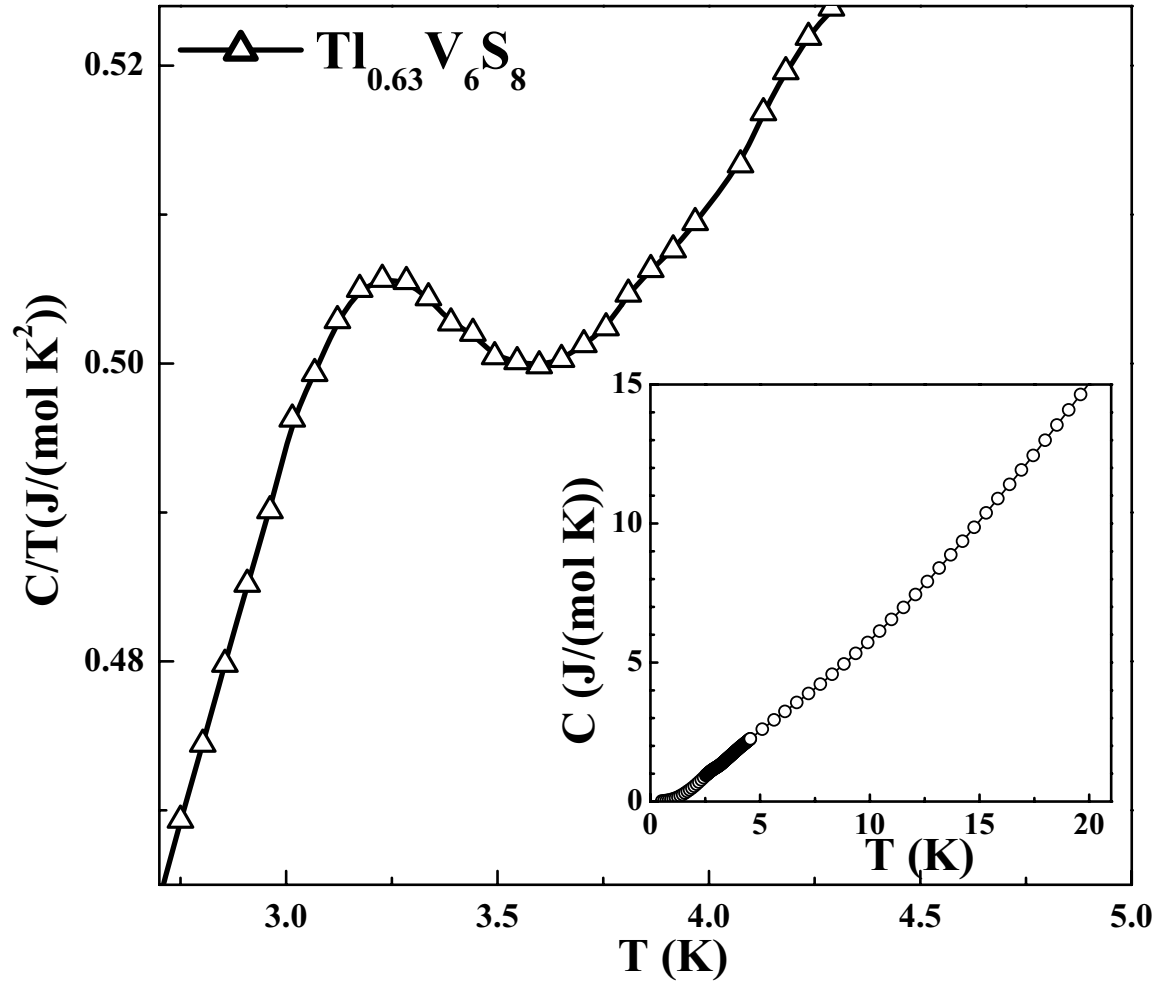
Figure 5.11: The low temperature $C(T)/T$ dependency in $Tl_{0.63}V_6S_8$ revealing the superconducting phase transition. Inset: $C(T)$ for the same sample.

of the anomaly becomes reminiscent of a first-order phase transition upon warming up. The jump in the specific heat at T_h is

$$\Delta C \approx 15 \text{ J/(mol K)}. \tag{5.3}$$

Furthermore we were able to probe the superconducting state employing a specific heat measurement. It is natural that the occurrence of two gaps on the Fermi-surface, one superconducting and the other dielectric, will change the thermodynamic properties of a CDW superconductor compared to the conventional BCS ones. In the case of CDW superconductors the formation of electron-hole pairs leads to $\Delta(0)/(k_BT_c)$ always smaller than the BCS value of 1.76, where $\Delta(0)$ and T_c are the

superconducting energy gap and the SC transition temperature, respectively [193]. The T-dependence of the specific heat for a CDW superconductor is also influenced by the high temperature gap [194, 195]. The specific heat jump at T_c is reduced relative to the BCS relation by a main correction quadratic in T_c/Δ_{CDW}, where Δ_{CDW} is the charge-density wave gap [193]. Cases of CDW superconductors for which the heat capacity reveals no anomaly as the SC state sets in, are not rare. For example the ceramic $BaPb_{1-x}Bi_x O_3$ with $x = 0.25$ reveals no signature of SC in calorimetric measurements [196] but a partial removal of the CDW gapping in this compound results in the appearance of a jump in the specific heat at T_c [197, 198]. $\Delta C/(\gamma T_c)$ ratios considerably lower than the correspondent BCS value of 1.43 are found for a vast series of CDW superconductors: $Li_{1.16}Ti_{1.84}O_4$ ($\Delta C/(\gamma T_c) \approx 0.6$) [199], $Nb_3 S_4$ ($\Delta C/(\gamma T_c) \approx 1.11$) [200], $Nb_3 Se_4$ ($\Delta C/(\gamma T_c) \approx 0.66$) [200], $Nb_3 Te_4$ (no trace of SC in specific heat) [200], etc..

Our specific heat study on $Tl_{0.63}V_6 S_8$ reveals unambiguously an anomaly as the system enters from the normal, but partially gapped state, into the superconducting phase (Fig. 5.11). The SC transition temperature $T_c = 3.39$ K determined using an equal-area construction, corresponds to the onset of the resistivity drop observed at T_c. The transition width is $\Delta T \approx 0.3$ K and the magnitude of the normalized jump $\Delta C/(\gamma T_c)$ estimated also using the equal-area construction has a small value of only

$$\Delta C/(\gamma T_c) \approx 0.08. \tag{5.4}$$

However, as already mentioned above, finding such a reduced $\Delta C/(\gamma T_c)$ is not surprising for a CDW superconductor.

In the normal state, the specific heat is almost linear in temperature up to $T = 12$ K (inset Fig. 5.11). Assuming for the low-T normal state

$$C = \gamma T + \beta T^3, \tag{5.5}$$

C/T is plotted as function of T^2 in order to estimate the specific heat electronic (γ) and phononic (β) terms (Fig. 5.12). The dashed line represents the least-squares fit to the normal state data which yields:
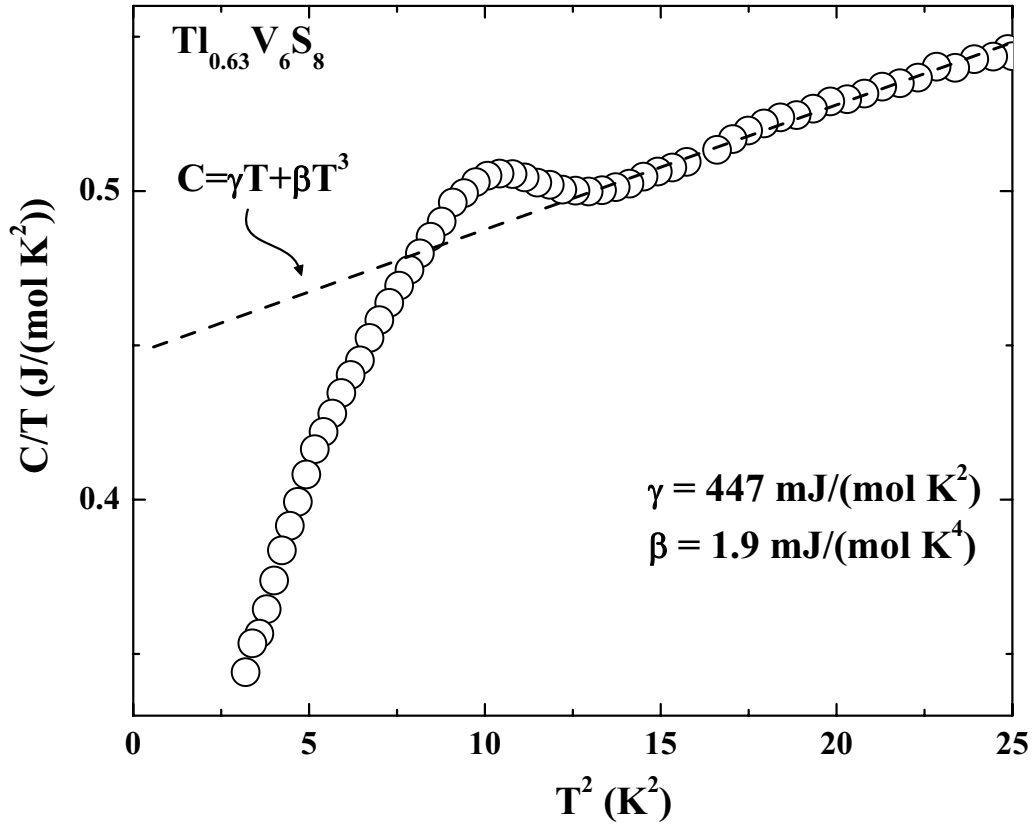
Figure 5.12: C/T as function of T^2. A linear fit (dashed line) in the normal state yields the $\gamma = 447$ mJ/(mol K^2) and $\beta = 1.9$ mJ/(mol K^4).

$$\gamma = 447 \text{ mJ/(mol K}^2\text{)},$$

$$\beta = 1.9 \text{ mJ/(mol K}^4\text{)}.$$

The Debye temperature Θ_D is given by:

$$\Theta_D = \sqrt[3]{\frac{12\pi^4 nR}{5\beta}}, \tag{5.6}$$

where R is the general gas constant and n is the number of atoms per molecule. This expression gives $\Theta_D = 246$ K, using $n = 14.63$ for $Tl_{0.63}V_6S_8$ and our experimental value of β.

The electron-phonon coupling constant, λ, can be evaluated using the McMillan expression [201]:

$$T_c = \frac{\Theta_D}{1.45} \exp\left[-\frac{1.04(1+\lambda)}{\lambda - \mu^*(1 + 0.62\lambda)}\right], \tag{5.7}$$

where μ^* denotes the Coulomb repulsion between electrons. An accurate value of μ^* is difficult to obtain. For simple elements it might be determined from the isotope shift. However, it was argued by McMillan that μ^* ranges from $\mu^* = 0.1$ for nearly free electron metals to $\mu^* = 0.13$ for transitional metals [201]. Using this latter value in equation 5.7 with $T_c = 3.39$ K, and the experimental $\Theta_D = 246$ K we obtain $\lambda = 0.61$. This is very close to the value of $\lambda = 0.61$ estimated for the metallic V [201].

The Sommerfeld coefficient γ is related to the electronic density of states at the Fermi-level $N(E_F)$ by:

$$\gamma = \frac{2}{3}\pi^2 k_B^2 (1 + \lambda) N_A N(E_F).\qquad(5.8)$$

This gives $N(E_F) = 5.9 \times 10^{20}$ states/(J molecule).

Table 5.2: Thermodynamic properties obtained from the specific heat measurements for $Tl_{0.63}V_6S_8$.

T_c (K)	3.39
$\frac{\Delta C}{\gamma T_c}$	0.08
γ (mJ/(mol K^2))	447
β (mJ/(mol K^4))	1.9
Θ_D (K)	246
λ	0.61
$N(E_F)$ (states/J molecule)	5.9×10^{20}
$\langle a^2 \rangle$	0.24
$\frac{\bar{\Delta}_0}{k_B T_c}$	1.14

Little is known about the symmetry of the gap. However, the low-dimensional structure and the anisotropic gap found in the related compounds Nb_3S_4 [202] and Nb_3Se_4 [200] suggest that the gap might be anisotropic in $Tl_xV_6S_8$ as well. When the symmetry of the energy gap is reduced, the thermal selection allows, at low-T, that the states corresponding to the regions on the Fermi-surface with a smaller gap

to contribute to the electronic specific heat. The effect of the anisotropy on the thermodynamic properties of superconductors has been analyzed by J. R. Clem [203] who has suggested the following modifications to the BCS predictions:

$$\frac{\bar{\Delta}_0}{k_B T_c} = 1.764 \left(1 - \frac{3}{2}\langle a^2\rangle\right),$$

(5.9)

$$\frac{\Delta C}{\gamma T_c} = 1.426 \left(1 - 4\langle a^2\rangle\right),$$

(5.10)

where $\bar{\Delta}_0$ is the averaged energy gap at $T = 0$ K and the mean-squared anisotropy $\langle a^2\rangle$ is the average over the whole Fermi-surface of the square of the energy gap deviation from its average value. From equation 5.10 we obtain $\langle a^2\rangle = 0.24$, significantly higher than $\langle a^2\rangle = 0.07$ for Nb_3S_4 [200], $\langle a^2\rangle = 0.14$ for Nb_3Se_4 [200] or $\langle a^2\rangle = 0.04$ for the layered compound $2H$-$NbSe_2$ [204]. With increasing lattice anisotropy, the $\langle a^2\rangle$ value is enhanced. Therefore, the high value we found might be due to the pronounced one dimensional character of the electronic structure of $Tl_x V_6 S_8$. Replacing $\langle a^2\rangle$ in equation 5.9 we estimate an normalized average energy gap of

$$\frac{\bar{\Delta}_0}{k_B T_c} = 1.14$$

(5.11)

for $Tl_{0.63} V_6 S_8$, smaller than the 1.76 value expected for a BCS superconductor. The results obtained from the low temperature specific heat measurements for $Tl_{0.63} V_6 S_8$ are summarized in the Table 5.2. Our results suggest that this compound is a highly anisotropic and weak coupling superconductor.

5.2.3 Influence of pressure on the charge-density wave instability and on the superconductivity

It is of great importance to determine in which way the superconductivity and the charge-density wave instability interfere with each other. Pressure, in general, has an important effect on the CDW state being an ideal tool to explore the interplay between the two ground states. In the following we will concentrate on the study of resistivity under hydrostatic pressure for the $Tl_{0.63}V_6S_8$ compound which displays both, CDW and complete SC. The results obtained for $x = 0.15$ and $x = 0.47$ under pressure are only mentioned briefly.

Upon applying hydrostatic pressure, the size of the CDW anomaly is gradually reduced together with a decrease of T_l and T_h (Fig. 5.13). The hysteretic behavior in
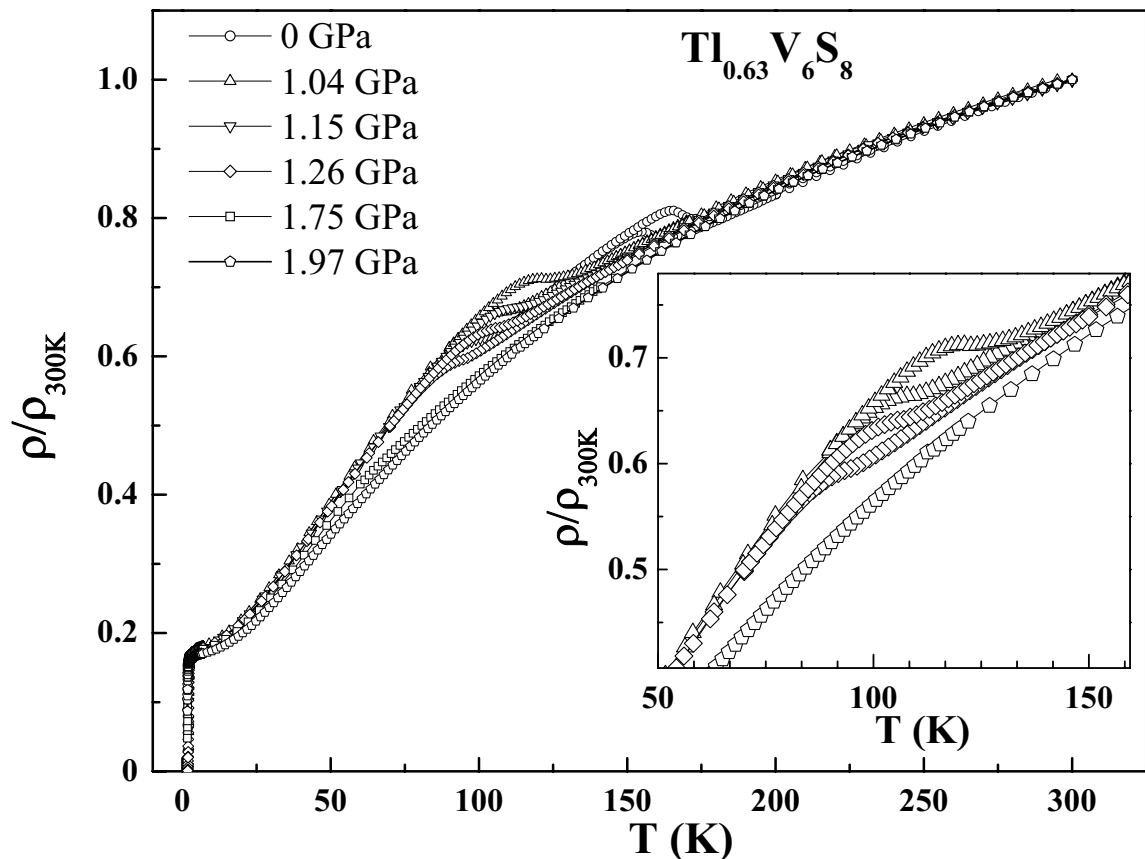
Figure 5.13: Temperature dependence of the normalized resistivity at different pressures for $Tl_{0.63}V_6S_8$. The size of the CDW anomaly as well as the transition temperature decreases with increasing pressure and is finally completely suppressed.
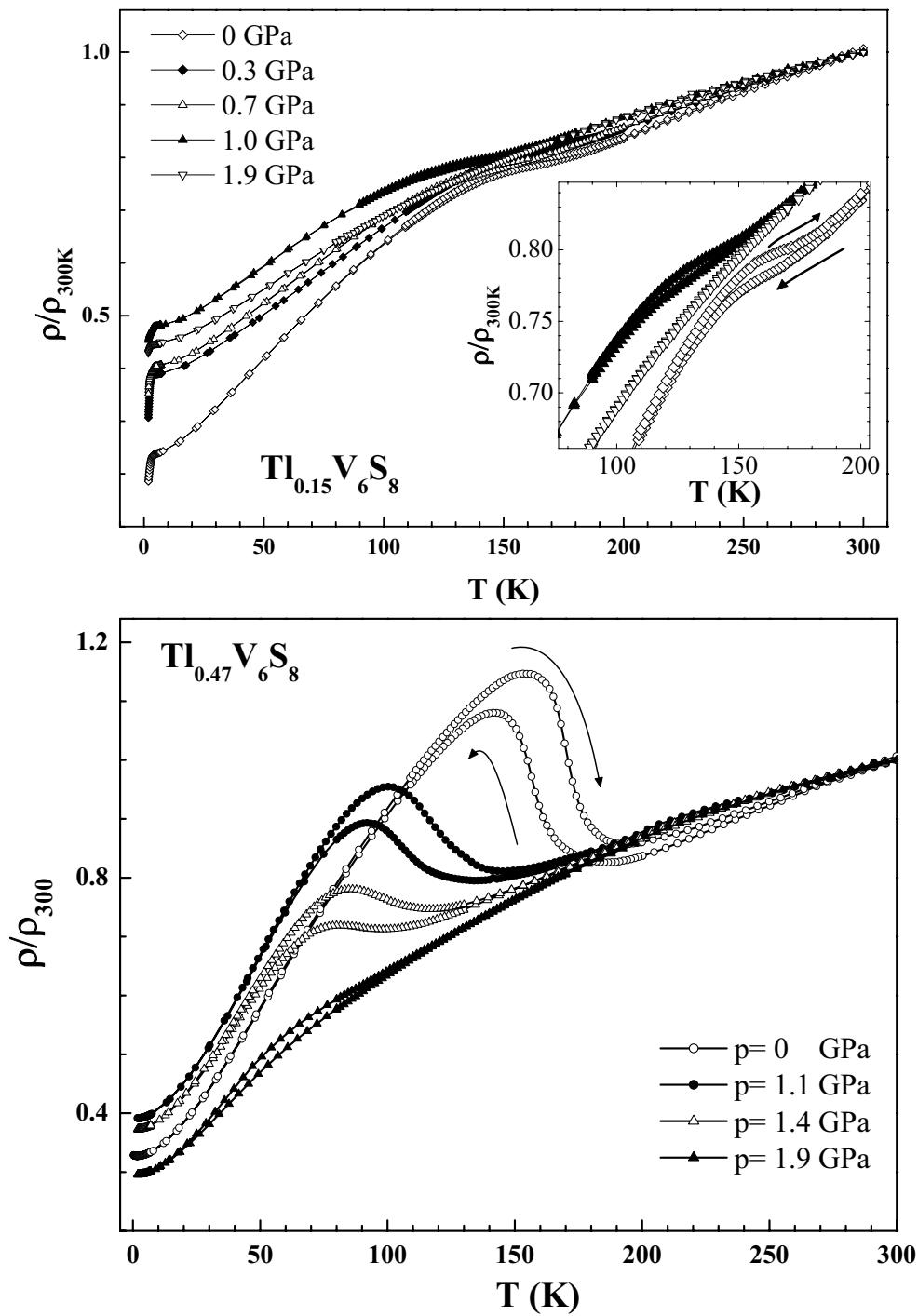
Figure 5.14: Temperature dependence of the normalized resistivity at different pressures for $Tl_xV_6S_8$ (top: $x = 0.15$; bottom: $x = 0.47$). The size as well as the transition temperature decreases with increasing p and is finally completely suppressed for $x = 0.15$.

resistivity is maintained up to $p = 1.26$ GPa. Above this pressure, which corresponds to a $T_l = 95$ K, any signature of the anomaly upon cooling down is difficult to be resolved unambiguously. However, the anomaly is still visible in the warming up measurements where the CDW formation can be followed up to $p = 1.71$ GPa corresponding to $T_h = 67$ K. For even higher p, no anomaly is found anymore, leading us to the conclusion that the CDW phase transition is suddenly suppressed at elevated p. We estimate a critical pressure for the vanishing of the CDW state of about $p_c = (1.85 \pm 0.12)$ GPa.

A similar suppression of the CDW transition temperature is observed also for $x = 0.15$ and $x = 0.47$ (Fig. 5.14). For $x = 0.15$ the estimated critical pressure is $p_c = (1.7 \pm 0.2)$ GPa, while for the $x = 0.47$ sample the CDW transition is not suppressed up to $p = 1.9$ GPa, the highest pressure achieved in the employed pressure cell.

Only the onset of the superconductivity is observed for $x = 0.15$ and its temperature is only slightly decreasing with pressure. For $x = 0.47$ no signature of superconductivity is observed up to $p = 1.9$ GPa . The absolute values of the resistivity in the low-T range are strongly influenced by the CDW transition temperature for both $x = 0.15$ and $x = 0.47$.

Zero resistivity is observed for the $x = 0.63$ sample at all pressures (Fig. 5.15). Upon increasing p, the superconducting transition is moved to lower temperatures from $T_c = 3.05$ K at atmospheric pressure down to $T_c = 1.09$ K at the maximum achieved pressure $p = 2.5$ GPa. Here, T_c is defined as the temperature where $\rho(T)$ drops to zero. The transition width ($\Delta T_c \approx 0.4$) remains unaffected by pressure. A slight decrease with p can be observed for the resistivity value in the normal state, ρ_0, immediately above the SC transition. Moreover, an additional tiny anomaly, not present at ambient pressure, starts to be visible around $T = 4.5$ K, already under a low pressure of $p = 0.18$ GPa. The temperature where this anomaly occurs decreases then slowly with increasing p (inset Fig. 5.15). The temperature of the anomaly does not correspond to any of the superconducting phase transitions at atmospheric pressure in elemental Tl ($T_c = 2.3$ K [205]) or V ($T_c = 5.3$ K [206, 207]). In addition, no
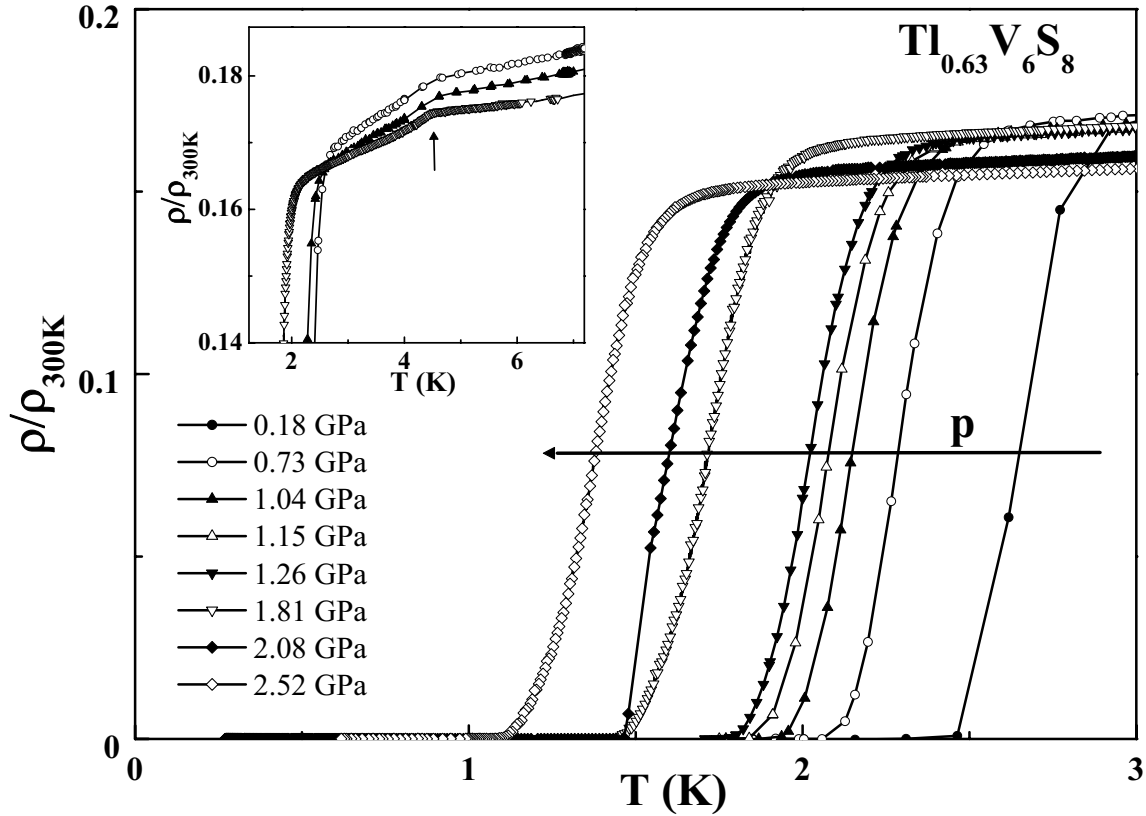
Figure 5.15: The low-T normalized resistivity showing the superconducting transition in $Tl_{0.63}V_6S_8$ at different pressures. Inset: a small anomaly above $T = T_c$, depicted by the arrow is visible under pressure

trace of magnetic order has been revealed by susceptibility measurements at ambient pressure. The nature of this feature remains to be investigated in future studies.

The pressure dependence of T_c, T_l and T_h are depicted for the $Tl_{0.63}V_6S_8$ sample in the phase diagram shown in Fig. 5.16. T_l and T_h are decreasing linearly at low p with an initial slope of

$$\frac{\partial T_l}{\partial p} \approx \frac{\partial T_h}{\partial p} = -44 \text{ K/GPa.} \tag{5.12}$$

The superconducting transition temperature first decreases suddenly from ambient pressure to $p = 0.18$ GPa and then, at higher pressures, is further reduced linearly with a slope

$$\frac{\partial T_c}{\partial p} = -0.6 \text{ K/GPa.} \tag{5.13}$$

Remarkably, the complete suppression of the CDW instability at the estimated critical pressure $p_c = (1.85 \pm 0.12)$ GPa leads to an enhancement of T_c of approximately
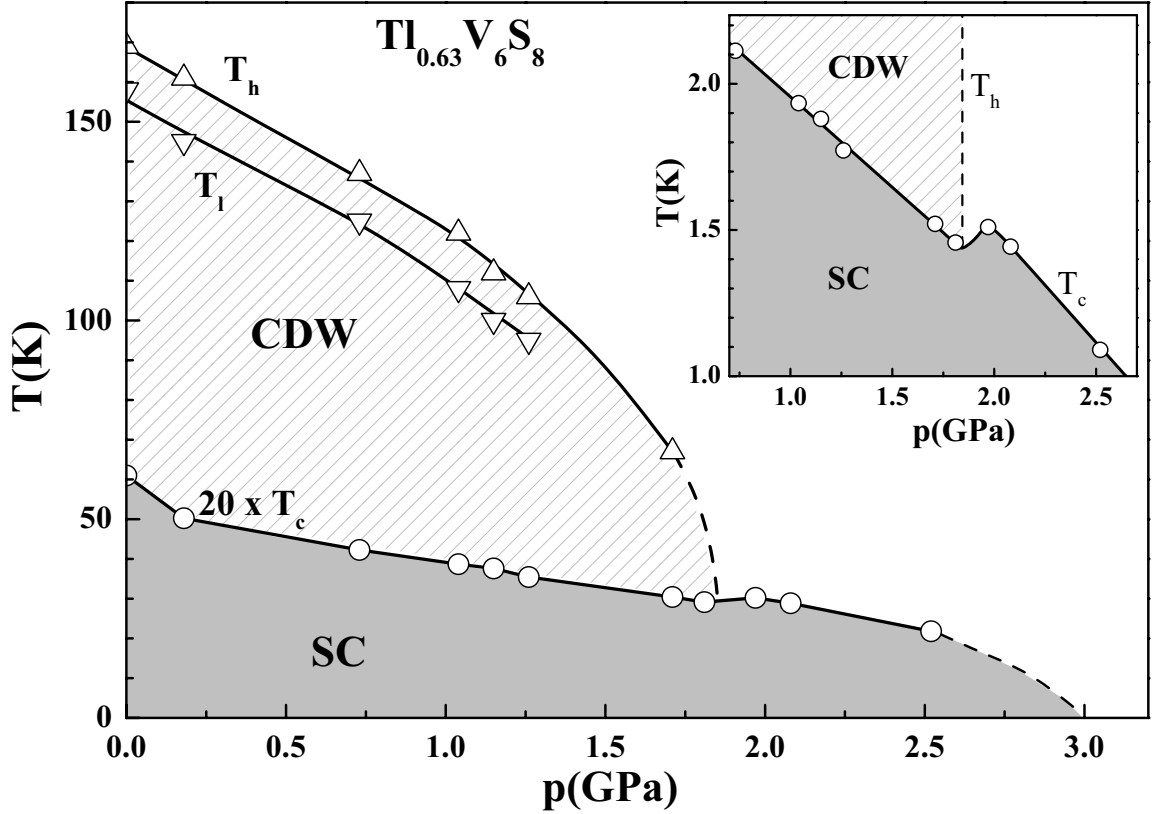
Figure 5.16: Phase diagram for $Tl_{0.63}V_6S_8$. The CDW instability is completely suppressed at a critical pressure $p_c = (1.85 \pm 0.12)$ GPa and concomitantly T_c is enhanced (inset). The dashed lines are guides for the eye.

$T_c|_{p=1.97\ GPa} - T_c|_{p=1.81\ GPa} \approx 120$ mK (inset Fig. 5.16). This is an indication that the relation between CDW and SC gap is antagonistic. However, pressure is strongly detrimental to both of the anomalies therefore the enhancement of T_c at $p \approx p_c$ due to the increase in the density of states is relatively small.

Above $p = 2$ GPa, T_c starts to decrease again, at an accelerated pace:

$$\frac{\partial T_c}{\partial p} = -0.8 \text{ K/GPa}. \tag{5.14}$$

A linear extrapolation of $T_c(p)$ would yield, as zero T interception, a critical pressure of about $p_c^{SC} = 3.9$ GPa. However, most likely the SC will be suppressed at significantly lower pressures ($|\frac{\partial T_c}{\partial p}|$ shows already an increasing tendency), as suggested by the dashed line in Fig. 5.16.

The enhancement of the resistivity at T_l and T_h results from the decrease of the
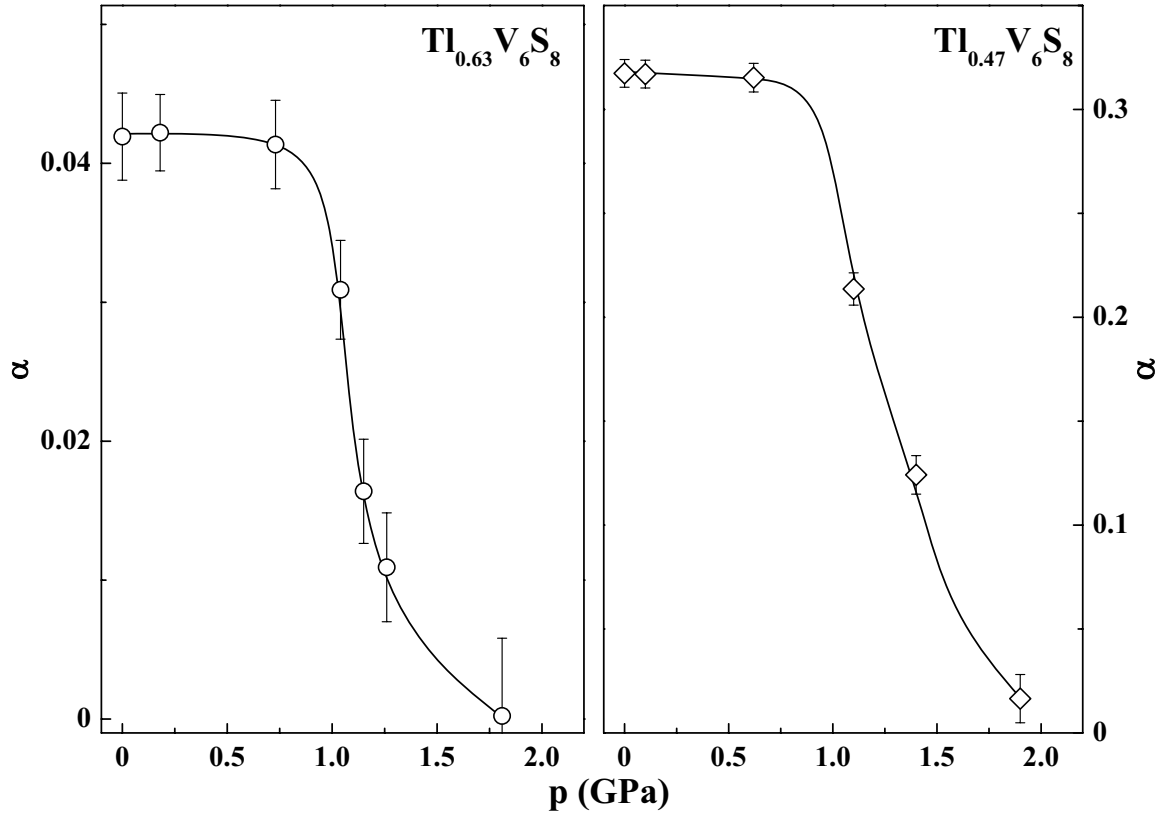
Figure 5.17: $\alpha(p)$ dependence for $Tl_{0.63}V_6S_8$ and $Tl_{0.47}V_6S_8$ samples. For both compounds, $\alpha(p)$ is almost constant at low pressure but decreases abruptly above $p \approx 0.9$ GPa.

carrier density as the CDW gap opens at the Fermi-level. The size of the relative resistivity increase can be defined as:

$$\alpha = \frac{\rho_{CDW} - \rho_n}{\rho_{CDW}} = \frac{\sigma_n - \sigma_{CDW}}{\sigma_{CDW}}, \tag{5.15}$$

where ρ_{CDW} is the resistivity value on top of the CDW anomaly while ρ_n is the resistivity value expected at the transition temperature in the absence of the CDW formation. ρ_n is determined by extrapolating the high-T $\rho(T)$ curve down to the CDW transition temperature. σ_{CDW} and σ_n are the conductivities corresponding to ρ_{CDW} and ρ_n, respectively. In a metal the conductivity is in general given by

$$\sigma \sim N(E_F)e^2 v_F \tau, \tag{5.16}$$

where $N(E_F)$ is the density of states at the Fermi-level and v_F and τ are the Fermi velocity and the relaxation time of the conduction electrons, respectively.

If we assume that the opening of the CDW gap reduces $N(E_F)$ without changing v_F and τ the relation 5.15 can be rewritten as:

$$\alpha = \frac{N_n - (N_n - \Delta N)}{N_n} = \frac{\Delta N}{N_n},$$ (5.17)

where N_n is the density of states at the Fermi-surface in the absence of the CDW instability and ΔN denotes its reduction after the gap has been opened. Therefore the fractional increase in the resistance, α, would give information regarding the size of the gapped area of the Fermi-surface [208, 209].

The pressure dependences of α for $x = 0.63$ and $x = 0.47$ are shown in Fig. 5.17. α is almost pressure independent for both compounds up to $p \approx 0.9$ GPa, but decreases abruptly above this pressure. The effect of the inter-chain coupling (η) on the CDW transition temperature has been studied theoretically within the mean-field approximation by Horovitz *et al.* [55, 210]. They showed that for a given electron-phonon coupling constant, λ, T_{CDW}/T_F is almost independent of the inter-chain coupling for η below a critical value η_c. Nevertheless, above η_c, T_{CDW}/T_F is suddenly reduced to zero due to a collapse of the nesting of the Fermi-surface. Within this scenario the drastic reduction of α only above $p \approx 0.9$ GPa might be a consequence of the inter-chain coupling constant exceeding η_c and thereby rapidly suppressing the CDW gap. A similar pressure dependence of $\alpha(p)$ has been reported for $NbSe_3$ [211, 212] and explained within the frame of the theory elaborated by Horovitz *et al.* [55, 210].

The CDW transition temperature depends also on the electron-phonon coupling constant:

$$T_{CDW} = 5.43 \, T_F \, \exp\left(-\frac{1}{\lambda}\right) \quad [210],$$ (5.18)

where T_F is the Fermi temperature. The pressure hardening of the bare phonon spectrum tends to decrease the electron-phonon coupling and, therefore, renders the lattice distortion less favorable energetically, resulting in a lowering of T_{CDW} as suggested by equation 5.18.

5.3   Conclusions

The high temperature anomaly observed in the metallic $Tl_xV_6S_8$ has been attributed to a charge-density wave instability [184]. Its true CDW nature is corroborated by band structure calculations which reveal nesting conditions [187]. To the best of our knowledge the first-order character of the high temperature anomaly in $Tl_xV_6S_8$ suggested in Ref. [184, 186] is confirmed for the first time by the observation of a hysteresis in our resistivity and susceptibility measurements.

Moreover, we report on the first specific heat evidence of the existence of the CDW ($Tl_{0.47}V_6S_8$ and $Tl_{0.63}V_6S_8$) and SC transitions ($Tl_{0.63}V_6S_8$) in the $Tl_xV_6S_8$ family. A clear hysteresis is as well observed at the high temperature transition in the specific heat data.

We observed a strong corespondence of the physical properties of $Tl_xV_6S_8$ on the Tl concentration x. Each sample showed a clear CDW anomaly which is strongly enhanced at half Tl filling, $x = 0.47$. This is also the only composition for which no signature of superconductivity is observed. The specific heat probing the SC phase in $Tl_{0.63}V_6S_8$ suggests that this compound is a highly anisotropic, weak coupling superconductor.

A first-ever study of resistivity under pressure revealed a rapid suppression of T_{CDW} upon increasing p for all samples investigated. For $x = 0.63$ also the evolution of the SC transition with p was followed by resistivity. Pressure is detrimental also to the SC phase as T_c is reduced with increasing p. Nevertheless, as the CDW gap is closed at the critical pressure p_c, the increase in the density of stated leads to a clear enhancement of T_c suggesting that SC and CDW compete for parts of the Fermi-surface.

Future systematic studies, on single crystals of $Tl_xV_6S_8$ under pressure in magnetic field will shed more light on the physical properties in this already very interesting, quasi one-dimensional class of materials.

Chapter 6

Conclusions

In the present work we explored the FFLO state in CeCoIn$_5$, the effect of uniaxial stress on the superconducting order parameter symmetry of the cubic UBe$_{13}$ and the interplay between superconductivity and a charge-density wave instability in the low-dimensional metal Tl$_x$V$_6$S$_8$.

We have studied the pressure evolution of the superconducting $B - T$ phase diagram of CeCoIn$_5$ by specific heat measurements. The superconducting transition temperature is enhanced from $T_c = 2.24$ K at atmospheric pressure to $T_c = 2.58$ K at the maximum pressure achieved, $p = 1.34$ GPa. The significant anisotropy in the system present already at ambient pressure, is further enhanced upon increasing p. For a magnetic field $B \parallel (a, b)$, the upper critical field rises from $B_{c2}(0)|_{0 \text{ GPa}} = 11.6$ T to $B_{c2}(0)|_{1.34 \text{ GPa}} = 14.3$ T, while for $B \parallel c$, $B_{c2}(0)$ is reduced from $B_{c2}(0)|_{0 \text{ GPa}} = 4.9$ T to $B_{c2}(0)|_{1.34 \text{ GPa}} = 4.2$ T. It is important to remark that in the $B \parallel c$ case upon applying pressure the upper critical field is suppressed while simultaneously T_c is enhanced; this behavior remains a challenge to understand.

The prerequisites required for the realization of the FFLO state satisfied at ambient pressure in CeCoIn$_5$ are met under pressure as well: the system remains in the clean-limit, with ℓ_{tr}/ξ_0 even increasing under pressure and the Maki parameter α stays well above the minimum required value for the formation of the FFLO state. The first-order character of the SC phase transition at high magnetic fields for $T_c < T_0$ is maintained also under pressure. This underlines the fact that the Pauli paramagnetism remains the main pair-breaking mechanism. T_0 is steadily increasing

upon applying pressure from $T_0(0\text{ GPa}) = 0.875$ K to $T_0(1.34\text{ GPa}) = 1.170$ K.

Furthermore, for all investigated pressures, the FFLO anomaly can be followed as function of magnetic field. With increasing p, the FFLO region in the phase diagram expands to higher temperatures and higher fields indicating that the FFLO state becomes more robust upon reducing the antiferromagnetic fluctuations, as expected in the frame of the AFM-fluctuations based model proposed in [47]. Our result provides the first evidence of the existence of this state away from the influence of the strong magnetic fluctuations, clearly suggesting its true FFLO nature.

We have analyzed the $B_{c2}(T)$ data of CeCoIn$_5$, at different pressures, within the microscopic model developed in Ref. [45, 46] which includes:

a) the layered structure ;

b) $d_{x^2-y^2}$ symmetry for the SC order parameter;

c) the Gruenberg-Gunther ansatz.

This model gives an excellent description of the experimental $B_{c2}(T)$ curves for both field orientations. Pronounced changes above $p = 0.45$ GPa are observed for both g-factor and the Fermi velocity in the basal plane (a, b).

In the heavy-fermion superconductor UBe$_{13}$ the uniaxial stress along the crystallographic [100] direction reduces the lattice symmetry from cubic to tetragonal. For both "L"- and "H"-type single crystals the superconducting transition temperature as function of uniaxial stress was probed by AC specific heat measurements. In both cases T_c is found to be reduced continuously upon increasing the uniaxial deformation. The superconducting anomaly becomes broader only at the top and a tiny feature, suggesting a splitting of T_c, is induced at high pressures in both types of samples. This anomaly is more clearly visible in the "H"-type sample where higher pressures were achieved. However, the effect is very small (≈ 0.01 K/GPa) compared to the theoretical estimation (≈ 0.5 K/GPa). Despite these observation, no unambiguous double structure could be detected in the "L"-type sample within our

measurement. Also the tiny splitting of T_c in the "H"-type crystal has to be regarded with caution; a pressure anisotropy effect, though improbable for the given sample geometry, cannot be completely ruled out. A lack of splitting could imply that:

a) the induced strain is still too small;

b) the order parameter is single component rather than multi-component;

c) depending on the details of the free energy, fourth-order cross-terms may pin the order parameter at the higher temperature phase transition [11, 12], preventing the other one even for a multi-component order parameter.

The metallic, quasi-1D compound $T_xV_6S_8$ displays both superconductivity and a high-T anomaly ascribed to the formation of a charge-density wave [184]. The CDW nature of this anomaly is corroborated by band structure calculations [187]. We studied the interplay between these two ground states in this compound employing resistivity (at both, ambient and high pressure), specific heat and susceptibility measurements. To our knowledge the first-order character of the high temperature anomaly in $Tl_xV_6S_8$ suggested in Ref. [184, 186] is confirmed for the first time by the observation of a hysteresis in our resistivity and susceptibility measurements.

In addition, we observed for the first time in this compound the CDW and SC transition in specific heat measurements. Also here the CDW transition displays a clear thermal hysteresis. We observed a clear dependence of the physical properties of $Tl_xV_6S_8$ on the Tl concentration x. The CDW anomaly is present in all investigated samples being strongly enhanced at half Tl filling, $x = 0.47$. This is also the only composition for which no signature of superconductivity is observed. The specific heat results regarding the SC phase in $Tl_{0.63}V_6S_8$ suggest that this compound is a highly anisotropic, weak coupling superconductor.

A first-time resistivity study under pressure revealed a rapid suppression of T_{CDW} upon increasing p for all concentrations investigated ($x = 0.15$, $x = 0.47$ and $x = 0.63$). Also the pressure evolution of the SC transition was followed by resistivity

measurements for $x = 0.63$. Pressure is detrimental also to the superconductivity as the SC transition temperature, T_c, is reduced with increasing p. Nevertheless, as the CDW gap is closed at the critical pressure p_c, the increase in the density of states leads to a clear enhancement of T_c suggesting that SC and CDW compete for the same parts of the Fermi-surface.

Appendix:

AC specific heat under uniaxial stress in CeCoIn$_5$

We measured the AC specific heat under uniaxial stress on high quality single crystals of CeCoIn$_5$. The crystals grow in a plate-like geometry with the small side along the crystallographic c-axis. The typical sample thickness is only 0.1 mm to 0.3 mm. Therefore, the samples easily brake under uniaxial stress applied in the (a, b)-plane. In order to prepare a mechanically stable setup we embedded the sample in a soft epoxy after attaching, on both of its large faces, silver foils used for the thermal contacts to the heater and thermometer, respectively. Under pressure the epoxy is deformed plastically and we assumed that all the force applied is kept by the sample. Therefore, the estimated maximum uniaxial pressure applied along the a-axis is about $p_a = 0.7$ GPa. The results obtained are depicted in Fig. 6.1.

The superconducting transition T_c is gradually moved to higher temperatures upon increasing pressure with an initial slope

$$\left. \frac{\partial T_c}{\partial p_a} \right|_{p_a = 0 \text{ GPa}} = (0.305 \pm 0.010) \text{ K/GPa}. \tag{6.1}$$

T_c seems to approach a broad maximum around $p_a = 0.7$ GPa, the highest pressure achieved. The relative jump in the specific heat is decreasing drastically under a small uniaxial stress and tends to saturate above $p_a \geq 0.3$ GPa.
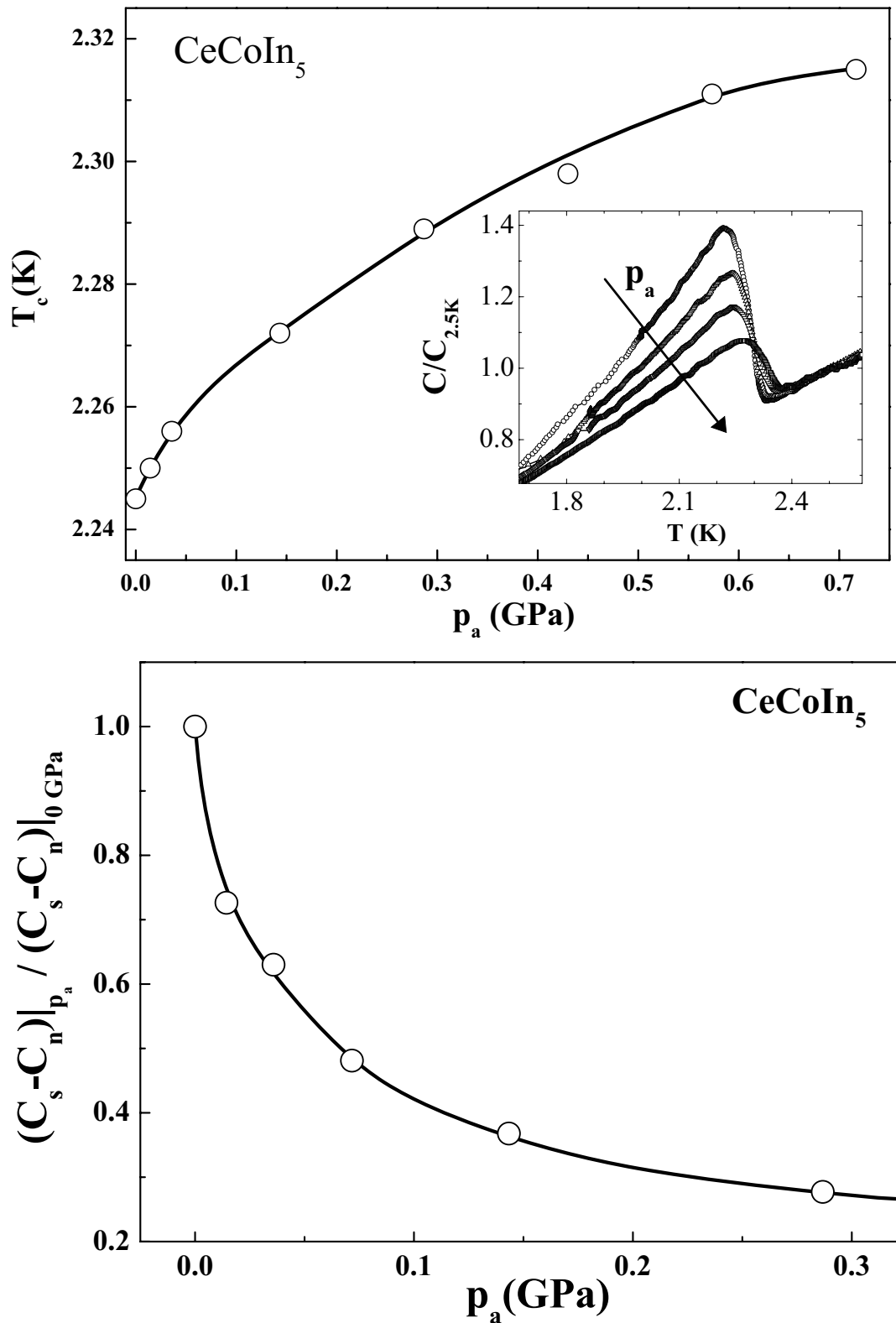
Figure 6.1: Upper panel: $T_c(p_a)$. Inset, upper panel: Temperature dependence of the specific heat normalized to $C(2.5\text{K})$ at different pressures. Lower panel: Pressure dependence of the normalized specific heat jump.

Bibliography

[1] C. Petrovic, P. G. Pagliuso, M. F. Hundley, R. Movshovich, J. L. Sarrao, J. D. Thompson, Z. Fisk, and P. Monthoux, J. Phys.: Condens. Matter **13**, L337 (2001).

[2] J. D. Thompson, M. Nicklas, A. Bianchi, R. Movshovich, A. Llobet, W. Bao, A. Malinowski, M. F. Hundley, N. O. Moreno, P. G. Pagliuso, J. L. Sarrao, S. Nakatsuji, Z. Fisk, R. Borth, E. Lengyel, N. Oeschler, G. Sparn, and F. Steglich, Physica B **329-333**, 446 (2003).

[3] A. Bianchi, R. Movshovich, C. Capan, P. G. Pagliuso, and J. L. Sarrao, Phys. Rev. Lett. **91**, 187004 (2003).

[4] H. A. Radovan, N. A. Fortune, T. P. Murphy, S. T. Hannahs, E. C. Palm, S. W. Tozer, and D. Hall, Nature **425**, 51 (2003).

[5] P. Fulde and R. A. Ferell, Phys. Rev. **135**, A550 (1964).

[6] A. I. Larkin and Y. N. Ovchinnikov, Pis'ma Zh. Eksp. Teor. Fiz. **47**, 1136 (1964), [Sov. Phys. JETP **20**, 762 (1965)].

[7] R. Casalbuoni and G. Nardulli, Rev. Mod. Phys. **76**, 263 (2004).

[8] B. Golding, D. J. Bishop, B. Batlogg, W. H. Haemmerle, Z. Fisk, J. L. Smith, and H. R. Ott, Phys. Rev. Lett. **55**, 2479 (1985).

[9] V. Müller, D. Maurer, E. W. Scheidt, C. Roth, K. L. Bucher, and H. E. Bömmel, Solid State Commun. **57**, 319 (1986).

[10] M. Sigrist and K. Ueda, Rev. Mod. Phys. **63**, 239 (1991).

[11] M. Sigrist, R. Joynt, and T. M. Rice, Europhys. Lett. **3**, 629 (1987).

[12] M. Sigrist, R. Joynt, and T. M. Rice, Phys. Rev. B **36**, 5186 (1987).

[13] A. M. Clogston, Phys. Rev. Lett. **6**, 9 (1962).

[14] B. S. Chandrasekhar, Appl. Phys. Lett. **1**, 7 (1962).

[15] G. Sarma, J. Phys. Chem. Solids **24**, 1029 (1963).

[16] K. Maki and T. Tsuneto, Prog. Theo. Phys. **31**, 945 (1964).

[17] H. Suhl, Low Temperature Physics, Les Houches, Gordon and Breach Publishers, Inc., New York, page 235 (1961).

[18] J. Goldstone, Nouvo Cimento **19**, 154 (1961).

[19] J. Goldstone, A. Salam, and S. Weinberg, Phys. Rev **127**, 965 (1962).

[20] M. Tachiki, S. Takahashi, P. Gegenwart, M. Weiden, M. Lang, C. Geibel, F. Steglich, R. Modler, C. Paulsen, and Y. Ōnuki, Z. Phys. B **100**, 369 (1996).

[21] L. G. Aslamazov, Pis'ma Zh. Eksp. Teor. Fiz. **55**, 1477 (1968), [Sov. Phys. JETP **28**, 773 (1969)].

[22] H. Burkhardt and D. Rainer, Ann. Phys. **3**, 181 (1994).

[23] H. Shimahara, J. Phys. Soc. Jpn. **67**, 736 (1998).

[24] R. Combescot and C. Mora, Eur. Phys. J. B **44**, 189 (2005).

[25] S. Matsuo, S. Higashitani, Y. Nagato, and K. Nagai, J. Phys. Soc. Jpn. **67**, 280 (1998).

[26] M. Houzet, Y. Meurdesoif, O. Coste, and A. I. Buzdin, Physica C **316**, 89 (1999).

[27] R. Combescot and C. Mora, Eur. Phys. J. B **28**, 397 (2002).

[28] R. Combescot and C. Mora, Europhys. Lett. **68**, 79 (2004).

[29] C. Mora and R. Combescot, Phys. Rev. B **71**, 214504 (2005).

[30] R. Combescot and C. Mora, Phys. Rev. B **71**, 144517 (2005).

[31] M. Houzet and A. Buzdin, Phys. Rev. B **63**, 184521 (2001).

[32] D. F. Agterberg and K. Yang, J. Phys.: Condens. Matter **13**, 9259 (2001).

[33] N. R. Werthamer, E. Helfand, and P. Hohenberg, Phys. Rev. **147**, 295 (1966).

[34] K. Maki, Phys. Rev. **148**, 362 (1966).

[35] G. Sarma and D. Saint-James, Proceedings of the Conference on the Physics of Type II Superconductivity, Western Reserve University (1964).

[36] L. W. Gruenberg and L. Gunther, Phys. Rev. Lett. **16**, 996 (1966).

[37] K. Maki, Physics **1**, 127 (1964).

[38] R. R. Hake, Appl. Phys. Lett. **10**, 189 (1967).

[39] K. Yang and S. L. Sondhi, Phys. Rev. B **57**, 8566 (1998).

[40] H. Shimahara, Phys. Rev. B **50**, 12760 (1994).

[41] For a review, see: K. Maki in Superconductivity II edited by R. D. Parks, Marcel Dekker, New York, (1969).

[42] K. Gloos, R. Modler, H. Schimanski, C. D. Bredl, C. Geibel, F. Steglich, A. I. Buzdin, N. Sato, and T. Komatsubara, Phys. Rev. Lett. **70**, 501 (1993).

[43] M. A. Baranovn, M. Yu. Kagan, and Yu. Kagan, Pis'ma Zh. Eksp. Teor. Fiz. **64**, 273 (1996), [JETP Lett. **64**, 301 (1996)].

[44] R. Combescot, Europhys. Lett. **55**, 150 (2001).

[45] H. Won and K. Maki, Europhys. Lett. **24**, 452 (1996).

[46] H. Won, K. Maki, S. Haas, N. Oeschler, F. Weickert, and P. Gegenwart, Phys. Rev. B **69**, 180504(R) (2004).

[47] H. Adachi and R. Ikeda, Phys. Rev. B **68**, 184510 (2003).

[48] R. E. Peierls, Quantum Theory of Solids, Oxford University, New York/London, (1955).

[49] G. Grüner, Rev. Mod. Phys. **60**, 1129 (1988).

[50] G. Grüner, Density Waves in Solids, Addison-Wesley, (1994).

[51] M. J. Rice and S. Strässler, Solid State Commun. **13**, 1389 (1973).

[52] H. Fröhlich, Proc. Roy. Soc. London Ser. A **223**, 296 (1954).

[53] J. Sólyom, Adv. Phys. **28**, 201 (1979).

[54] P. A. Lee, T. M. Rice, and P. W. Anderson, Phys. Rev. Lett. **31**, 462 (1973).

[55] B. Horovitz, H. Gutfreund, and M. Weger, Phys. Rev. B **12**, 3174 (1975).

[56] W. L. McMillan, Phys. Rev. B **16**, 643 (1977).

[57] C. M. Varma and A. L. Simons, Phys. Rev. Lett. **51**, 138 (1983).

[58] T. M. Rice and G. K. Scott, Phys. Rev. Lett. **35**, 120 (1975).

[59] I. R. Walker, Rev. Sci. Instrum. **70**, 3402 (1999).

[60] A. Eiling and J. S. Schilling, J. Phys. F: Metal Phys. **11**, 623 (1981).

[61] S. Asgari, E. El-Danaf, S. R. Kalidindi, and R. D. Doherty, Met. Mat. Trans. A **28A**, 1781 (1997).

[62] S. Asgari, E. El-Danaf, E. Shaji, S. R. Kalidindi, and R. D. Doherty, Acta mater. **46**, 5795 (1998).

[63] E. M. Shaji, S. R. Kalidindi, and R. D. Doherty, Mat. Sci. Eng. **A272**, 371 (1999).

[64] E. M. Shaji, S. R. Kalidindi, R. D. Doherty, and A. S. Sedmak, Mat. Sci. Eng. **A340**, 163 (2003).

[65] B. Wand, Dissertation, Technische Hochschule Darmstadt, unpublished (1993).

[66] P. F. Sullivan and G. Seidel, Phys. Rev. **173**, 679 (1968).

[67] Y. M. Kalychak, V. I. Zaremba, V. M. Baranyak, V. A. Bruskov, and P. Y. Zavalii, Russ. Metall. **1**, 213 (1989).

[68] R. Settai, H. Shishido, S. I. Y. Murakawa, M. Nakashima, D. Aoki, Y. Haga, H. Harima, and Y. Ōnuki, J. Phys.: Condens. Matter **13**, L627 (2001).

[69] C. Petrovic, R. Movshovich, M. Jaime, P. G. Pagliuso, M. F. Hundley, J. L. Sarrao, Z. Fisk, and J. D. Thompson, Europhys. Lett. **53**, 354 (2001).

[70] R. A. Fisher, F. Bouquet, N. E. Phillips, M. F. Hundley, P. G. Pagliuso, J. L. Sarrao, Z. Fisk, and J. D. Thompson, Phys. Rev. B **65**, 224509 (2002).

[71] V. S. Zapf, E. J. Freeman, E. D. Bauer, J. Petricka, C. Sirvent, N. A. Frederick, R. P. Dickey, and M. B. Maple, Phys. Rev. B **65**, 014506 (2001).

[72] P. G. Pagliuso, C. Petrovic, R. Movshovich, D. Hall, M. F. Hundley, J. L. Sarrao, J. D. Thompson, and Z. Fisk, Phys. Rev. B **64**, 100503 (2001).

[73] H. Shishido, R. Settai, D. Aoki, S. Ikeda, H. Nakawaki, N. Nakamura, T. Iizuka, Y. Inada, K. Sugiyama, T. Takeuchi, K. Kindo, T. C. Kobayashi, Y. Haga, H. Harima, Y. Aoki, T. Namiki, H. Sato, and Y. Ōnuki, J. Phys. Soc. Jpn. **71**, 162 (2002).

[74] D. Hall, E. C. Palm, T. P. Murphy, S. W. Tozer, Z. Fisk, U. Alver, R. G. Goodrich, J. L. Sarrao, P. G. Pagliuso, and T. Ebihara, Phys. Rev. B **64**, 212508 (2001).

[75] T. Maehira, T. Hotta, K. Ueda, and A. Hasegawa, J. Phys. Soc. Jpn. **72**, 854 (2003).

[76] M. A. Tanatar, J. Paglione, S. Nakatsuji, D. G. Hawthorn, E. Boaknin, R. W. Hill, F. Ronning, M. Sutherland, L. Taillefer, C. Petrovic, P. C. Canfield, and Z. Fisk, Phys. Rev. Lett. **95**, 067002 (2005).

[77] S. Nakatsuji, D. Pines, and Z. Fisk, Phys. Rev. Lett. **92**, 016401 (2004).

[78] N. J. Curro, B. Simovic, P. C. Hammel, P. G. Pagliuso, J. L. Sarrao, J. D. Thompson, and G. B. Martins, Phys. Rev. B **64**, 180514 (2001).

[79] R. Movshovich, M. Jaime, J. D. Thompson, C. Petrovic, Z. Fisk, P. G. Pagliuso, and J. L. Sarrao, Phys. Rev. Lett. **86**, 5152 (2001).

[80] F. A. Fisher, S. Kim, B. F. Woodfield, N. E. Phillips, L. Taillefer, K. Hasselbach, J. Flouquet, A. L. Giorgi, and J. L. Smith, Phys. Rev. Lett. **62**, 1411 (1989).

[81] K. A. Moler, D. J. Baar, J. S. Urbach, R. Liang, W. N. Hardy, and A. Kapitulnik, Phys. Rev. Lett. **73**, 2744 (1994).

[82] N. Momono and M. Ido, Physica C **264**, 311 (1996).

[83] R. Movshovich, A. Bianchi, M. Jaime, M. F. Hundley, J. D. Thompson, N. Curro, P. C. Hammel, Z. Fisk, P. G. Pagliuso, and J. L. Sarrao, Physica B **312-313**, 7 (2002).

[84] Y. Kohori, Y. Yamato, Y. Iwamoto, T. Kohara, E. D. Bauer, M. B. Maple, and J. L. Sarrao, Phys. Rev. B **64**, 134526 (2001).

[85] Y. Kitaoka, K. Ueda, T. Kohara, K. Asayama, Y. Ōnuki, and T. Komatsubara, J. Magn. Magn. Mater. **52**, 341 (1985).

[86] D. E. MacLaughlin, C. Tien, W. G. Clark, M. D. Lan, Z. Fisk, J. L. Smith, and H. R. Ott, Phys. Rev. Lett. **53**, 1833 (1984).

[87] Y. Kohori, T. Kohara, H. Shibai, Y. Oda, Y. Kitaoka, and K. Asayama, J. Phys. Soc. Jpn. **57**, 395 (1988).

[88] K. Matsuda, Y. Kohori, and T. Kohara, Phys. Rev. B **55**, 15223 (1997).

[89] K. Matsuda, Y. Kohori, and T. Kohara, J. Phys. Soc. Jpn. **65**, 679 (1996).

[90] K. Izawa, H. Yamaguchi, Y. Matsuda, H. Shishido, R. Settai, and Y. Ōnuki, Phys. Rev. Lett. **87**, 057002 (2001).

[91] E. E. M. Chia, D. J. V. Harlingen, M. B. Salamon, B. D. Yanoff, I. Bonalde, and J. L. Sarrao, Phys. Rev B **67**, 014527 (2003).

[92] S. Özcan, D. M. Broun, B. Morgan, R. K. W. Haselwimmer, J. L. Sarrao, S. Kamal, C. P. Bidinosti, P. J. Turner, M. Raudsepp, and J. R. Waldram, Europhys. Lett. **62**, 412 (2003).

[93] R. J. Ormeno, A. Sibley, C. E. Gough, S. Sebastian, and I. R. Fisher, Phys. Rev. Lett. **88**, 047005 (2002).

[94] W. Higemoto, A. Koda, R. Kadano, Y. Kawasaki, Y. Haga, D. Aoki, R. Settai, H. Shishido, and Y. Ōnuki, J. Phys. Soc. Jpn. **71**, 1023 (2002).

[95] T. Mito, S. Kawasaki, G. -q. Zheng, Y. Kawasaki, K. Ishida, Y. Kitaoka, D. Aoki, Y. Haga, and Y. Ōnuki, Phys. Rev. B **63**, 220507(R) (2001).

[96] K. Maki, G. Yang, and H. Won, Physica C **341-348**, 1647 (2000).

[97] H. Aubin, K. Behnia, M. Ribault, R. Gagnon, and L. Taillefer, Phys. Rev. Lett. **78**, 2624 (1997).

[98] H. Aoki, T. Sakakibara, H. Shishido, R. Settai, Y. Ōnuki, P. Miranovic, and K. Machida, J. Phys.: Condens. Matter **16**, L13 (2004).

[99] M. R. Eskildsen, C. D. Dewhurst, B. W. Hoogenboom, C. Petrovic, and P. C. Canfield, Phys. Rev. Lett. **90**, 187001 (2003).

[100] M. J. Graf, S.-K. Yip, J. A. Sauls, and D. Rainer, Phys. Rev. B **53**, 15147 (1996).

[101] A. Bianchi, R. Movshovich, N. Oeschler, P. Gegenwart, F. Steglich, J. D. Thompson, P. G. Pagliuso, and J. L. Sarrao, Phys. Rev. Lett. **89**, 137002 (2002).

[102] T. Tayama, A. Harita, T. Sakakibara, Y. Haga, H. Shishido, R. Settai, and Y. Ōnuki, Phys. Rev. B **65**, 18050(R) (2002).

[103] T. Takeuchi, H. Shishido, S. Ikeda, R. Settai, Y. Haga, and Y. Ōnuki, J. Phys.: Condens. Matter **14**, L261 (2002).

[104] N. Oeschler, P. Gegenwart, M. Lang, R. Movshovich, J. L. Sarrao, J. D. Thompson, and F. Steglich, Phys. Rev. Lett. **91**, 076402 (2003).

[105] C. Capan, A. Bianchi, R. Movshovich, A. D. Christianson, A. Malinowski, M. F. Hundley, A. Lacerda, P. G. Pagliuso, and J. L. Sarrao, Phys. Rev. B **70**, 134513 (2004).

[106] C. Martin, C. C. Agosta, S. W. Tozer, H. A. Radovan, E. C. Palm, T. P. Murphy, and J. L. Sarrao, Phys. Rev. B **71**, 020503(R) (2005).

[107] T. Watanabe, Y. Kasahara, K. Izawa, T. Sakakibara, Y. Matsuda, C. J. van der Beek, T. Hanaguri, H. Shishido, R. Settai, and Y. Ōnuki, Phys. Rev. B **70**, 020506(R) (2004).

[108] K. Kakuyanagi, M. Saitoh, K. Kumagai, S. Takashima, M. Nohara, H. Takagi, and Y. Matsuda, Phys. Rev. Lett. **94**, 047602 (2005).

[109] J. Paglione, M. A. Tanatar, D. Hawthorn, E. Boaknin, F. Ronning, R. W. Hill, M. Sutherland, L. Taillefer, C. Petrovic, and P. Canfield, cond-mat/0405157 (2004).

[110] J. S. Kim, J. Alwood, G. R. Stewart, J. L. Sarrao, and J. D. Thompson, Phys. Rev. B **64**, 134524 (2001).

[111] V. A. Sidorov, M. Nicklas, P. G. Pagliuso, J. L. Sarrao, Y. Bang, A. V. Balatsky, and J. D. Thompson, Phys. Rev. Lett. **89**, 157004 (2002).

[112] G. -q. Zheng, K. Tanabe, T. Mito, S. Kawasaki, Y. Kitaoka, D. Aoki, Y. Haga, and Y. Ōnuki, Phys. Rev. Lett. **86**, 4664 (2001).

[113] T. Muramatsu, N. Tateiwa, T. C. Kobayashi, K. Shimizu, K. Amaya, D. Aoki, H. Shishido, Y. Haga, and Y. Ōnuki, J. Phys. Soc. Jpn. **70**, 3362 (2001).

[114] A. Bianchi, R. Movshovich, I. Vekhter, P. Pagliuso, and J. L. Sarrao, Phys. Rev. Lett. **91**, 257001 (2003).

[115] S. Nakatsuji, S. Yeo, L. Balicas, Z. Fisk, P. Schlottmann, P. G. Pagliuso, N. O. Moreno, J. L. Sarrao, and J. D. Thompson, Phys. Rev. Lett. **89**, 106402 (2002).

[116] T. Moriya and K. Ueda, Solid State Commun. **15**, 169 (1974).

[117] A. Ishigaki and T. Moriya, J. Phys. Soc. Jpn. **65**, 3402 (1996).

[118] H. Hegger, C. Petrovic, E. G. Moshopoulou, M. F. Hundley, J. L. Sarrao, Z. Fisk, and J. D. Thompson, Phys. Rev. Lett. **84**, 4986 (2000).

[119] M. Nicklas, R. Borth, E. Lengyel, P. G. Pagliuso, J. L. Sarrao, V. A. Sidorov, G. Sparn, F. Steglich, and J. D. Thompson, J. Phys.: Condens. Matter **13**, L905 (2001).

[120] E. Lengyel, R. Borth, P. G. Pagliuso, J. L. Sarrao, G. Sparn, F. Steglich, and J. D. Thompson, High Pres. Res. **22**, 185 (2002).

[121] H. Shishido, T. Ueda, S. Hashimoto, T. Kubo, R. Settai, H. Harima, and Y. Ōnuki, J. Phys.: Condens. Matter **15**, L499 (2003).

[122] M. Yashima, S. Kawasaki, Y. Kawasaki, G. -q. Zheng, Y. Kitaoka, H. Shishido, R. Settai, Y. Haga, and Y. Ōnuki, J. Phys. Soc. Jpn. **73**, 2073 (2004).

[123] G. Sparn, R. Borth, E. Lengyel, P. G. Pagliuso, J. L. Sarrao, F. Steglich, and J. D. Thompson, Physica B **312-313**, 138 (2002).

[124] G. Knebel, M.-A. Measson, B. Salce, D. Aoki, D. Braithwaite, J. P. Brison, and J. Flouquet, J. Phys.: Condens. Matter **16**, 8905 (2004).

[125] H. Won, S. Haas, K. Maki, D. Parker, B. Dora, and A. Virosztek, Phys. Stat. Sol. , in press.

[126] R. S. Kumar, A. L. Cornelius, and J. L. Sarrao, Phys. Rev. B **70**, 214526 (2004).

[127] T. Tayama, Y. Namai, T. Sakakibara, M. Hedo, Y. Uwatoko, H. Shishido, R. Settai, and Y. Ōnuki, J. Phys. Soc. Jpn. **74**, 1115 (2005).

[128] E. Helfand and N. Werthamer, Phys. Rev. **147**, 288 (1966).

[129] T. P. Orlando, E. J. McNiff Jr., S. Foner, and M. R. Beasley, Phys. Rev. B **19**, 4545 (1979).

[130] C. F. Miclea, M. Nicklas, D. Parker, K. Maki, J. L. Sarrao, J. D. Thompson, G. Sparn, and F. Steglich, Phys. Rev. Lett. **96**, 117001 (2006).

[131] H. Won and K. Maki, Phys. Rev. B **49**, 1397 (1994).

[132] K. Maki, AIP Conf. Proc. **438**, 83 (1998).

[133] R. Ikeda, private communication.

[134] P. Villars and L. D. Calvert, Pearsons Handbook of Crystallographic Data for Intermetallic Phases, The American Society for Metals, Metals Park Oh. (1985).

[135] H. R. Ott, H. Rudigier, Z. Fisk, and J. L. Smith, Phys. Rev. Lett. **50**, 1595 (1983).

[136] G. Landgren, Y. Jugnet, J. F. Morar, A. J. Arko, Z. Fisk, J. L. Smith, H. R. Ott, and B. Reihl, Phys. Rev. B **29**, 493 (1984).

[137] M. C. Aronson, J. D. Thompson, J. L. Smith, Z. Fisk, and M. W. McElfresh, Phys. Rev. Lett. **63**, 2311 (1989).

[138] D. L. Cox, Phys. Rev. Lett. **59**, 1240 (1987).

[139] D. L. Cox, Physica B **186-188**, 312 (1993).

[140] H. R. Ott, Progress in Low Temp. Phys. XI, Elsevier Science Publishers, page 215 (1987).

[141] M. B. Maple, J. W. Chen, S. E. Lambert, Z. Fisk, J. L. Smith, H. R. Ott, J. S. Brooks, and M. J. Naughton, Phys. Rev. Lett. **54**, 477 (1985).

[142] R. Felten, F. Steglich, G. Weber, H. Rietschel, F. Gompf, B. Renker, and J. Beuers, Europhys. Lett. **2**, 323 (1986).

[143] E. A. Knetsch, G. J. Nieuwenhuys, J. A. Mydosh, R. H. Heffner, and J. L. Smith, Physica B **186-188**, 251 (1993).

[144] F. Kromer, R. Helfrich, M. Lang, F. Steglich, C. Langhammer, A. Bach, T. Michels, J. S. Kim, and G. R. Stewart, Phys. Rev. Lett. **81**, 4476 (1998).

[145] F. Kromer, M. Lang, N. Oeschler, P. Hinze, C. Langhammer, F. Steglich, J. S. Kim, and G. R. Stewart, Phys. Rev. B **62**, 12477 (2000).

[146] R. Helfrich, Dissertation, TU Darmstadt, unpublished (1996).

[147] J. D. Thompson, J. Magn. Magn. Mater. **63-64**, 358 (1987).

[148] J. A. Olsen, R. A. Fisher, N. E. Phillips, G. R. Stewart, and A. L. Giorgi, Bull. Am. Phys. Soc. **31**, 648 (1986).

[149] N. E. Phillips, R. A. Fisher, J. Flouquet, A. L. Giorgi, J. A. Olsen, and G. R. Stewart, J. Magn. Magn. Mat. **62-63**, 172 (1987).

[150] F. Steglich, P. Gegenwart, R. Helfrich, C. Langhammer, P. Hellmann, L. Donnevert, C. Geibel, M. Lang, G. Sparn, W. Assmus, G. R. Stewart, and A. Ochiai, Z. Phys. B **103**, 235 (1997).

[151] T. Moriya and T. Takimoto, J. Phys. Soc. Jpn. **64**, 960 (1995).

[152] N. Oeschler, F. Kromer, T. Tayama, K. Tenya, P. Gegenwart, G. Sparn, F. Steglich, M. Lang, and G. R. Stewart, Acta Phys. Pol. B. **34**, 255 (2003).

[153] D. L. Cox and M. Jarrell, J. Phys.: Condens. Matter **8**, 9825 (1996).

[154] D. L. Cox, Physica B **223-224**, 453 (1996).

[155] H. R. Ott, H. Rudigier, Z. Fisk, and J. L. Smith, in Moment Formation in Solids, Proceedings of a NATO Advanced Study Institute, edited by W. J. L. Buyers, Plenum, New York, page 305 (1984).

[156] B. Renker, F. Gompf, W. Reichardt, H. Rietschel, J. B. Suck, and J. Balers, Phys. Rev. B **32**, 1859 (1985).

[157] H. R. Ott and Z. Fisk, in Handbook of Physics and Chemistry of the Actinides, edited by A. J. Freeman and G. H. Lander, Elsevier, Amsterdam, page 85 (1987).

[158] F. Steglich, J. Aarts, C. D. Bredl, W. Lieke, D. Meschede, W. Franz, and H. Schäfer, Phys. Rev. Lett. **43**, 1892 (1979).

[159] C. Wälti, Dissertation, Swiss Federal Institute of Technology Zurich, unpublished (2000).

[160] C. Langhammer, R. Helfrich, A. Bach, F. Kromer, M. Lang, T. Michels, M. Deppe, F. Steglich, and G. R. Stewart, J. Magn. Magn. Mater. **177-181**, 443 (1998).

[161] H. R. Ott, H. Rudigier, T. M. Rice, K. Ueda, Z. Fisk, and J. L. Smith, Phys. Rev. Lett. **52**, 1915 (1984).

[162] C. Wälti, H. R. Ott, Z. Fisk, and J. L. Smith, Phys. Rev. Lett. **84**, 5616 (2000).

[163] F. Gross, B. S. Chandrasekhar, D. Einzel, K. Andres, P. J. Hirschfeld, H. R. Ott, J. Beuers, Z. Fisk, and J. L. Smith, Z. Phys. B: Condens Matter **64**, 175 (1986).

[164] D. Einzel, P. J. Hirschfeld, F. Gross, B. S. Chandrasekhar, K. Andres, H. R. Ott, J. Beuers, Z. Fisk, and J. L. Smith, Phys, Rev. Lett. **56**, 2513 (1986).

[165] L. Glémot, J. P. Brison, J. Flouquet, A. I. Buzdin, I. Sheikin, D. Jaccard, C. Thessieu, and F. Thomas, Phys. Rev. Lett. **82**, 169 (1999).

[166] U. Rauchschwalbe, U. Ahlheim, F. Steglich, D. Rainer, and J. J. M. Franse, Z. Phys. B **60**, 379 (1985).

[167] U. Rauchschwalbe, U. Ahlheim, C. D. Bredl, H. M. Mayer, and F. Steglich, J. Magn. Magn. Mater. **63-64**, 447 (1987).

[168] K. Ueda and T. M. Rice, Phys. Rev. B **31**, 7114 (1985).

[169] E. I. Blount, Phys. Rev. B **32**, 2935 (1985).

[170] R. Joynt and T. M. Rice, Phys. Rev. B **32**, 6074 (1985).

[171] C. F. Miclea, F. M. Grosche, J. Sichelschmidt, G. R. Stewart, G. Sparn, and F. Steglich, Physica B **312-313**, 97 (2002).

[172] P. H. P. Reinders, B. Wand, F. Steglich, G. Fraunberger, G. R. Stewart, and G. Adrian, Europhys. Lett. **25**, 619 (1994).

[173] N. E. Alekseevskii, A. V. Mitin, A. S. Rudenko, and A. A. Sorokin, Pis'ma Zh. Eksp. Teor. Fiz. **43**, 533 (1986), [JETP Lett. **H3**, 690 (1986)].

[174] R. H. Friend and D. Jérome, J. Phys. **12**, 1441 (1979).

[175] L. P. Gorkov, Usp. Fiz. Nauk **144**, 381 (1984).

[176] A. I. Buzdin and L. N. Bulaevskii, Usp. Fiz. Nauk **144**, 415 (1984).

[177] K. Machida, Appl. Phys. **35**, 193 (1984).

[178] C. A. Balseiro and L. M. Falicov, Phys. Rev. B **20**, 4457 (1979).

[179] M. Kitaoka, IBM J. Res. Dev. **33**, 356 (1989).

[180] A. A. Gorbatsevich, V. P. Elesin, and Y. V. Kopaev, Phys. Lett. A **125**, 149 (1987).

[181] M. Ichimura, M. Fujita, and K. Nakao, Phys. Rev. B **43**, 175 (1991).

[182] Y. V. Kopaev, Trudy Fiz. Inst. Akad. Nauk SSSR **86**, 3 (1975).

[183] M. Vlasse and L. Fournes, Mater. Res. Bull. **11**, 1527 (1976).

[184] T. Ohtani, Y. Miyoshi, Y. Fujii, T. Koyakumaru, T. Kusano, and K. Minami, Solid State Commun. **120**, 95 (2001).

[185] W. Bensch, J. Abart, and E. Amberger, Solid State Commun. **58**, 631 (1986).

[186] R. Schlögl and W. Bensch, J. Less-Common Met. **132**, 155 (1987).

[187] R. Rao, D. Gaitone, A. Garg, B. K. Godwal, and H. D. Hochheimer, to be published.

[188] T. Sekine, Y. Kiuchi, E. Matsuura, K. Uchinokura, and R. Yoshizaki, Phys. Rev. B **36**, 3153 (1987).

[189] T. Ohtani, Y. Yokota, and H. Sawada, Jpn. J. Appl. Phys. **38**, L142 (1999).

[190] W. Bensch, J. Koy, and W. Biberacher, Solid State Commun. **93**, 261 (1995).

[191] Y. Fujii, T. Koyakumaru, T. Ohtani, Y. Miyoshi, S. Sunagawa, and M. Sugino, Solid State Commun. **121**, 165 (2002).

[192] See, for example, C. Kittel, Introduction to Solid State Physics 5-th edition, Wiley, New York, (1976).

[193] A. M. Gabovich, A. I. Voitenko, and M. Ausloos, Phys. Rep. **367**, 583 (2002).

[194] A. M. Gabovich, D. P. Moiseev, and A. S. Shpigel, J. Phys. **15**, L569 (1982).

[195] A. M. Gabovich, D. P. Moiseev, and A. S. Shpigel, Pis'ma Zh. Z Eksp. Teor. Fiz. **83**, 1383 (1982), [Sov. Phys. JETP **56**, 795 (1982)].

[196] C. E. Methfessel, A. R. Stewart, B. T. Matthias, and C. K. N. Patel, Proc. Natl. Acad. Sci. USA **77**, 6307 (1980).

[197] A. M. Gabovich, D. P. Moiseev, L. V. Prokopovich, S. K. Uvarova, and V. E. Yachmenev, Pis'ma Zh. Z Eksp. Teor. Fiz. **86**, 1727 (1984), [Sov. Phys. JETP **59**, 1006 (1984)].

[198] M. Sato, H. Fujishita, and S. Hoshino, J. Phys. **16**, L417 (1983).

[199] J. M. Heintz, M. Drillon, R. Kuentzler, Y. Dossmann, J. P. Kappler, O. Durmeyer, and F. Gautier, Z. Phys. B **76**, 303 (1989).

[200] H. Okamoto, H. Taniguti, and Y. Ishihara, Phys. Rev. B **53**, 384 (1996).

[201] W. L. McMillan, Phys. Rev. **167**, 331 (1968).

[202] H. Okamoto and Y. Ishihara, Phys. Rev. B **48**, 3927 (1993).

[203] J. R. Clem, Ann. Phys. N. Y. **40**, 268 (1966).

[204] N. Kobayashi, K. Noto, and Y. Muto, J. Low Temp. Phys. **27**, 217 (1977).

[205] B. J. C. van der Hoeven Jr. and P. H. Keesom, Phys. Rev. **135**, A631 (1964).

[206] B. W. Roberts, Progress in Cryogenics, Heywood and Co. Ltd., London, (1964).

[207] F. Heininger, E. Bucher, and J. Muller, Phys. Kondens. Mater. **5**, 243 (1966).

[208] G. Bilbro and W. L. McMillan, Phys. Rev. B **14**, 1887 (1976).

[209] W. W. Fuller, P. M. Chaikin, and N. P. Ong, Phys. Rev. B **24**, 1887 (1981).

[210] B. Horovitz, H. Gutfreund, and M. Weger, Phys. Rev. B **9**, 1246 (1975).

[211] M. Ido, Y. Okayama, T. Ijiri, and Y. Okajima, J. Phys. Soc. Jpn. **59**, 1341 (1990).

[212] M. Núñez, J. M. Mignot, and D. Castello, Europhys. Lett. **18**, 53 (1992).

ACKNOWLEDGMENTS

I owe my gratitude to all the people who have made this thesis possible.

First and foremost I would like to express my gratitude to Prof. Frank Steglich whom I have known as an outstanding physicist. I thank him for his constant support and guidance during the last years.

I would particularly like to thank Dr. Michael Nicklas for his constant help and support. Without his amazing efficiency in solving a great variety of issues, from science to organizational problems, this thesis would still have been a distant achievement. He has always made himself available for help and advice and there has never been an occasion when I have knocked on his door and he has not given me time.

Special thanks I owe to Dr. Günter Sparn for his guidance and constant help from the beginning of my work in Dresden. It was him who introduced me to the field of high pressure physics.

I want to express my sincere gratitude to Dr. Michael Nicklas and Edit Lengyel for their thorough reading and corrections to my thesis. Without their help I would have, most likely, missed the deadline for submitting my thesis. Furthermore I want to thank Prof. Hans Dieter Hochheimer, Prof. Ana Celia Mota, Dr. Peter Thalmeier and Prof. Manfred Sigrist for proof-reading parts of this work and for their valuable comments. For stimulating discussion and a fruitful collaboration regarding the

phenomena described in Chapter 3, I want to thank Prof. Kazumi Maki and David Parker. Additionally my gratitude goes to Prof. Ryusuke Ikeda and Prof. Joe D. Thompson for valuable discussions.

I am in debt to Dr. Tomasz Cichorek, Dr. Teodora Radu, Dr. Yoshifumi Tokiwa and Franziska Weickert for allowing me to use their cryostats and for their help during some of my measurements.

Special thanks go to Dr. Malte Grosche for guidance in the beginning of my work in Dresden.

For supplying the compounds investigated in this work I am glad to thank Dr. John L. Sarrao, Prof. Gregory R. Stewart and Prof. Hans Dieter Hochheimer.

As all of my experimental physicists colleagues, at points of my work I ran into technical problems with pumps failures and broken gauges. As all of them I have to thank to Robert Borth and Dr. Thomas Lühmann for technical assistance. For the drawings of the pressure cells I like to thank Christoph Klausnitzer, our Autodesk expert.

For machining the miniaturized specific heat and the resistivity pressure cells I acknowledge Ralf Koban and Ion Cheroi, respectively.

The working environment at Max Planck Institute has been made enjoyable by my colleagues, starting with my office mates, Edit Lengyel, Huiqiu Yuan, Constantze Lamprecht and continuing with Dr. Teodora Radu, Dr. Takeshi Nakanishi, Dr. Michael Nicklas, Dr. Stefan Mederle, Monica Leonte, Adriana Sanchez and Julia Ferstl. My flatmates in the famous Chemnitzer Str. 59C, Dr. Niels Oeschler, Gabriel Dionicio and Dr. Ivica Zerec, made my staying in Dresden pleasant.

I owe my deepest thanks to my family, my wife, my brother and my parents who have always stood by me. Words cannot express the gratitude I owe them.

It is impossible to remember all, and I apologize to those I have inadvertently left out.

Author's declaration

I declare that the work described in this dissertation was carried out in accordance with the regulations of the Dresden University of Technology. No part of this work has been submitted previously for a degree or other qualification at this or any other university. The research reported herein is original, except where specific reference is acknowledged to the work of others. All the research was carried out under the supervision of Prof. Frank Steglich at the Max Planck Institute for Chemical Physics of Solids between January 2000 and December 2005.

Corneliu F. Miclea

Dresden, Germany

December 23rd, 2005

Versicherung

Hiermit versichere ich, dass ich die vorliegende Arbeit ohne unzulässige Hilfe Dritter und ohne Benutzung anderer als der angegebenen Hilfsmittel angefertigt habe; die aus fremden Quellen direkt oder indirekt übernommenen Gedanken sind als solche kenntlich gemacht. Die Arbeit wurde bisher weder im Inland noch im Ausland in gleicher oder ähnlicher Form einer anderen Prüfungsbehörde vorgelegt.

Die vorliegende Dissertation wurde unter der Betreuung von Prof. Dr. Frank Steglich am Max-Planck-Institut für Chemische Physik fester Stoffe in Dresden im Zeitraum von Januar 2000 bis Dezember 2005 angefertigt. Ich erkenne die Promotionsordnung an.

Corneliu F. Miclea

Dresden, Deutschland

23. Dezember, 2005